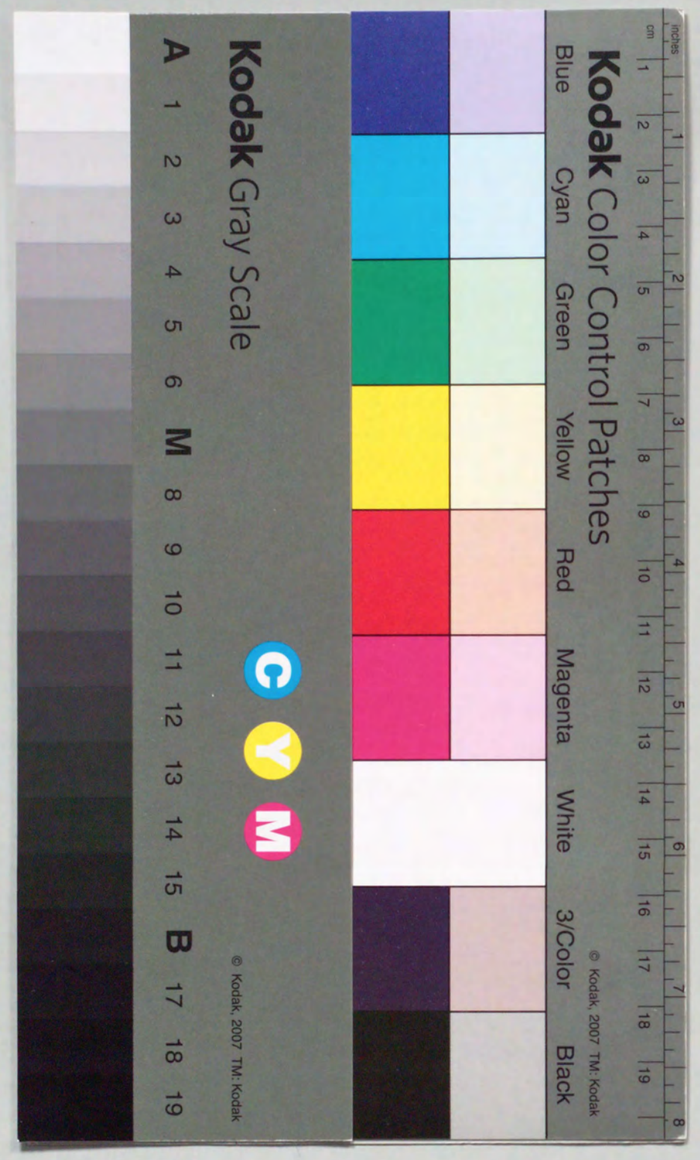

Projectile-Fragmentation Process Studied by Detecting the Spin Polarization of Heavy Fragments of ~100MeV/nucleon

AKIRA OZAWA

DISSERTATION IN PHYSICS

THE OSAKA UNIVERSITY

GRADUATE SCHOOL OF SCIENCE

TOYONAKA, OSAKA

(1)

Projectile-Fragmentation Process Studied by Detecting the Spin Polarization of Heavy Fragments of ~100MeV/nucleon

AKIRA OZAWA

PHYSICS DEPARTMENT
GRADUATE SCHOOL OF SCIENCE
OSAKA UNIVERSITY
TOYONAKA, OSAKA, 560, JAPAN

1992

Acknowledgement

I am grateful to Prof. T. Minamisono who has shared his knowledge with me and allowed me to study nuclear physics at the Lawrence Berkeley Laboratory. I also wish to express my thanks to Prof. Y. Nojiri, Dr. K. Matsuta and Mr. M. Fukuda for their collaboration, discussion and encouragement throughout this study.

I would like to thank Prof. K. Sugimoto, Prof. I. Tanihata, Dr. K. Yoshida, Dr. T. J. M. Symons, Dr. G. F. Krebs and Dr. J. R. Alonso for the collaboration and valuable suggestions for this study. I would also like to thank Mr. A. Kitagawa, Mr. S. Momota, Mr. T. Ohtsubo, Mr. Y. Matsuo, Mr. H. Takechi, Mr. S. Fukuda and Ms. I. Minami for their collaboration.

All experiments for the present work were carried out at the Bevatron at Lawrence Berkeley Laboratory in the USA, under program numbers E752H and E955H. The staff and crew of the Bevatron are appreciated for their hospitality and cooperation.

Mr. Y. Takahashi, Mr. M. Sakamoto, Mr. K. Omata, Dr. F. Myers, Ms. J. Miller, and Ms. K. Ohsawa provided technical support.

Last, but not least, I would like to thank Prof. K. Katori, Prof. M. Kondo, Prof. Y. Nagashima, and Prof. H. Ohtsubo for their encouragement.

Abstract

106 MeV/nucleon ^{40}Ca beam and 108 Mev/nucleon ^{46}Ti beam were used to bombard Au and C targets. Spin polarization, as well as momentum and angular distributions, of the projectile fragments ^{37}K, ^{39}Ca and ^{43}Ti were measured at forward angles ($\theta \sim 2^{o}$). The observed widths of the angular distributions were broader than those predicted by the Goldhaber model, which explained the widths of the momentum distributions well, for collisions both with Au and C targets. For comprehension of the broadening, observation of the nuclear spin polarization of the fragments can be the best mean. It determines the sign of the scattering angle, since the sign of the polarization depends upon whether positive or negative scattering angles dominate in the reaction. Although polarization detection is usually difficult for heavy fragments which are short-lived β-radioactive nuclei, we made it possible by combining the fragment separator and the β-NMR method, and measured precisely the nuclear spin polarization for the first time.

The observed momentum dependences of the polarization were accounted for by a simple projectile fragmentation model. Thus, it can be a good probe to determine the sign of the scattering angle. It was concluded from the measurement that positive-angle scattering dominates in the case of the Au target and negative-angle scattering dominates in the case of the C target. This result strongly suggests orbital deflection of the projectile prior to the breakup by the Coulomb potential for the Au target and the nuclear potential for the C target. Even in the present energy region, these potentials play important role and cause the broadening in the angular distributions of the fragments.

Since polarization has been obtained in heavy projectile-fragments through high-energy heavy-ion collisions and the polarization is found to be

predictable, the present technique has been applied for the measurement of the magnetic moment of ^{43}Ti ($I^{\pi} = 7/2^-$, $T_{1/2} = 0.5$ sec). The magnetic moment of ^{43}Ti was determined to be $|\mu| = 0.85\ (2)$ nm. It was shown that the observed magnetic moment deviated significantly from the Schmidt value for a single particle in $I^{\pi} = 7/2^-$ state but still was between the Schmidt lines, i.e., $I^{\pi} = 7/2^-$ and $I^{\pi} = 5/2^-$ states, respectively. The large deviation was explained fairly well by first-order configuration-mixing.

Table of contents

List of tables

List of figures

Chapter 1. Introduction

1.1 Puzzle regarding the angular distributions of projectile fragments

Projectile-like heavy products of peripheral heavy-ion collisions, namely projectile fragments, in the energy region around 100 MeV/nucleon seem to provide important information for the study of the reaction mechanism, since the transverse momentum distributions, namely the angular distributions, of the projectile fragments are broader than the momentum distributions, while a simple fragmentation model predicts uniform distributions. The sign of the scattering angle of projectile fragments, the definition of which is given in Fig. 2.7, can be an important clue for the broadening. Since the polarization of the fragments is the observable most sensitive to the sign, polarization phenomena in the projectile-fragmentation process were studied.

(a) The projectile-fragmentation process

For bombarding energies higher than 100 MeV/nucleon, the de Broglie wavelength of each nucleon inside a nucleus (less than 0.4 fm) is much smaller than the each nucleon distance (~1.8 fm). Individual collisions of nucleons that are constituents of the colliding nuclei, rather than the macroscopic interaction between the nuclei, thus become important in reaction at these energies (WE76). In this case the velocity of the relative motion of colliding nuclei is much larger than the Fermi motion of the nucleons inside the nucleus (E_F~40 MeV/nucleon, where E_F is the Fermi energy.). As a result, the overlapping region formed by the target nucleus and the projectile nucleus turns into a hot region at the collision and the

remainder part of the projectile flies away unaffected to be detected as a fragment. These two parts are often called the participant and the spectator, respectively. Such a process is called the projectile-fragmentation process. Under the participant-spectator picture, it is predicted that the momentum and angular distribution of projectile fragments are both described by the Goldhaber model, which further assumes the minimal correlations among the momenta of nucleons. Thus these momentum distributions are determined by the Fermi momenta of the nucleons inside the nucleus (GO74).

(b) Broadening of the angular distributions of fragments

However, for the angular distributions of projectile fragments at around 100MeV/nucleon, the observation was quite different from the prediction. An experiment using ^{16}O + Al/Au systems at $2^o < \theta < 8^o$ revealed that the angular distributions of the fragments are much broader than those expected from the Fermi motion only (BI79). For solving the causes of the surprising broadening, determination of the sign of scattering angle is indispensable, since positive-angle scattering is governed mainly by the Coulomb potential; on the contrary, negative-angle scattering is governed by the nuclear potential.

(c) Determining sign of the scattering angle by an analysis of the angular distributions

Wong and Bibber analyzed the same experimental data for the ^{16}O + Al/Au systems at $2^o < \theta < 8^o$, and introduced the Coulomb final-state interaction in order to explain the Z_f dependence of the width of the angular distributions; Z_f is the atomic number of the fragment (WO82). (the Coulomb

final-state interaction is the interaction between protons in the participant and the spectator fragment through the Coulomb field.) The Z_f dependence of the width is sensitive to the sign of the scattering angle. The observed charge effect suggested that the type of the scattering is predominantly positive-angle scattering for both Au and Al targets.

Recently, the angular distributions of fragments has been precisely remeasured for the same ^{16}O + Al/Au systems at the same energy at $2^o < \theta < 8^o$ (SI88). A detailed examination of the momentum distributions revealed strong energy-dumping at larger angles. From the target mass dependence of this energy dumping, it was suggested that the sign of the scattering angle is always positive for components outside the grazing angle, regardless of the target mass.

The sign of the scattering angles in the energy region around 100 MeV/nucleon was thus determined to be positive by an analysis of the angular distributions. These results suggest the importance of the Coulomb potential for the transverse momentum of the fragments at the present energy. However, in the light target, the broadening beyond the classical grazing angle can not be explained very well. And their assumption (only the participant came from the projectile contributes the Coulomb final-state interaction.) was too rough since they completely neglected the participant came from the target. Thus, before conclusive statements can be given, other direct measurements are necessary in order to confirm the sign of the scattering angle. For such measurements, heavier fragments have advantages over lighter fragments, since the contribution from the Fermi momenta, which divert the orbits of the fragments, is smaller.

(d) New observable: spin polarization

The nuclear spin polarization of the fragments can be the best probe of the sign of scattering angle, since the sign of the polarization reflects the direction of the orbital angular momentum of the projectile and, thus, strongly depends on whether positive or negative scattering angles dominate. Although determination of the sign of scattering angle through fragment polarization is model dependent, it is likely to be the most reliable method because of the data compilation in the lower energy regions (SU77) (AS90). The model, which is based on the rather simple nature of the polarization mechanism, is also well established and reliable for reproducing the experimental data.

It is noted that the qualitative trend in the momentum dependence of the fragment polarization could be well explained by a model based on the participant-spectator picture. The model assumes that the origin of the polarization is the orbital angular momentum left in the spectator fragment by a sudden disappearance of the participant nucleons from the incident projectile at the instant of the collision. Therefore in the energy region around 100 MeV/nucleon, the polarization mechanism is expected to be the same. It should, of course, be clarified. Once the mechanism becomes clear, it can be the best means for determining the sign of the scattering angle.

(e) The present study: observation of the polarization of heavier projectile fragments

Heavy-ion accelerator, the Bevalac, at Lawrence Berkeley Laboratory can supply heavier projectiles in the energy region higher than 100 MeV/nucleon with good quality and high intensity. A fragment-separator set at Beam line No. 44, which was developed by our group from 1983 (MA89),

can be used to separate and purify projectile fragments in the mass region A<50. By using a high-energy heavy-ion beam and the separation technique, the polarization of heavy fragments has been studied.

For heavy fragments which are short-lived β-radioactive nuclei, polarization detection is usually difficult. To measure the polarization reliably, Sugimoto (SU65) and Minamisono (MI73) have developed a β-NMR method that is applicable to β-emitting nuclei. This method has the following advantages for measuring the polarization:

(i) The ground state of a short-lived β-radioactive nucleus can be studied.

(ii) The analyzing power can be as large as 100%.

(iii) The geometrical asymmetry of the detection system can be completely canceled by inverting the nuclear spin using a radio-frequency magnetic field.

Maintaining the polarization of the heavy nuclei (A~40) during their lifetime is crucial for this technique; it is not always easy to find suitable samples. The hyperfine interactions were studied for the last twenty years using the β-emitter produced by the Van de Graff accelerator at Osaka University. The compiled data were indispensable for the present study.

We combined these techniques, and measured the nuclear spin polarization of heavy projectile fragments (^{37}K, ^{39}Ca and ^{43}Ti), which are all short-lived β-radioactive nuclei, produced through the ^{40}Ca + Au and the ^{46}Ti + C/Au collisions near the classical grazing angle ($\theta \sim 2^{o}$) at an energy of around 100 MeV/nucleon. The observed polarization showed the same trend as that observed at much lower energies (10 MeV/nucleon). From the momentum dependence of the polarization, we could prove positive-angle

scattering for an Au target and negative-angle scattering in a C target. The results suggest that the orbital deflection of the projectile prior to breakup by the Coulomb potential for the Au target and the nuclear potential for the C target plays an important role regarding the transverse momentum of the fragments.

1.2 Application: mirror magnetic moments

The polarization of projectile fragments can be applied to other important fields of studies, for example, such as studies of the non-nucleonic degrees of freedom through the magnetic moments. Studying the non-nucleonic degrees of freedom inside a nucleus, such as mesonic and quark effects, is one of the most exciting fields in present-day nuclear physics. They are studied through the axial-vector coupling-constant in the weak interaction (TO86), magnetic moments of mirror nuclei (MI90), and the magnetic moments of high spin states (YA85).

Methods to study the non-nucleonic degrees of freedom through the magnetic moments of mirror nuclei in A=16±1 and A=40±1 regions have been greatly developed during this decade, both experimentally (MI90) and theoretically (TO83) (AR88). For a complete understanding, an extension of this study is very important and crucial. There are two possible directions for this extension. One is to study the same shell; the other is to study the next closed shell (±1 nucleon; A=56±1).

A study of mirror nuclei in the sd-shell has been carried out vigorously (RO86) (BR83). However, studies of the magnetic moments of mirror nuclei in the $f_{7/2}$ shell, which includes the A=56±1 region, is rare, especially regarding experimental work. Indeed, no mirror pairs have been studied,

except for A=41. The reason why the study is rare is due to the difficulties in producing such mirror nuclei with high productivity and in creating polarization in such nuclei. Now, however, the situation is changing. The projectile-fragmentation process in high-energy heavy-ion collisions provides a good tool to produce nuclei far from the line of stability. The polarization phenomena of projectile fragments have been well studied at intermediate energy (AS90) and higher energy regions, as described in the former section. The mechanism can be basically understood in terms of a simple projectile fragmentation model (AS90). We can therefore measure the magnetic moment of ^{43}Ti ($I^{\pi} = 7/2^{-}$, $T_{1/2}$ = 0.50 sec) by combining these techniques. ^{43}Ti constitutes on the A=43 mirror pair with ^{43}Sc, the magnetic moment of which is known. Furthermore, the recent development of a large-scale shell-model for the $f_{7/2}$ shell makes it possible to calculate the magnetic moment of ^{43}Ti using the first-order configuration-mixing effect (OG89) (RI91). Discussions concerning the non-nucleonic degrees of freedom are expected to progress from the pair moments.

1.3 Contents of this thesis

The main purpose of the present study was to investigate the reaction mechanism in the energy region around 100 MeV/nucleon through observations of the fragment polarization. Furthermore, the establishment of a technique to provide polarized nuclear-beams and their application to the magnetic-moment study are also described in this thesis. Typical aspects of the projectile-fragmentation process are described in Chapter 2. The principles of the technique used in the present measurements are described in Chapter 3. The experimental apparatus, including the fragment separator, are

introduced in Chapter 4. The results are discussed in Chapter 5. As a future study, the measurement of the magnetic moment of ^{43}Ti is described in Chapter 6. Conclusions concerning the present study are described in Chapter 7.

Chapter 2. Projectile-fragmentation process in high-energy heavy-ion collisions

A participant-spectator picture can be used to qualitatively describe the mechanism of the projectile-fragmentation process in high-energy nucleus-nucleus collisions. Only those constituent nucleons in a projectile nucleus, which interact with constituent nucleons in a target nucleus in the overlapping region, take part in strong nucleon-nucleon collisions, and they are classified as participants. Other nucleons, however, which do not interact strongly with other nucleons, fly away unaffected as spectators. These spectators, projectile fragments in other words, move at the same speed as that of the incident beam (Fig. 2.1). The production cross-sections as well as the momentum and angular distributions of the fragments in the process can well be explained in terms of the above-mentioned participant-spectator picture, as is described the following sections.

2.1 Production cross-sections of projectile fragments

Various kinds of nuclei, even those far from the line of stability, can be produced with high productivity at the same time through the projectile-fragmentation process in high-energy heavy-ion collisions, as shown in Fig. 2.2 (WE79).

The typical energy dependences of the cross-sections are shown in Table 2.1 (GU83). According to this table, the cross-sections are almost unchanged from 100 MeV/nucleon to around 1 GeV/nucleon, except for the cross-sections of one-nucleon-removal channels or charge-exchange-reaction channels, such as ^{12}C --> ^{13}C or ^{12}C --> ^{12}N. (The cross-sections in the energy

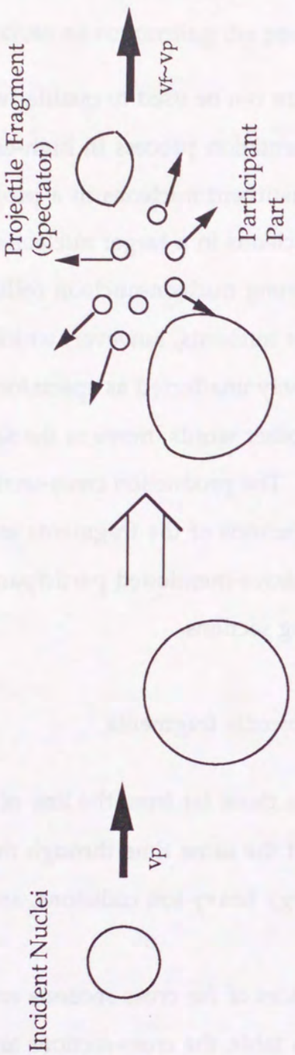

Fig. 2.1 Schematic view of projectile fragmentation process.

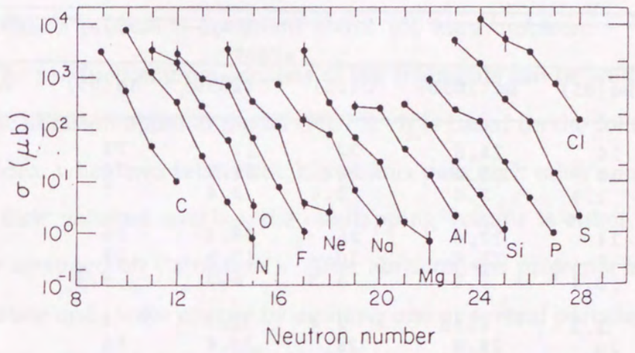

Fig. 2.2 Production cross sections for the elements observed in the fragmentation of 212 MeV/nucleon ^{48}Ca by a Be target. The lines are to guide the eye. (WE79)

Fragment		Target					
Z_F	A_F	Be(85)	Be(1050)	C(85)	C(1050)	Ag(85)	Ag(1050)
3	6	20	24.8	32	27	72	38
3	7	19	23.4	28	21.5	74	42
3	8	1.9	2.4	2.4	2.4	7	2.8
4	7	14	17.8	26	19.9	56	21.6
4	9	6	11.6	10	13.9	25	23.7
4	10	3.4	5.1	4.3	6.5	9.4	8.4
5	8	1.2	1.55	2.4	1.7	4	1.78
5	10	20	28.8	28	30.4	56	43.1
5	11	23	50.7	42	64.5	77	110
5	12	< 0.2	0.09	0.8	0.1	1.4	---
6	9	---	0.42	< 0.5	0.48	---	0.67
6	10	2	4	4	4.4	7	7.53
6	11	27	44.7	43	44.7	74	78.1
6	13	0.2	---	2.7	---	3	---
7	12	< 0.2	0.2	0.3	0.05	0.05	---
7	13	---	---	0.2	---	0.5	---
7	14	---	---	0.1	---	0.3	---

Table 2.1 Fragment production cross-sections (mb) in ^{12}C induced reactions at 85 MeV/nucleon and 1.05 GeV/nucleon. (GU83)

region around 100 MeV/nucleon are larger than those in the relativistic energy region.) The constant character in the cross-sections between 100 MeV/nucleon and 1 GeV/nucleon is one piece of evidence that the projectile-fragmentation process is dominant above 100 MeV/nucleon.

The production cross-sections of the fragments can be well reproduced using the abrasion-ablation model (HÜ75). It is based on the following very simple idea: when two relativistic heavy-ions pass each other so closely that a part of their volumes overlap, the overlapping volume is either sheared away or scrapped off ("abrasion"). After abrasion, the projectile is in an excited state and looses energy by emitting one or several particles ("ablation"). Hüfner et al. established a connection between the classical and macroscopic treatments of the abrasion-ablation process, and a quantum mechanical and microscopic multiple-scattering theory, such as the Glauber's multiple-scattering theory (GL59). According to their treatment, the expression of the cross-section for abrasion of n out of N neutrons and z out of Z protons from the projectile nucleus is given as

$$\sigma_{nz}(b) = \binom{N}{n}\binom{Z}{z}[\,1 - P(b)\,]^{n+z}\,P(b)^{A-n-z}\ , \qquad (2.1)$$

where $\binom{N}{n}$ and $\binom{Z}{z}$ are binomial coefficients, b is the impact parameter and $P(b)$ is the probability function at the impact parameter b, defined as follows:

$$P(b) = \int d^2s\, dz\, \rho_P(\,\mathbf{s}\,, z\,)\ \exp[\,-\,A_T\,\sigma^{NN}{}_{Tot}\ \int_{-\infty}^{+\infty}\rho_T(\,\mathbf{s}\text{-}\mathbf{b}\,, z'\,)\,dz'\,]\,. \quad (2.2)$$

Here A_T is the target mass-number and $\sigma^{NN}{}_{Tot}$ is the total nucleon-nucleon cross-section averaged over the isospin; the ρ's are the single-particle densities. The integral is essentially the overlap of the projectile and target densities when they pass at a distance of b from each other. In order to obtain the total abrasion cross-section, $\sigma_{nz}(b)$ is integrated over b,

$$\sigma_{nz} = \int \sigma_{nz}(b)\, 2\,\pi\, b\, db \ . \qquad (2.3)$$

In order to obtain more precise cross-sections, we should consider the final-state interaction. Abrasion means that a nucleon from the projectile ion is hit by a target nucleon, and is "knocked out" of its bound orbit. The struck nucleon may break up the remaining fragment. This effect is called the final-state interaction (FSI). The escape probability of one struck nucleon should be 50%, since it would be ejected isotoropically from the projectile. FSI therefore reduces the abrasion cross-section for a system in which one nucleon is sheared off by a factor of 2, and for a system in which two nucleons are sheared off by a factor of 4, etc.. The results of the abrasion-ablation calculation with FSI can well reproduce the experimental cross-sections, as shown in Ref. (HÜ75).

In order to evaluate the ablation process, the excitation energy of the fragment introduced by abrasion is necessary. The fragment excitation energy is estimated in a simple way in calculating the difference between the surface of the deformed primary ejectile and the surface of the same nucleus in a spherical shape. The average excitation-energy per nucleon is calculated to be

$$\frac{(E - E_0)(b)}{A - n} =$$

$$\frac{1}{2M} \frac{\int d^2s\, dz\, \rho_P(s\text{-}b,z) \mid \hbar\nabla \exp[\, -1/2\, A_T\, \sigma^{NN}{}_{Tot}\, (1 - i\alpha) \int \rho_T(s,z')\, dz'\,]\, \mid^2}{\int d^2s\, dz\, \rho_P(s\text{-}b,z) \quad \exp[\, -\, A_T\, \sigma^{NN}{}_{Tot}\, (1 - i\alpha) \int \rho_T(s,z')\, dz'\,]} \ ,$$

(2.4)

where M is the nucleon mass and the parameter α = Re $f^{NN}(O)$/Im $f^{NN}(O)$ is a measure of the real part of the nucleon-nucleon forward-scattering amplitude $f^{NN}(O)$; it can be omitted since it is sufficiently small.

Since we know the thresholds of particle emissions, we can calculate the production cross-sections of the fragments produced after the particle

emission (the ablation cross-section). Thus, by combining the ablation cross-section with the abrasion cross-section below the thresholds of the particle emission, we can obtain the realistic production cross-sections. The actual calculation of Equations (2.2) and (2.4) is described in Appendix 3.

2.2 Momentum distribution of projectile fragments

As shown in Fig. 2.3, at energies higher than 200 MeV/nucleon, the momentum distribution of the projectile fragments can be well described by a Gaussian in the projectile frame as

$$\frac{d^3\sigma}{dp^3} \propto \exp\left\{ -\frac{(p_L - p_0)^2}{2\sigma_L{}^2} \right\}, \qquad (2.5)$$

where p_0 denotes the average momentum of the fragments and σ_L is the width of the momentum distribution in the direction parallel to the beam. The longitudinal momentum spread (Δp_L) of fragments in the laboratory system is

$$\Delta p_L = \frac{\sigma_L}{\sqrt{1 - \beta^2}}, \qquad (2.6)$$

where $\beta = v/c$.

The momentum distribution is thus characterized by the center momentum (p_0) and the width (σ_L); p_0 is smaller than the average momentum of incident nuclei. Generally, however, the difference is very small compared with its momentum; for example, it is 10 - 130 MeV/c in the relativistic energy region (GR75). The velocity of fragments is therefore almost the same as that of the incident beam. The width (σ_L) does not depend on either the mass of the target or the incident velocity; it is well accounted for by the Fermi momenta of the nucleons inside a nucleus. The Goldhaber

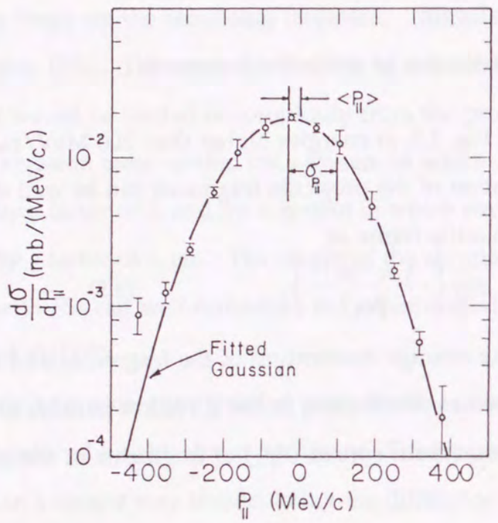

Fig. 2.3 The projectile-frame parallel-momentum distribution for ^{10}Be fragments from ^{12}C at 2.1 GeV/nucleon on a Be target. The mean momentum $p_L \equiv \langle p_{//} \rangle = -30$ MeV/c and standard deviation $\sigma_L \equiv \langle \sigma_{//} \rangle = 129$ MeV/c are indicated. (GR75)

model can well describe σ_L. The model assumes that there are minimal correlations among nucleon momenta and that the statistical combination determines the width; i.e., the width (σ_F) can be written as

$$\sigma_F = \sigma_0 \sqrt{\frac{A_F(A_P - A_F)}{(A_P - 1)}} , \qquad (2.7)$$

where A_P and A_F are the projectile mass-number and the fragment mass-number, respectively, and σ_0 is given by the Fermi momentum p_F (GO74). For the Fermi-gas model,

$$\sigma_0^2 = \frac{3}{5} p_F^2 . \qquad (2.8)$$

In intermediate-energy heavy-ion reactions (energy range of 10 - 100 MeV/nucleon), however, the distribution is not a simple Gaussian and a low energy tail is usually seen, as shown typically in Fig. 2.4 (GU83). The high-momentum side of the distribution, however, is well described by Equation (2.5), independent of target. Though the optimum p_0 is very close to the momentum of a projectile also in the energy region, one can usually find a small energy loss, unlike in the relativistic-energy region. Even though the energy loss has not been studied systematically, the following equation has been given empirically for the energy shift at around 50 MeV/nucleon (DU86):

$$\Delta E_N = E_{FN} - E_P = -0.45 (A_P - A_F) + 0.58 (Z_P - Z_F) - 0.48 \ \text{(MeV/nucleon)} . \qquad (2.9)$$

Here Z_P and Z_F are the projectile atomic number and the fragment atomic number, respectively. The width (σ_L) obtained by fitting a Gaussian only to the high-momentum side of the distribution is slightly less than that predicted by the Goldhaber model. The energy dependence of the reduced momentum width (σ_0) is shown in Fig. 2.5 (MU83). It should be noted that σ_0 increases with energy, and becomes almost flat at energies above 50 MeV/nucleon. The tendency of σ_0 at intermediate energies can be explained

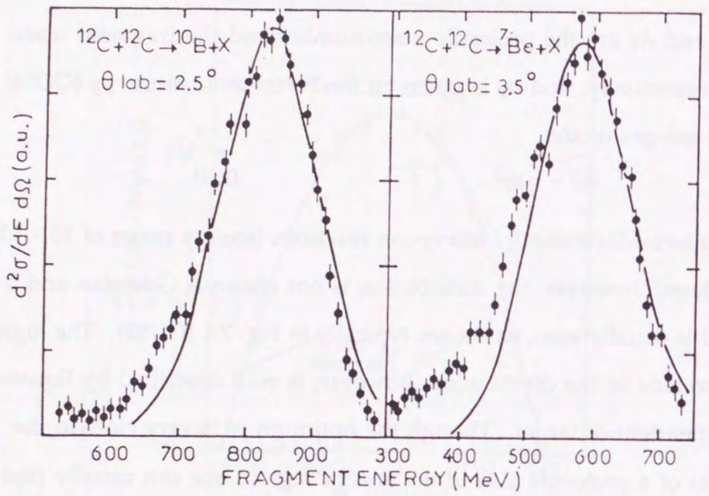

Fig. 2.4 Typical energy distribution of projectile fragments at intermediate energy. The full curves are from Equation (2.5). (GU83)

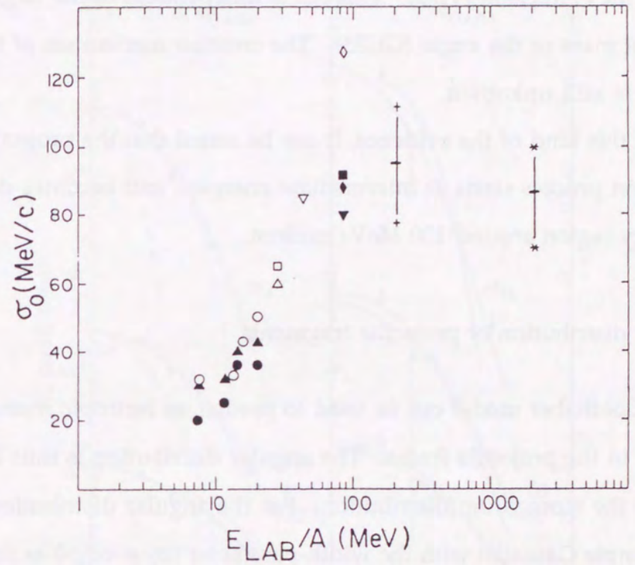

Fig. 2.5 A compilation of several different measurements of the reduced momentum width σ_0 of ejectiles from heavy-ion reactions. (MU83)

in terms of the behavior of the transfer process, due to the kinematical-matching conditions of the nucleons transferred to the target nucleus (GU85).

A low-energy tail in the momentum distribution can be seen at energies below 100 MeV/nucleon, but has not been observed at energies of around 200 MeV/nucleon (VI79). This tail is independent of the target and the fragment mass or the angle (GU83). The creation mechanism of the tail component is still unknown.

From this kind of the evidence, it can be stated that the projectile-fragmentation process starts at intermediate energies, and becomes dominant at the energy region around 100 MeV/nucleon.

2.3 Angular distribution of projectile fragments

The Goldhaber model can be used to predict an isotropic momentum distribution in the projectile frame. The angular distribution is thus basically the same as the momentum distribution. For the angular distribution, we can use a simple Gaussian with the width-parameter ($\sigma_T \equiv <\sigma_\perp>$) as follows:

$$\frac{d^3\sigma}{dp^3} \propto \exp\left\{ -\frac{{p_T}^2}{2{\sigma_T}^2} \right\}, \qquad (2.10)$$

where p_T is $<p_\perp>$.

In the relativistic energy region (around 1 GeV/nucleon) it has been found that $\sigma_T = \sigma_L$ within an accuracy of 10%, showing validity of the following equation (GR75):

$$\sigma_T \sim \sigma_L \sim \sigma_F \equiv \sigma_0 \sqrt{\frac{A_F(A_P - A_F)}{(A_P - 1)}} . \qquad (2.11)$$

On the other hand, in the energy region around 100 MeV/nucleon, the situation is different. The first experimental results concerning ^{16}O + Al/Au systems at $2^o < \theta < 8^o$ showed surprisingly large widths (Fig. 2.6) (BI79). These

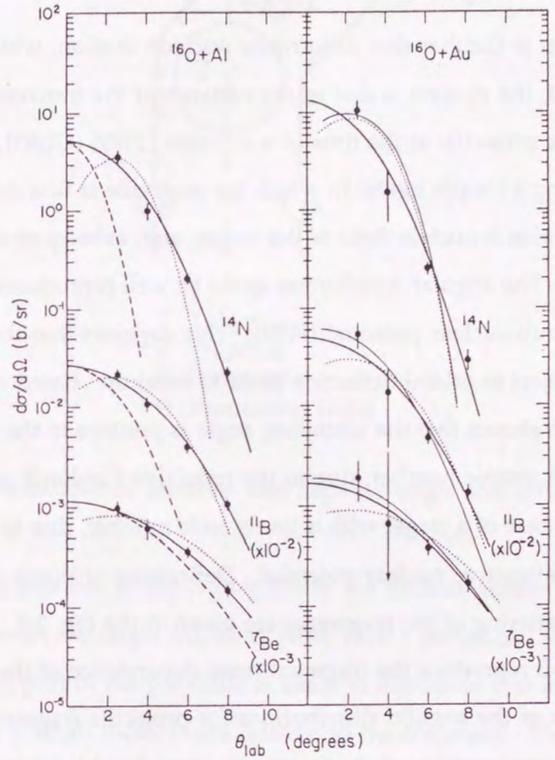

Fig. 2.6 Typical angular distribution for ^{16}O + Al, ^{16}O + Au at 92.5 MeV/nucleon. The solid curves are best fit from Equation (2.10) ; the dashed curves for σ_0 = 86 MeV/c. The dotted curves result from folding the deflection function with the momentum distribution due to the intrinsic nucleon motion ; similarly for the fine lines, but under the abrasion-ablation assumption. (BI79)

are clearly broader than a prediction from the Goldhaber model. Bibber et al. tried to explain this broadening by introducing the classical orbital deflection. The width was thus given by

$$\sigma_T^2 = \frac{A_F\,(A_P - A_F)}{A_P - 1}\,\sigma_0^2 + \left(\frac{A_F}{A_P}\right)^2 \sigma_2^2\,, \qquad (2.12)$$

where the σ_0-term is familiar due to intrinsic nucleon motion, which was already explained; the σ_2-term is due to the variance of the transverse momentum of the projectile at the time of a collision (BI79) (GU83). σ_2 can be calculated by using a simple model in which the projectile is first deflected by the combined Coulomb-nuclear field of the target, and, subsequently, fragments (BI79). The angular distribution could be well reproduced by a reasonable Coulomb-nuclear potential (BI79). This suggests that the fragments are subject to orbital deflection prior to breakup. Based on a simple calculation, it was shown that the scattering angle is positive in the case of a target with a high atomic number, due to the repulsive Coulomb potential; it is negative in the case of a target with a low atomic number, due to the relatively strong attractive nuclear potential. Definitions of positive- and negative-angle scattering of the fragments are given in the Fig. 2.7. Equation (2.12) can also well reproduce the fragment-mass dependence of the widths.

The widths of the angular distributions for projectile fragments also depend on the charge number of the fragments, even for the same mass number. The greater is the charge number, the smaller is the width of the angular distribution. Such a charge effect can be explained based on the Coulomb final-state interaction between the fragment and the protons dissociated from the projectile (WO82). One expects the fragmentation process to be a prompt peripheral process with the observed fragment being the spectator part of the parent projectile nucleus. The participant part of the

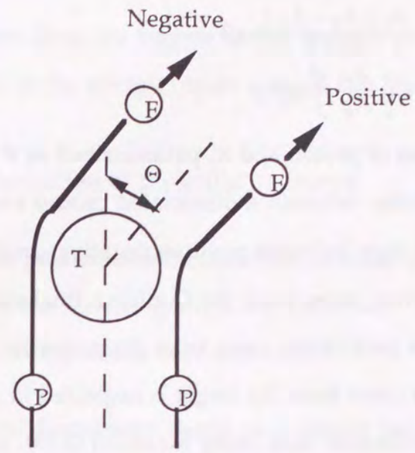

T : Target
P : Projectile
F : Fragment
Θ : Production angle

Fig. 2.7 Definitions of positive- and negative-angle scattering.

parent nucleus lies in the region where the nuclear matter of the projectile overlaps with the target nucleus. After such a peripheral encounter, the participant part of the projectile is likely to dissociate into a gas which moves with only a small momentum relative to the fragment. The Coulomb final-state interaction consists of the vector sum of all Coulomb kicks exerted between each dissociated proton in the gas and the fragment. In this model, the widths are given by

$$\sigma_T^2 = \sigma_I^2 + \sigma_{D\perp}^2 \pm \frac{\sqrt{2\,\pi}}{4}\,(Z_P - Z_F)\,C_0\,\sigma_{D\perp} + \\ + C_0^2\,(Z_P - Z_F)\left(\frac{1}{3} + \frac{(Z_P - Z_F - 1)}{8}\right) \qquad (2.13)$$

$$C_0 = \sqrt{2\,m\,Z_F\,e^2\,A_F\,/\,(A_F + 1)\,R}$$

$$\sigma_I^2 = \frac{A_F\,(A_P - A_F)}{A_P - 1}\,\sigma_0^2$$

$$\sigma_{D\perp}^2 = \left(\frac{A_F}{A_P}\right)^2 \sigma_Z^2 \ ,$$

where m is the mass of proton and R, parametrized as $R = r_0\,A_P^{1/3}$, is the mean initial separation between a dissociated proton and the fragment; the positive (negative) sign indicates positive(negative)-angle scattering. The third and fourth terms come from the Coulomb final-state interaction. It is noted that only the participant came from the projectile is taken into account and the participant came from the target is neglected in this equation. By analyzing the experimental data using Equation (2.13), we can determine the sign of the scattering angle of the projectile fragments. Wong et al. showed positive-angle scattering for a target with high and low atomic numbers in the energy region around 100 MeV/nucleon by analyzing former data for the angular distributions (WO82). This contradicts the speculation of the former work.

Recently, the scattering angle of projectile fragments in the energy region has been re-studied using the target-mass dependence of the rapidity (SI88). The peak rapidity of fragments was accurately measured for ^{16}O + Al/Au systems at $2^o < \theta < 8^o$ in the present work. A closer examination reveals an angle-dependent dumping of the peak. The consistency between the data sets for the different targets comes about upon subtracting, rather than adding, the grazing angle. This fact leads us to the following conclusion: scattering outside the grazing angle has a positive angle. The data are clearly not sufficient to explain the dumping. The transfer process may cause it. However, it is suggested that dumping may be explained in terms of the final-state interactions between the observed fragments and nucleons emitted from

the participant region, since the fragmentation process, not the transfer process, is dominant in the energy region around 100 MeV/nucleon.

2.4 Nuclear spin polarization of projectile fragments

In this chapter, polarization measurement studies used as a probe to determine the sign of the scattering angle are described. The definition of the polarization is given in Equations (3.2) and (3.3).

(a) Simple kinematical discussions based on a simple projectile fragmentation model

A calculation based on a simple projectile fragmentation model was the first theoretical work regarding this subject. Since the principle is very simple, this study is mentioned first. The formalism explained in this section was first introduced by Asahi et al. in Ref. (AS86) to calculate fragment alignment. He also applied it to fragment polarization without giving any details (AS90). They are, thus, explained here.

The model assumes that the following:

(1) The projectile-fragmentation process is well described by the participant-spectator picture.

(2) The participant part already exists in the projectile nucleus, and is prepared for removal prior to the collision. However, this assumption may not necessarily mean that the parts must form a cluster in the strict sense.

In addition to the assumptions described above, the model also assumes the peripheral nature of the collision for projectile-fragmentation process.

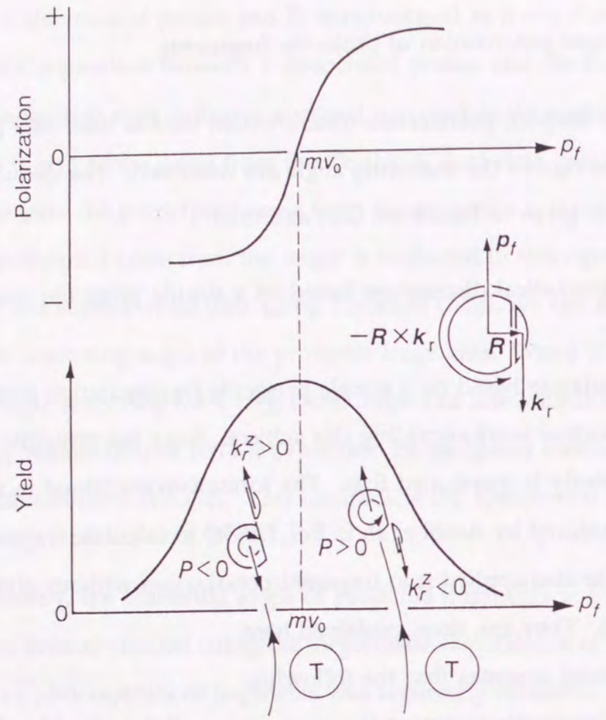

Fig. 2.8 Schematic diagram of correlation between P and p_f predicted from a model of projectile fragmentation. See text for notations.

Under these assumptions, the projectile nucleus is divided into two parts: the participant part and the spectator part. As indicated in the small insert of Fig. 2.8, the linear momentum (p_f) and the angular momentum ($R \times p_f$) of projectile fragments are supposed to be strongly connected; they are directly connected to those of the participant part through the momentum- and angular momentum-conservation laws. As is indicated in Fig. 2.8, a fragment whose velocity is larger than the projectile velocity is formed when a cluster moving in the backward direction in the projectile frame at the instance of a collision is removed. In this case, the spectator fragment must have the angular momentum given in the right-hand side of the figure. The polarization is thus positive when we assume a positive deflection, as shown in the figure, where the polarization parallel to the vector $p_i \times p_f$ is defined so as to be positive; p_i and p_f are the momenta of incoming and out going particles. On the other hand, for a fragment whose velocity is smaller than that of the projectile, the above discussion is reversed, and the sign of the polarization is negative. The momentum dependence of the polarization, where the polarization is positive for the higher side of the momentum distribution and negative for the lower side of the distribution, will thus be observed for positive-angle scattering; negative-angle scattering gives a reversed tendency.

The polarization in such a process is calculated using the Wigner transform of the one-body density matrix as follows. The axis of the polarization (quantization axis) is perpendicular to the beam axis in the system, as shown in Fig. 2.9. The consideration can be elaborated as follows into a quantitative form by taking an expression derived in Ref. (HÜ81) for the production of a fragment with a longitudinal momentum $k_{//}$:

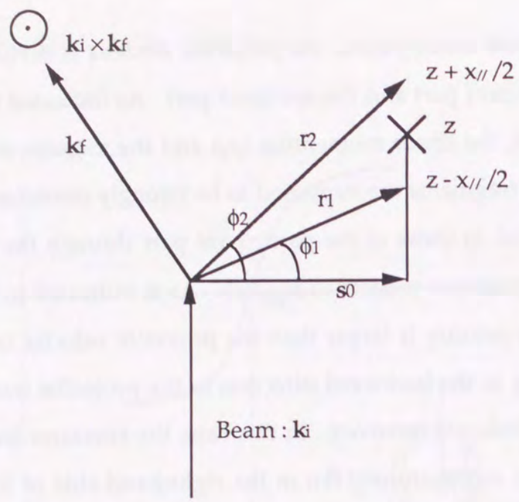

Fig. 2.9 Coordination of polarization.

$$\frac{d\sigma}{dk_{//}} = \int d^2 s\, D(s) \int dz \int d^2 k_{//}\, W(s, z, k_{\perp}, k_{//}) \ , \qquad (2.14)$$

where the momentum vector ($k = (k_{\perp}, k_{//})$) of the removed cluster is decomposed into a $k_{//}$ component parallel to the beam direction and a transverse part, $k_{\perp}$; the position vector ($R = (s, z)$), at which cluster removal takes place, is decomposed into z and s in the same manner. In the above expression for the fragmentation cross-section, the Wigner transform ($W_m(R, k)$) of the one-body density matrix ($\langle r|\rho|r'\rangle$), defined by

$$W_m(R, k) = \int \frac{d^3 x}{(2\pi)^3} \exp(-i k x) \left\langle R - \frac{x}{2} \middle| \rho \middle| R + \frac{x}{2} \right\rangle$$
$$= \int \frac{d^3 x}{(2\pi)^3} \exp(-i k x)\, \Phi_m(s, z - \frac{x}{2})\, \Phi_m^*(s, z + \frac{x}{2}) \ , \quad (2.15)$$

represents the "probability" for finding a particle at position R and momentum p. Using this equation, the production of a fragment is given by

$$\frac{d\sigma_m}{dk_{//}} = \int d^2 s\, D(s) \int dz \int \frac{d x_{//}}{2\pi} \exp(-i k x)\, \Phi_m(s, z - \frac{x_{//}}{2})\, \Phi_m^*(s, z + \frac{x_{//}}{2}) \ .$$

(2.16)

The weighting function ($D(s)$) contains the collision dynamics, and confines the process of the nucleon removal to the region of the nuclear surface. Since the form $D(s) = \delta(s - s_0)$ was assumed for the weighting function, the equation was changed to

$$\frac{d\sigma_m}{dk} = \int dz \int \frac{d x}{2\pi} \exp(-i k x)\, \Phi_m(s_0, z - \frac{x}{2})\, \Phi_m^*(s_0, z + \frac{x}{2}) \ , \quad (2.17)$$

where we have replaced $k_{//}$ ($x_{//}$) by $k = |k|$ ($x = |x|$) for simplicity.

As an example, we consider the case that a nucleon is removed from the 1d orbit of the projectile. For simplicity, we assume no intrinsic spin for the nucleon. By describing this orbit by a harmonic-oscillator wave function, we obtain the following expression for the momentum distribution:

$$\frac{d\sigma}{dk} = \sum_m \frac{d\sigma_m}{dk}$$
$$= N \exp[-(b k)^2] \left[\left\{ \left(\frac{k}{\Gamma} \right)^2 + 2 - \left(\frac{b}{s_0} \right)^2 \right\}^2 - 3 + 3 \left(\frac{b}{s_0} \right)^2 \right], \quad (2.18)$$

where $d\sigma_m/dk$ denotes the cross-section for orbit m of the angular momentum $l = 2$; N is a normalization constant. The width (Γ) of the distribution is expressed as $\Gamma = s_0 / b^2$, where b denotes the oscillator parameter for the wave function. Noting that the angular momentum remaining in the fragment nucleus is opposite to that of the removed nucleon, the spin polarization (P) is calculated as

$$P = \left(\frac{d\sigma_{-2}}{dk} - \frac{d\sigma_{+2}}{dk} \right) \Big/ \left(\frac{d\sigma}{dk} \right)$$
$$= 3 \frac{k}{\Gamma} \left[\left(\frac{k}{\Gamma} \right)^2 + 1 - \left(\frac{b}{s_0} \right)^2 \right] \Big/ \left[\left(\left(\frac{k}{\Gamma} \right)^2 + 2 - \left(\frac{b}{s_0} \right)^2 \right)^2 - 3 + 3 \left(\frac{b}{s_0} \right)^2 \right]. \quad (2.19)$$

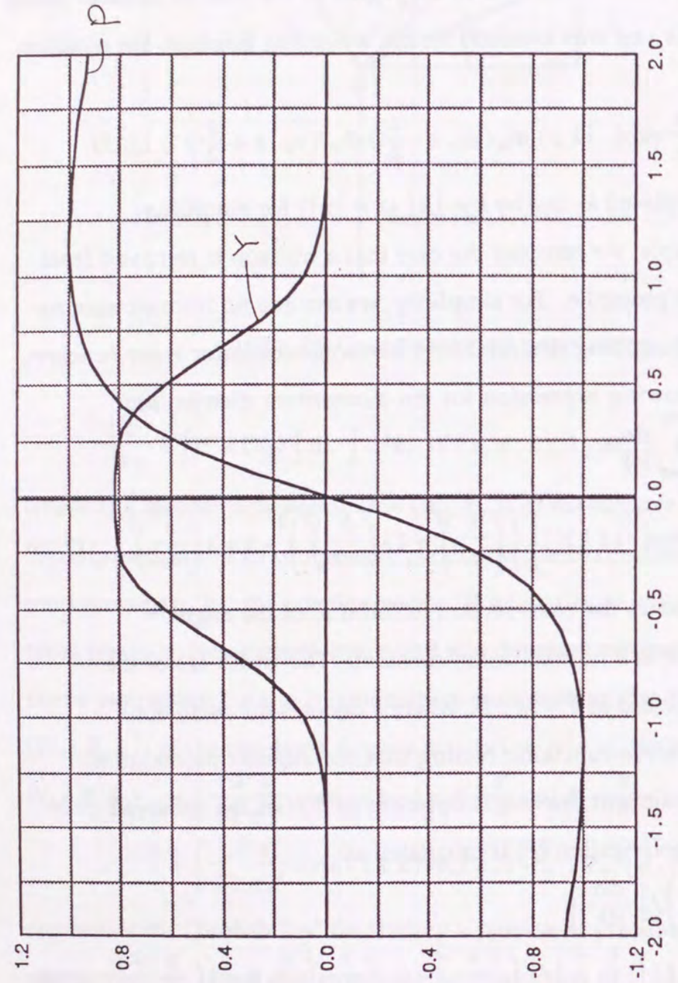

Fig. 2.10 Typical prediction from a simple projectile fragmentation model ; The momentum distribution and the polarization of nuclei on 1d state.

The quantitative behaviors of the cross-section and polarization as a function of k are shown in Fig. 2.10, where we chose the parameter r, s_0, b and Γ as follows: $s_0 = r = 4.45$ fm, $b = 2.18$ fm and $\Gamma = 0.936$ fm^{-1}. The above discussion is similar, even for an actual nucleon which has intrinsic spin, as well as for other orbits. (See Appendix 4 for detailed calculations.) It was shown that the sign of the scattering angle can be determined from the momentum dependence of the fragment polarization.

(b) Microscopic simulation method

A more sophisticated theoretical calculation based on microscopic-simulation methods from quantum molecular dynamics (QMD) (PE89) has also been used to predict the polarization of projectile fragments (OH92). In the case of peripheral collisions, like the projectile-fragmentation process, the mean field of the target nucleus was assumed. This treatment is called a "quantum molecular dynamics + an external mean field" model. In this model, the two nuclei interact through this mean field as well as stochastic 2-nucleon collisions. The Gogny interaction (OH92) is used as the effective nuclear-force, and the target mean field is constructed by the folding potential of the Gogny interaction. Since the total angular momentum is not conserved with the usual treatment of the 2-nucleon collision term, it is restored by a uniform rotation of the total system. The recoil effect of the target nucleus is also taken into account.

Typical calculation results are given in Fig. 2.11. The momentum dependence and the projectile polarization in ^{15}N induced reactions are also shown in the figure. In the case of a 40 MeV/nucleon ^{15}N+^{197}Au reaction, the momentum dependence of the polarization is almost consistent with that predicted from simple kinematical discussions based on a simple projectile

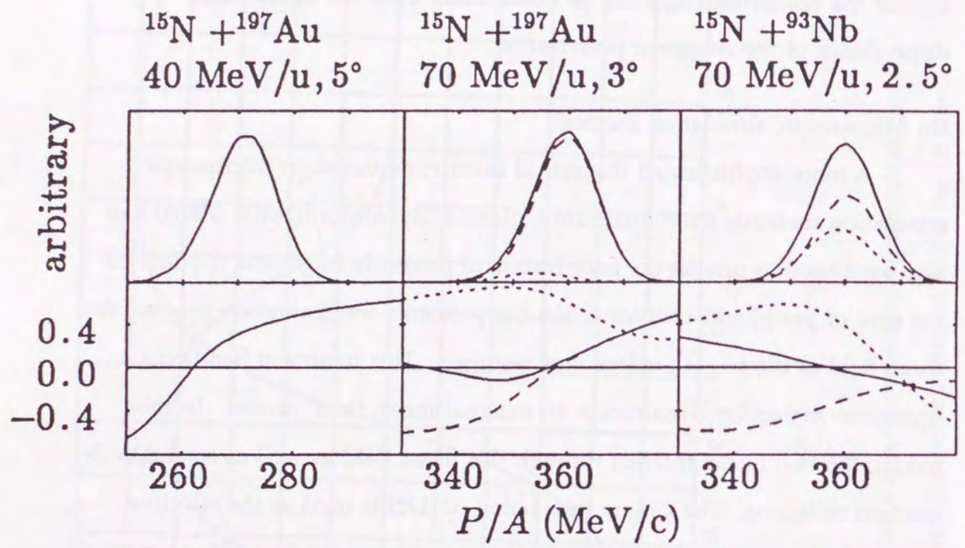

Fig. 2.11 Typical prediction from microscopic simulation methods ; The momentum distribution (upper) and the polarization (lower) of mass number = 14 nuclei produced in the ^{15}N induced reactions. The dashed, dotted, and solid lines show the near-, far-side contribution, and their average, respectively.

fragmentation model. At 70 MeV/nucleon, however, the far-side component (the component of negative-angle scattering) cannot be neglected, even though the cross-section is still small. The far-side component has a large positive polarization, since the contact time is long and the ejectile has sufficient time to absorb the relative angular momentum. Thus, a dip appears as the result of the mixing. In the 70 MeV/nucleon ^{15}N+^{93}Nb reaction, fragment polarization is dominated by the far-side component, and the slope becomes negative. These tendencies are basically consistent with predictions from a simple projectile fragmentation model.

Chapter 3. Principle of nuclear polarization measurements

We had to measure the polarization of the heavy ^{37}K, ^{39}Ca and ^{43}Ti projectile fragments, which are all short-lived β-radioactive nuclei. Among the many methods used for measuring the nuclear polarization, the nuclear magnetic resonance (NMR) probed by the asymmetric emission of β-rays (β-NMR technique) is best because of its effectiveness and reliability. This method has several advantages, i.e., an analyzing power of $A \sim 1.0$, and reliability in cancelling geometrical asymmetry of the detection system. We can thus measure the nuclear polarization with high precision.

3.1 β-NMR technique

3.1.1 Asymmetric β-decay

Basically the nuclear polarization can be detected by the asymmetric emission of β-rays when the nucleus is a β-emitter and its nuclear spin (I) is not zero. Due to parity non-conservation in a weak interaction, the general β-ray angular distribution for nuclear polarization is given as (HO76)

$$W(\theta) = 1 + \mathcal{A} P \frac{v}{c} \cos\theta \ , \qquad (3.1)$$

where P is the nuclear polarization and $\mathcal{A}$ is the asymmetry factor; θ is the polar angle of the β-ray relative to the polarization direction and (v/c) is the β-ray velocity divided by the light velocity, which is omitted later since it is very close to that for the present β-ray energy.

The spin polarization (P) for the ensemble of a spin I object is defined in terms of the population of the magnetic sublevel (a_m) as follows:

$$P = \sum_{m=-I}^{I} a_m \, m \ / \ I \ , \qquad (3.2)$$

where a_m is normalized as

$$\sum_{m=-I}^{I} a_m = 1. \qquad (3.3)$$

In the V-A approximation the asymmetry factor ($\mathcal{A}$) is given by

$$\mathcal{A} = \pm \lambda_{jj_1} \frac{|C_A|^2 |\int \boldsymbol{\sigma}|^2}{|C_V|^2 |\int \mathbf{1}|^2 + |C_A|^2 |\int \boldsymbol{\sigma}|^2} - 2\,\delta_{jj_1} \left(\frac{j}{j+1}\right)^{1/2} \frac{(C_A)(C_V) \int \boldsymbol{\sigma} \int \mathbf{1}}{|C_V|^2 |\int \mathbf{1}|^2 + |C_A|^2 |\int \boldsymbol{\sigma}|^2} \quad \text{for } \beta^{\pm} \qquad (3.4)$$

$$\lambda_{jj_1} = 1 \quad \text{for} \quad j \Rightarrow j_1 = j - 1 \qquad (3.5)$$
$$= \frac{1}{j+1} \quad \text{for} \quad j \Rightarrow j_1 = j$$
$$= -\frac{j}{j+1} \quad \text{for} \quad j \Rightarrow j_1 = j + 1 \ ,$$

where j and j_1 indicate the total angular momentum of the initial and final states respectively; $\int \mathbf{1}$ and $\int \boldsymbol{\sigma}$ are the Fermi and Gamow-Teller matrix elements; C_A and C_V are coupling constants with the subscripts being the vector and axial vectors, respectively (MO73). If decay mode is pure of the Gamow-Teller type, $\mathcal{A}$ becomes even simpler,

$$\mathcal{A} = \pm \lambda_{jj_1} \ , \qquad \text{for } \beta^{\pm} \ . \qquad (3.6)$$

The Fermi matrix element is given by

$$\int \mathbf{1} = [\, T(T+1) - T_{zi}\, T_{zf} \,]\, \delta_{if}\, (1 - \varepsilon) \ , \qquad (3.7)$$

where T is the isospin; T_{zi} and T_{zf} are the z-components of the initial- and final-state isospins, respectively; δ_{if} allows the Fermi transition to take place only between nuclear analog states. The quantity $(1 - \varepsilon)$ is the conventional correction for the Fermi decay by which the reduction in the overlap between the initial and final nuclear wave functions due to isospin mixing is taken into account. The free nucleon value for C_A/C_V can be obtained from the

mixed Fermi/Gamow-Teller decay of the neutron. The calculations are based on a 1982 analysis of Wilkinson (WI82), which gave

$$| C_A/C_V | = 1.2606 \pm 0.0075 . \qquad (3.8)$$

Thus, if $\int \boldsymbol{\sigma}$ can be estimated, we can calculate the asymmetry factor from Equation (3.4).

$|\int \boldsymbol{\sigma}|$ can be obtained from the β-decay *ft*-value of the nuclei. The expression incorporates both the phase-space factor (*f*) and the constant (*K*),

$$f t_{1/2} = K / [\, C_V^2 \, | \int \mathbf{1} \, |^2 + C_A^2 \, | \int \boldsymbol{\sigma} \, |^2 \,], \qquad (3.9)$$

where $t_{1/2}$ is the partial half-life of the nuclei. The *ft* value can be calculated from the β-decay *Q* value, the total half-life and the branching ratio. The sign of $\int \boldsymbol{\sigma}$ can be determined by either shell-model calculations or magnetic-moment systematics.

The asymmetry factor of ^{43}Ti is shown here as an example. The data necessary for such a calculation as the β–decay half-life, the branching ratio and the *Q* value are given by (HO87). In this nuclei, a ground-to-ground transition is main path; it is of the mixed Fermi/Gamow-Teller type. Other β-decay transitions are weak, and are of the pure Gamow-Teller type. Ref. (BR85) was adopted as the best method to calculate the phase-space factor. We thus obtained the asymmetry factor of each transition. Finally, by taking average of each asymmetry factor, we obtained -0.72 for ^{43}Ti. Asymmetry factors for ^{37}K and ^{39}Ca could be calculated in a similar way, and are given by -0.57 and +0.83, respectively, as summarized in Table 3.1.

Thus, in order to evaluate the polarization, we measured the β-rays using two sets of counter telescopes placed above and below the reaction plane, i.e., in the direction of θ=0° and θ=180°. The ratio *R* of the counting rate is thus given by

	^{37}K		^{39}Ca	^{43}Ti	
Transition	$3/2^+ \Rightarrow 3/2^+$	$3/2^+ \Rightarrow 5/2^+$	$3/2^+ \Rightarrow 3/2^+$	$7/2^- \Rightarrow 7/2^-$	$7/2^- \Rightarrow 5/2^-$
Decay mode	β^+		β^+	β^+	
Interaction type	Mixed GT and F	Pure GT	Mixed GT and F	Mixed GT and F	Pure GT
Half life	1.226(7) sec		859.6(14) msec	509(5) msec	
Branching ratio	98.2(3) %	1.8 (3) %	~ 100 %	90.2(8) %	9.8(8) %
β-ray energy	5.13 MeV	2.33 MeV	5.51 MeV	5.85 MeV	5.00 MeV or less
Asymmetry factor	-0.573	-0.400	+0.83	-0.777	-0.222
Effective $\mathcal{A}$ factor	-0.57		+0.83	-0.72	

Table 3.1 β-decay information for ^{37}K, ^{39}Ca and ^{43}Ti (EN90).

$$R = \frac{W(\theta=0^{o})}{W(\theta=180^{o})} = \frac{1 + \mathcal{A} P}{1 - \mathcal{A} P} \sim 1 + 2\,\mathcal{A} P\,. \qquad (3.10)$$

Using the calculated asymmetry factor, we can evaluate the magnitude of the polarization.

3.1.2 Nuclear Magnetic Resonance (NMR)

Although the polarization can be measured basically through asymmetric β-ray emission, we need a reliable method to cancel the geometrical asymmetry of the counter system for a precise determination of the polarization. The most reliable way to do this is to invert the polarization by means of the NMR technique.

Nuclear magnetic resonance (NMR) was developed by Purcell et al. (PU46). In a classical picture, the magnetic moment in a magnetic field (H_0) rotates around the field with a Larmor frequency (ω_L) given by

$$\omega_L = \gamma H_0\,, \quad \gamma = \frac{\mu}{I\,\hbar} = \frac{g}{\hbar}\,\mu_N\,. \qquad (3.11)$$

Here, μ is the magnetic moment (see Fig. 3.1), γ the gyromagnetic ratio, g the g-factor of the nuclei, I the nuclear spin and μ_N the nuclear magneton. The quantum-mechanic energy levels of nuclei are split in terms of their magnetic sublevels, as shown in Fig. 3.3. When a photon having the same energy, with the energy difference between these levels, is supplied from a rf (radio frequency) magnetic field, transitions between these levels occur and the direction of the magnetic moment is changed, under the following condition:

$$\hbar\,\omega = g\,\mu_N H_0\,|\Delta m| \equiv \hbar\,\omega_L |\Delta m| \qquad \Delta m = m - m' = \pm 1\,, \quad (3.12)$$

where m denotes the magnetic sublevels.

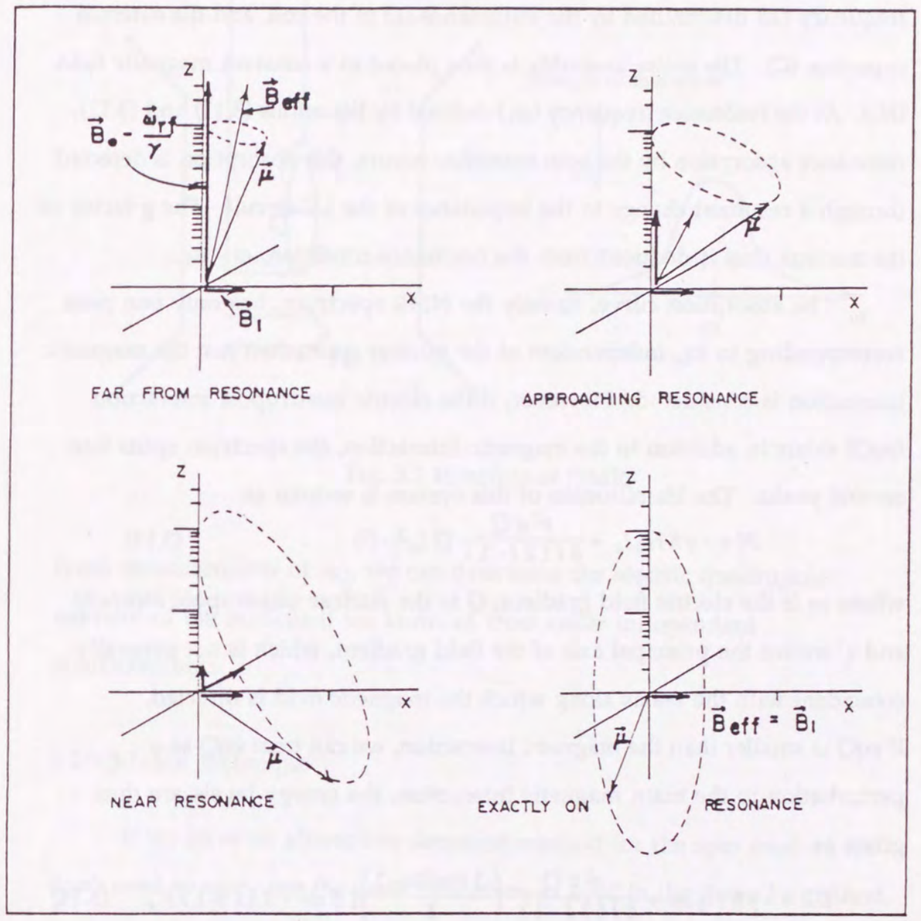

Fig. 3.1 Schematic views explaining precession of the magnetic moment μ. Four cases depicting precession of the magnetic moment about the effective field $\mathbf{B}_{eff}$. Exactly on resonance, $\mathbf{B}_{eff} = \mathbf{B}_1$ (RO86).

The principle of the NMR technique developed by Purcell et al. is indicated in Fig.3.2. Material is placed in an rf coil which is tuned for the frequency (ω) determined by the inductance (L) of the coil, and the external capacitor (C). The entire assembly is then placed in a constant magnetic field (H_0). At the resonance frequency (ω_L) defined by Equations (3.11) and (3.12), resonance absorption by the spin ensemble occurs; this absorption is detected through a resultant change in the impedance of the LC-circuit. The g-factor of the nucleus thus is deduced from the resonance condition, $\omega = \omega_L$.

The absorption curve, namely the NMR spectrum, has only one peak corresponding to ω_L, independent of the nuclear spin when just the magnetic interaction is considered. However, if the electric quadrupole interaction (eqQ) exists in addition to the magnetic interaction, the spectrum splits into several peaks. The Hamiltonian of this system is written as

$$\mathcal{H} = - \gamma \hbar H_0 I_z + \frac{e^2 q Q}{4 I (2 I - 1)} (3 I_{z'}^2 - I^2) , \qquad (3.13)$$

where eq is the electric field gradient, Q is the nuclear quadrupole moment and z' means the principal axis of the field gradient, which is not generally coincident with the z-axis along which the magnetic field is directed.
If eqQ is smaller than the magnetic interaction, we can treat eqQ as a perturbation to the main magnetic interaction; the energy levels are thus given as

$$E_m = - \gamma \hbar H_0 m + \frac{e^2 q Q}{4 I (2 I - 1)} \left(\frac{3 \cos^2\theta - 1}{2} \right) [3 m^2 - I (I + 1)] , \qquad (3.14)$$

where θ is the angle between the z- and z'- axis. The energy levels therefore split as shown in Fig. 3.3. Here, ω_Q is given by

$$\omega_Q = \frac{e^2 q Q}{4 \hbar} = 2\pi \nu_Q . \qquad (3.15)$$

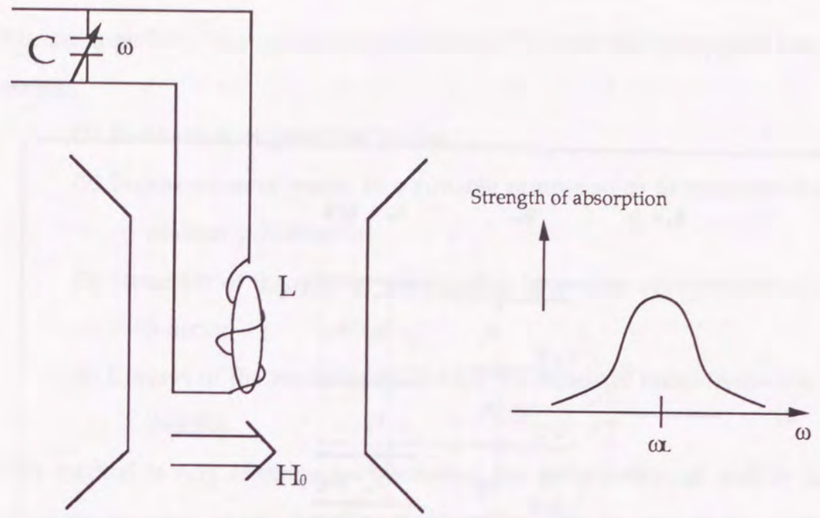

Fig. 3.2 Principle of NMR.

From measurements of ω_Q, we can determine the electric quadrupole moment of the nucleus if we know eq from other independent measurements.

3.1.3 β-NMR technique

If we have an alternative detection method for the spin motion, we don't need to carry out the same procedure as used in the Purcell's method. Such a method involves using the asymmetric emission of β-rays described in the preceding section. An ambitious technique, called β-NMR, was initiated by Sugimoto, and then developed by Minamisono (SU65) (MI73). In this method, the spin motion is detected by the β-ray asymmetry from polarized nuclei, so that it can be detected, even for a very low concentration,

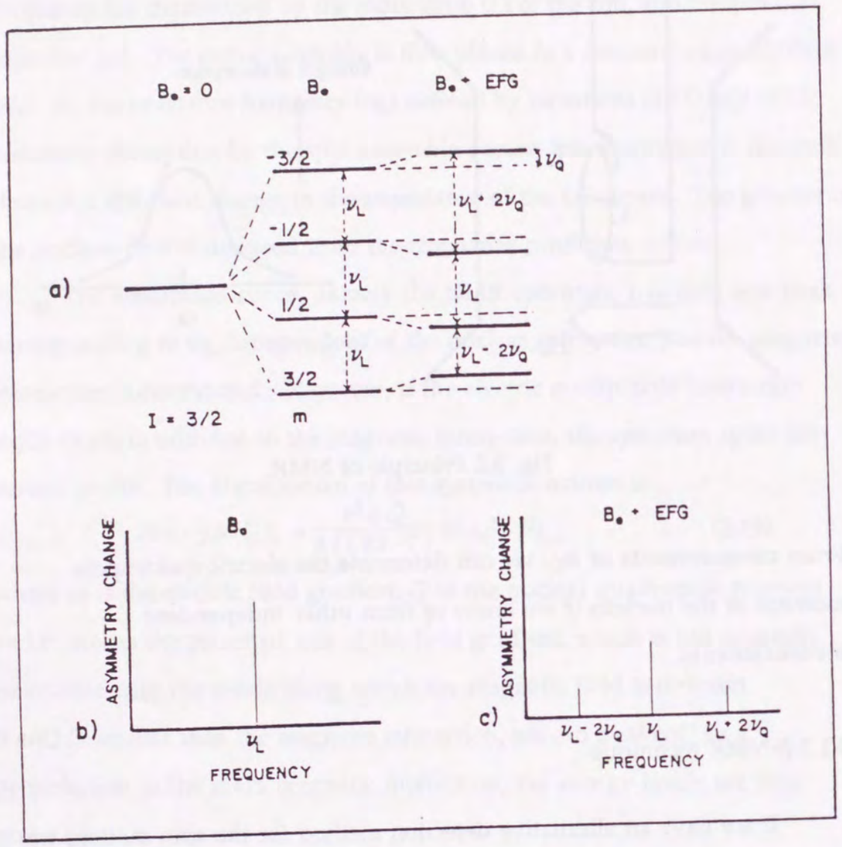

Fig. 3.3 a) Magnetic sublevels for a spin 3/2 nucleus with magnetic and electric quadrupole interactions. b) Change in β-decay asymmetry at resonance for B field alone, c) splitting of resonance line by addition of the electric field gradient and quadrupole coupling (RO86).

like an impedance change of a rf-coil circuit. This method comprises four stages:

(1) Production of polarized nuclei.

(2) Implantation of nuclei to a suitable sample so as to maintain the nuclear polarization.

(3) Detection of the nuclear polarization by means of asymmetric β-decay.

(4) Control of the nuclear polarization by means of radio-frequency (NMR).

This method is very effective for measuring the polarization, as well as the magnetic moment, of any β-radioactive nucleus. The success of this method depends on production of polarized nuclei, and the maintenance of the polarization during their lifetimes.

3.1.4 Adiabatic fast passage (AFP) method

Adiabatic fast passage is one of effective methods for the NMR technique (AB61). It is possible to invert the nuclear spin by this method. This method was introduced to the β-NMR technique by Minamisono (MI73).

The magnetic moment (μ) precesses around the external static magnetic field with a Larmor frequency of $\nu_L = \omega_L/2\pi$. When a linear rf magnetic field ($2H_1\cos\omega\tau$) is induced perpendicular to the external static magnetic field, the magnetic moment (μ) precesses around an effective magnetic field, i.e., the external magnetic field (H_0) is reduced by (ω/γ) and H_1.

(Note that the effective rotating strength (H_1) obtained by the linear field, $2H_1\cos\omega t$, is $|H_1 e^{i\omega t}| = H_1$.)

This phenomenon can be intuitively understood in a rotating coordinate system which rotates simultaneously with H_1. In this coordination the strength of the reduced external magnetic field (H_0') is

$$H_0' = H_0 - \omega/\gamma \ . \qquad (3.16)$$

The magnetic moment (μ) precesses around the effective magnetic field, ($H_{eff} = H_0' + H_1$) with a Larmor frequency of $\omega_L' = \gamma H_{eff}$.

(Note that H_1 becomes a static magnetic field in the coordination.)

The strength of H_{eff} is given by

$$| H_{eff} | \equiv \sqrt{H_1^2 + H_0'^2} = \sqrt{H_1^2 + (H_0 - \omega/\gamma)^2} \ . \qquad (3.17)$$

The angle θ between H_1 and H_{eff} is written as

$$\theta = \tan^{-1}\left(\frac{H_0 - \omega/\gamma}{H_1}\right). \qquad (3.18)$$

This situation is illustrated in Fig. 3.4.

By scanning the rotating angular velocity (ω) from $\omega_i < \gamma H_0$ to $\omega_f > \gamma H_0$ through the resonance angular velocity ($\omega_0 = \gamma H_0$), the direction of H_{eff} is changed from parallel to H_0 to anti parallel to H_0. If the change in the rotation of the angular velocity of dH_{eff}/dt is sufficiently slower than ω_L', the magnetic moment (μ) follows H_{eff}. This phenomenon represents the adiabatic fast passage (AFP). The change in the rotation of the angular velocity of H_{eff} is estimated to be $d\theta/dt$. Near the resonance angular-velocity ($\omega_0 = \gamma H_0$,) the quantity $d\theta/dt$ is written as

$$\frac{d\theta}{dt} = \frac{d}{dt}\left(\frac{H_0 - \omega/\gamma}{H_1}\right) = -\frac{1}{\gamma H_1}\frac{d\omega}{dt}, \qquad (3.19)$$

and ω_L' is

$$\omega_L' = \gamma H_{eff} = \gamma\sqrt{H_1^2 + (H_0 - \omega/\gamma)^2} \ . \qquad (3.20)$$

The condition of AFP $\omega_L' \gg d\theta/dt$ is thus rewritten according to following equation:

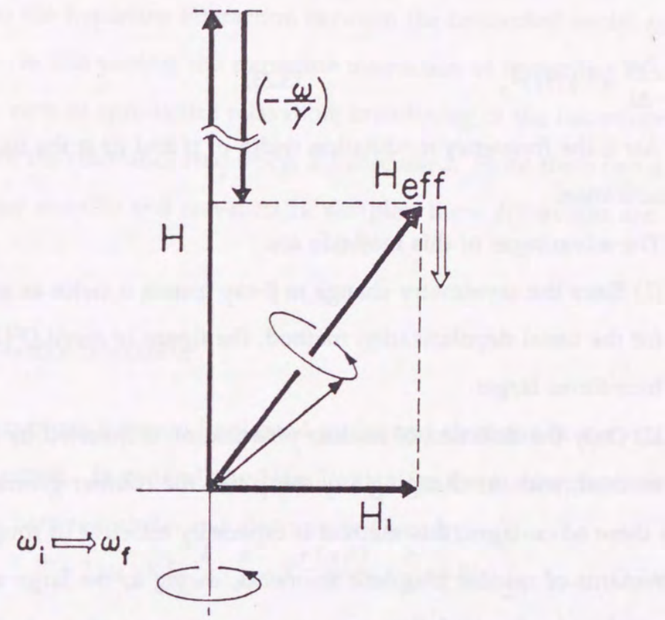

Fig. 3.4 Schematic views explaining the adiabatic fast passage (AFP) (MI73).

$$-\frac{1}{\gamma H_1}\frac{d\omega}{dt} \ll \gamma\sqrt{H_1^2 + (H_0 - \omega/\gamma)^2}\ . \qquad (3.21)$$

Near to the resonance, H_0 is nearly equal to ω_0/γ. Then, the AFP condition is again rewritten as either

$$-\frac{1}{\gamma H_1}\frac{d\omega}{dt} \ll \gamma H_1 \qquad (3.22)$$

or

$$\frac{\Delta\omega}{\Delta t} \ll (\gamma H_1)^2\ , \qquad (3.23)$$

where $\Delta\omega$ is the frequency modulation width of rf and Δt is the time period of the modulation.

The advantages of this methods are:

(1) Since the asymmetry change in β-ray counts is twice as much as that for the usual depolarization method, the figure of merit ($P^2 N$) becomes four-times larger.

(2) Only the direction of nuclear polarization is inverted by this method, without changing any setup like the counter geometry.

Due to these advantages, this method is especially effective in rough measurements of nuclear magnetic moments, owing to the large asymmetry change and wide rf modulation.

The effectiveness of the AFP was first shown in measurements of the ^{8}B nuclear magnetic moment (MI73). In this experiment, the asymmetry change (which was originally only 3% according to the usual depolarization method) was enhanced to 6% by means of AFP.

3.2 Hyperfine interaction of implanted nuclei

The selection of host material is very important for the NMR-measurements because the maintained polarization, the shift of the resonance frequency and the broadening of the width of NMR spectrum depend on the hyperfine interaction between the implanted nuclei and host materials. In this section, the hyperfine interaction of impurities in catcher materials, such as spin-lattice relaxation, broadening of the resonance width and shift of the resonance frequency, are discussed. Since these items are different for metallic and non-metallic samples, these differences are also described.

3.2.1 Spin-lattice relaxation

Interactions between implanted nuclei and electrons in a crystal can cause relaxation. In general, the Hamiltonian for the electromagnetic interaction between nuclei and electrons is given by

$$\mathcal{H} = 2\,\mu_B\,\gamma\hbar\,I\left[\frac{l}{r^3} - \frac{s}{r^3} + 3\frac{r(s\,r)}{r^5} + \frac{3}{8}\pi\,s\,\delta(r)\right], \qquad (3.24)$$

where μ_B is the Bohr magneton, I is the nuclear spin, l and s are the orbital and intrinsic spin of electrons (AB61). Although in free space this interaction becomes very large, in the case of a diamagnetic sample, it is reduced because of the disappearance of orbital angular momentum.

The spin-lattice relaxation and the shift in the resonance frequency (Knight shift) in metals are caused by the conduction S electrons. They are associated with the well-known following Korringa relation:

$$T_1\left(\frac{\Delta H}{H}\right)^2 = \frac{\hbar}{4\,\pi\,k\,T}\frac{\gamma_e^2}{\gamma_n^2}, \qquad (3.25)$$

where γ_e and γ_n denote the spin g-factors of the electrons and nuclei, respectively; $\Delta H/H$ denotes the Knight shift; and T_1 denotes the spin-lattice relaxation time. From the relation, the relaxation time (T_1) is expected to be inversely proportional to the temperature (T). In order to make the relaxation time longer, it is necessary to make the temperature low.

On the other hand, in the case of insulators, the spin-lattice relaxation time is not given by a simple relation, like Equation (3.25). It is found that the spin-lattice relaxation time in pure metal is larger than 10^2 seconds at room temperature (GL49). It is understood that the paramagnetic impurity in the crystal is the main cause of relaxation (GL49). In the present study the lattice defects produced in crystals during the implantation process may have also caused the relaxation, since defects may cause fluctuation in the local magnetic field and/or electric field, thus destroying the nuclear polarization (MI87).

3.2.2 Line broadening

The implanted nucleus is surrounded by many host nuclei. Such surrounding nuclei cause a local magnetic field. The fluctuation in the local magnetic field causes a broadening of the width of resonance.

The magnetic dipole interaction is given by Ref. (AB61) as

$$\mathcal{H}_{12} = \frac{\gamma_1 \gamma_2 \hbar^2}{r_{12}^3} \left[I_1 I_2 - 3 \frac{(I_1 r_{12})(I_2 r_{12})}{r_{12}^2} \right], \qquad (3.26)$$

where r_{12} is the vector connecting two spins. The dipolar broadening ($\overline{\Delta\omega}$) is thus given as

$$(\overline{\Delta\omega})^2 = \frac{1}{3} \gamma_I^2 \gamma_S^2 \hbar^2 S(S+1) \sum_i \frac{(3\cos^2\theta_i - 1)^2}{r_i^6}, \qquad (3.27)$$

where γ_I and γ_S are gyromagnetic ratios of the implanted and host nuclei, respectively; θ_i indicates angle between their direction; and the magnetic field (H_0), r_i denotes the distance between them. A sum should be taken over the surrounding nuclei (VA48). Dipolar broadening is associated with the spin-spin relaxation time (T_2) as

$$\frac{1}{\pi T_2} = \overline{\Delta\omega}. \qquad (3.28)$$

In addition to the magnetic interaction between the implanted nuclei and surrounding nuclei, eqQ causes line broadening if implanted nuclei have a quadrupole moment. There are some causes to generate a local electric field gradient, such as the creation of lattice defects during the implantation processes and a local lattice effect caused by impurities. However, it is not easy to estimate the broadening.

3.2.3 Chemical shifts

An implanted nucleus is affected by many local magnetic and electric fields in addition to the experimental magnetic field for the NMR, as discussed in previous sections. These fields can cause a shift in the resonance frequency.

In the case of a metallic sample, the main cause of the shift is the magnetic field generated by conduction electrons. This shift is known as the Knight shift. The measured Knight shift is of the order of 0.01% ~ 1%; the shift depends on the concentration of implanted nuclei.

Even in the case of an insulator, we must still consider the diamagnetic effects due to the rotation of electrons around the nuclei (FE68). The contribution from polarization of the atomic spin induced by the external

magnetic field, known as paramagnetic shielding, also causes a shift. Due to these magnetic fields, the total magnetic field is changed to

$$H = H_0 (1 - \sigma) , \qquad (3.29)$$

where H_0 denotes the external magnetic field and σ is equivalent to the shift of the resonance frequency. σ, called the chemical shift, is independent of the external magnetic field and is of the order of $10^{-4} \sim 10^{-2}$.

Chapter 4. Experimental apparatus

In this chapter the experimental setup used for the present study is described. Beam line 44 was built at the Bevalac of the Lawrence Berkeley Laboratory as a fragment separator. It has been used for the separation of ^{37}K, ^{39}Ca and ^{43}Ti fragments. The general specifications of the separator are outlined in Section 4.1, and beam-line parameters are described in Section 4.2. Detailed methods for tuning the separator and the identification technique of the fragments are explained in Section 4.3. The setup for the β-NMR technique is explained in Section 4.4.

4.1 Fragment Separator (Beam line 44 at the Bevalac)

Since many projectile fragments are produced in the projectile-fragmentation process at the same time, we must generally separate the desired fragments in general. In addition, we must observe the β-decay of the fragments for the polarization measurement. Since β-decay is a slow process, we can not tag the nuclei by the event-by-event record, as is often done for the rejection of unwanted events. Separation of the fragments is therefore necessary for the present study in a strict meaning. For these reasons, our group developed and improved a fragment separator: Beam line 44 (B44) at the Bevalac of Lawrence Berkeley Laboratory (TA89) (MA89).

The separation of fragments was achieved by a rigidity analysis and a range or energy-loss analysis. Since the velocities of the fragments are very close to that of the primary beam (as discussed in Chapter 2) rigidity analysis separates the fragments based on the A/Z ratio of the fragments. It was made by a dipole magnet located just after a target and a pair of slit jaws located at

the focus of the magnet (see Fig. 4.1). In order to select only the desired nuclei from all nuclei with the same rigidity (namely, the same A/Z ratio) an energy-loss or range analysis was carried out in addition to the rigidity analysis. The energy-loss analysis was carried out using an energy degrader and a dipole magnet. By passing through the energy degrader with a proper thickness, nuclei with the same rigidity lose their rigidity depending on their species, and based on their $Z^{2\gamma 2}/A^{2\gamma 1}$; γ is a constant which is determined by the absorber material. By the combined analysis, only one nucleus is separated out (Fig. 4.2.a). The range analysis is made using a combination of a thin stopper and an energy degrader, the thickness of which can be controlled (see Fig. 4.2.b). In this method, only the desired nuclei can be selectively implanted in a thin stopper, by adjusting the thickness of the absorber.

A view of entire Beam line 44 is shown in Fig. 4.3. This beam line has five foci, and the total length is about 55 m. F1 and F3 are achromatic foci, and F2 and F4 are momentum-dispersive foci. We placed a target at F3 and used the down-stream section of the beam line as a fragment separator. The rigidity was selected at F4, and the energy-loss analysis was performed by an energy degrader placed at F4 and a dipole magnet located down stream. F5 is the final focus, where the NMR-magnet and a stopper are located. Another energy degrader, the thickness of which is controllable, is placed right before F5 in order to control the range of fragments and to implant the desired fragment in a catcher. A schematic view of this setup is shown in Fig. 4.4. Since the F5 focus was not a perfect achromatic focus without using a degrader at F4, the dispersion at F5 was planned to be eliminated by careful designing the degrader used at F4.

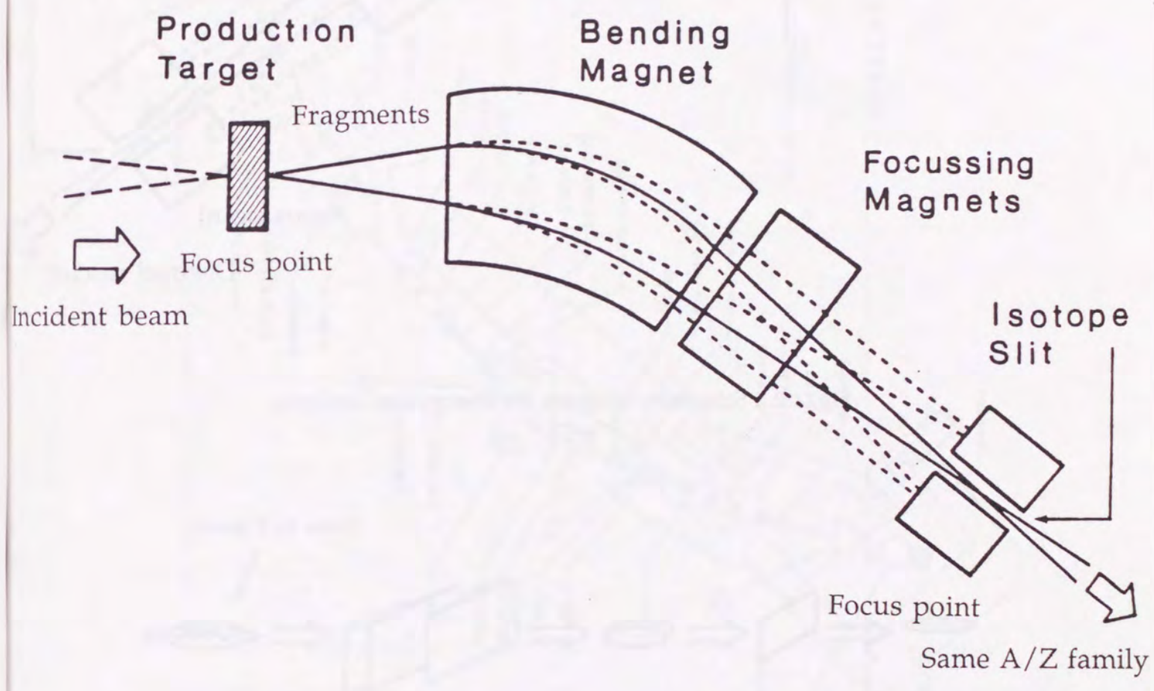

Fig. 4.1 Schematic diagram for rigidity analysis.

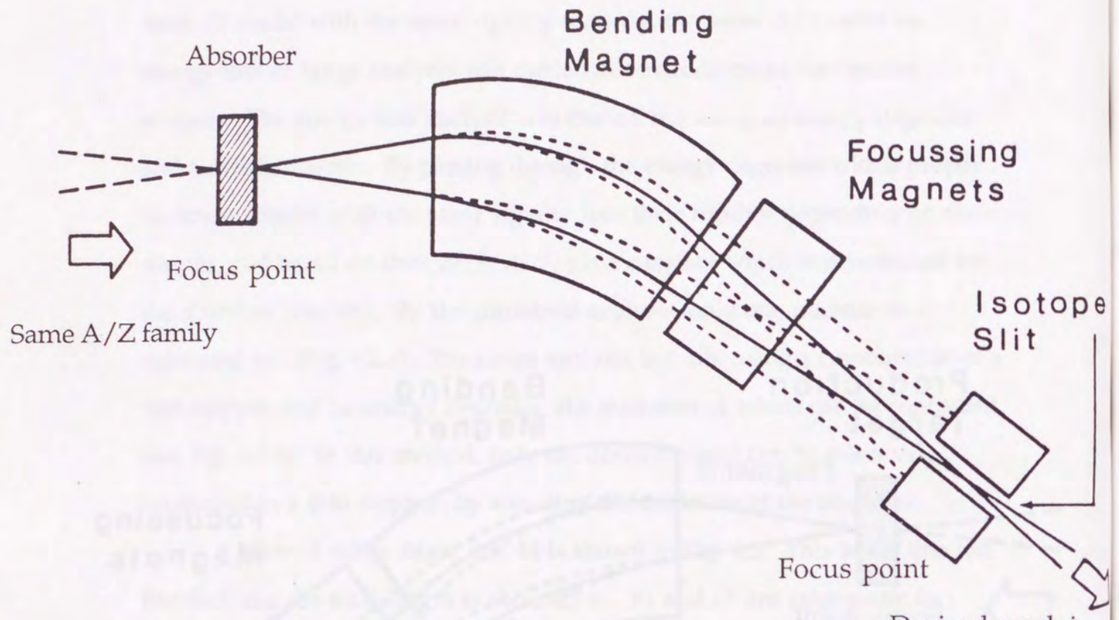

Fig. 4.2.a Schematic diagram for energy-loss analysis.

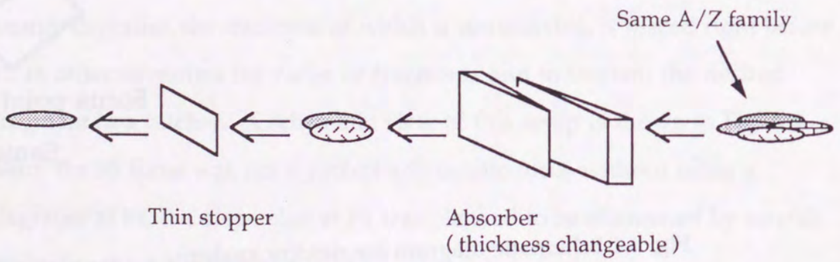

Fig. 4.2.b Schematic diagram for range analysis.

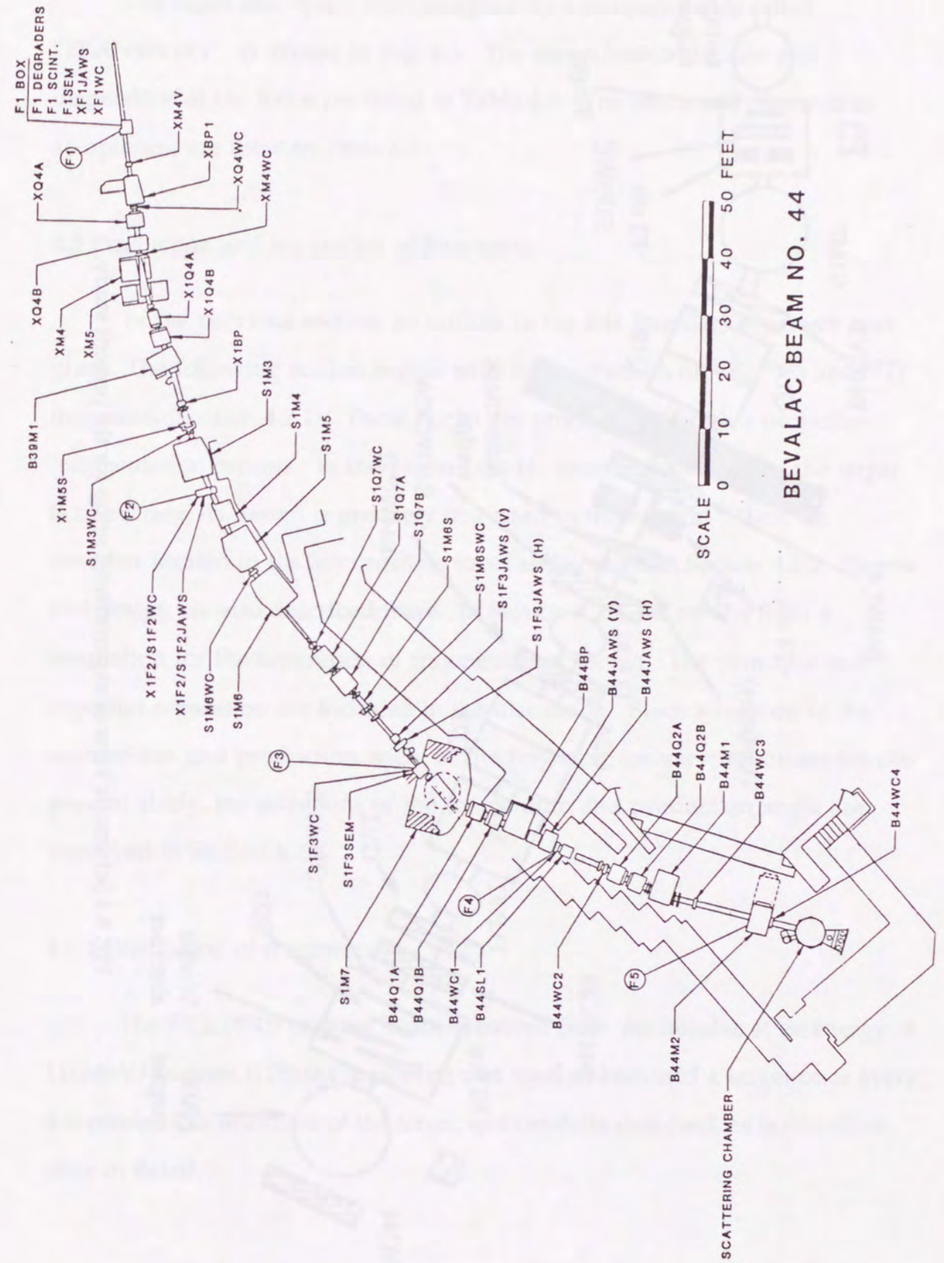

Fig. 4.3 Beam line 44 at the Bevalac.

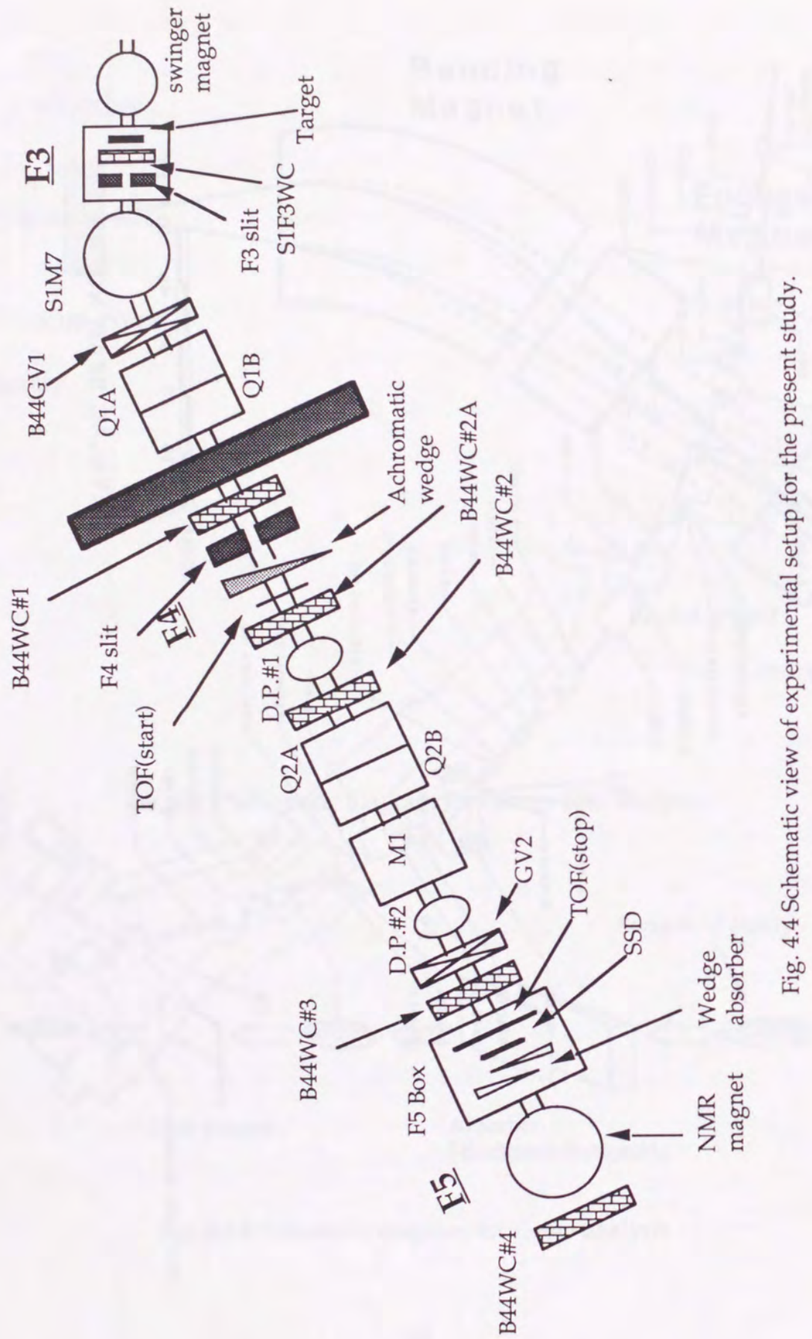

Fig. 4.4 Schematic view of experimental setup for the present study.

The beam-line optics were designed by a computer code called "TRANSPORT", as shown in Fig. 4.5. The magnification factors and dispersions at the focus are listed in Table 4.1. The beam and momentum acceptances are listed in Table 4.2.

4.2 Production and separation of fragments

In the previous section, an outline of the B44 fragment separator was given. The following section begins with the production of ^{37}K, ^{39}Ca and ^{43}Ti fragments (Section 4.2.1). These nuclei are produced through a projectile-fragmentation process. In the present study, since the thickness of the target is important, its design is precisely discussed in this section. Then, an absorber located in the intermediate focus is discussed in Section 4.2.2. Its role and design are also described there. In Section 4.2.3, the results from a simulation for the separation of fragments are shown. The principle and expected separation are included in the discussion. Since selections of the momentum and production angle of the fragment are very important for the present study, the selections of the momentum and production angle are described in Section 4.2.4.

4.2.1 Production of fragments

The ^{40}Ca (^{46}Ti) primary beam extracted from the Bevalac at an energy of 119MeV/nucleon (125MeV/nucleon) was used to bombard a target once every 4 seconds. The thickness of the target was carefully designed, as is described later in detail.

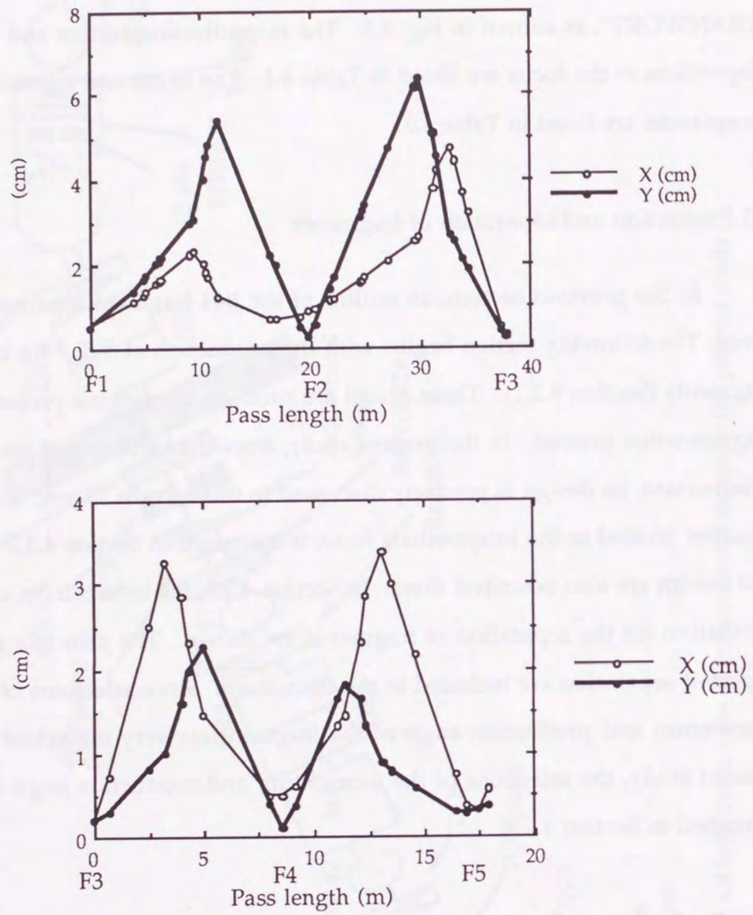

Fig. 4.5 Horizontal (X) and vertical (Y) beam-envelopes of B44.

Position	Distance (m)	Magnification X	Y	Dispersion (cm/%)
F1 ⇒ F3	38.10	+0.449	+0.629	-0.175
F3 ⇒ F4	8.634	-2.454	+0.509	+1.740
F4 ⇒ F5	8.824	-0.625	+3.12	+0.583

Table 4.1 First-order optical parameters.

Configuration	D-Q-Q (first stage)
	Q-Q-D (second stage)
Angular acceptance	14 mr x 14 mr
Momentum acceptance	1.9 % (max)
Max. magnetic rigidity	7.5 Tm
Foci	F3, production target position
	F4, momentum dispersive, end of first stage
	F5, (achromatic), end of second stage
Isotopic separation	A/Z and energy loss
Beam swinger	max. 3 deg

Table 4.2 Basic characteristics of Beam line 44.

The average beam-intensity was about 2×10^9 (3×10^8) particles per beam spill for the ^{40}Ca (^{46}Ti) beam. (The internal beam-intensity in the accelerator was about 4-times larger than the extracted beam-intensity, and the typical extraction efficiency was 25%.)

The difference in the energy-loss in the target between the primary beam and projectile fragments causes a broadening of the fragment

momentum. Thus, in some other cases there should be an optimum thickness determined by momentum acceptance of the fragment separator (DU86). However, in the present case, the limitation of the target thickness results from a stricter consideration. Since the width of the momentum distribution due to the Fermi motion which reflects the reaction mechanism is Δp_{PF}, the ratio r_{PF} shown in the following equation gives the rigidity width:

$$r_{PF} = \frac{\Delta p_{PF}}{p_c} = 2\sqrt{2\ln 2}\ \frac{\sigma_{PF}}{p_c}\ , \qquad (4.1)$$

where p_c denotes the total momentum of the fragments and σ_{PF} is the width given by the Goldhaber model. For the momentum width due to the difference in the energy-loss in the target, the same ratio is given by

$$r_T = \frac{\Delta p_t}{p_c} \sim \frac{1}{2}\frac{\Delta E_t}{E_c}\ , \qquad (4.2)$$

where ΔE_t and E_c denote the difference in the energy-loss and the energy of the fragments. Since the nuclear polarization is smeared out if r_T is larger than r_{PF}, the condition for the target thickness becomes

$$r_T < r_{PF}\ . \qquad (4.3)$$

In order to fulfill this condition, the thickness of an Au target was determined to be 380 μm (250 μm) for a ^{40}Ca (^{46}Ti) beam. Similarly, a C target for the ^{46}Ti beam was 260 mg/cm^2 thick.

The production rates of the various fragments were estimated as shown in Fig. 4.6 using the computer code "FRAGBNL" for the condition. From these figures, the predicted production rate of ^{43}Ti (^{39}Ca) was found to be about 1000 particles/spill (5000 particles/spill) for an Au target with a primary-beam intensity of 1×10^8 particle/spill.

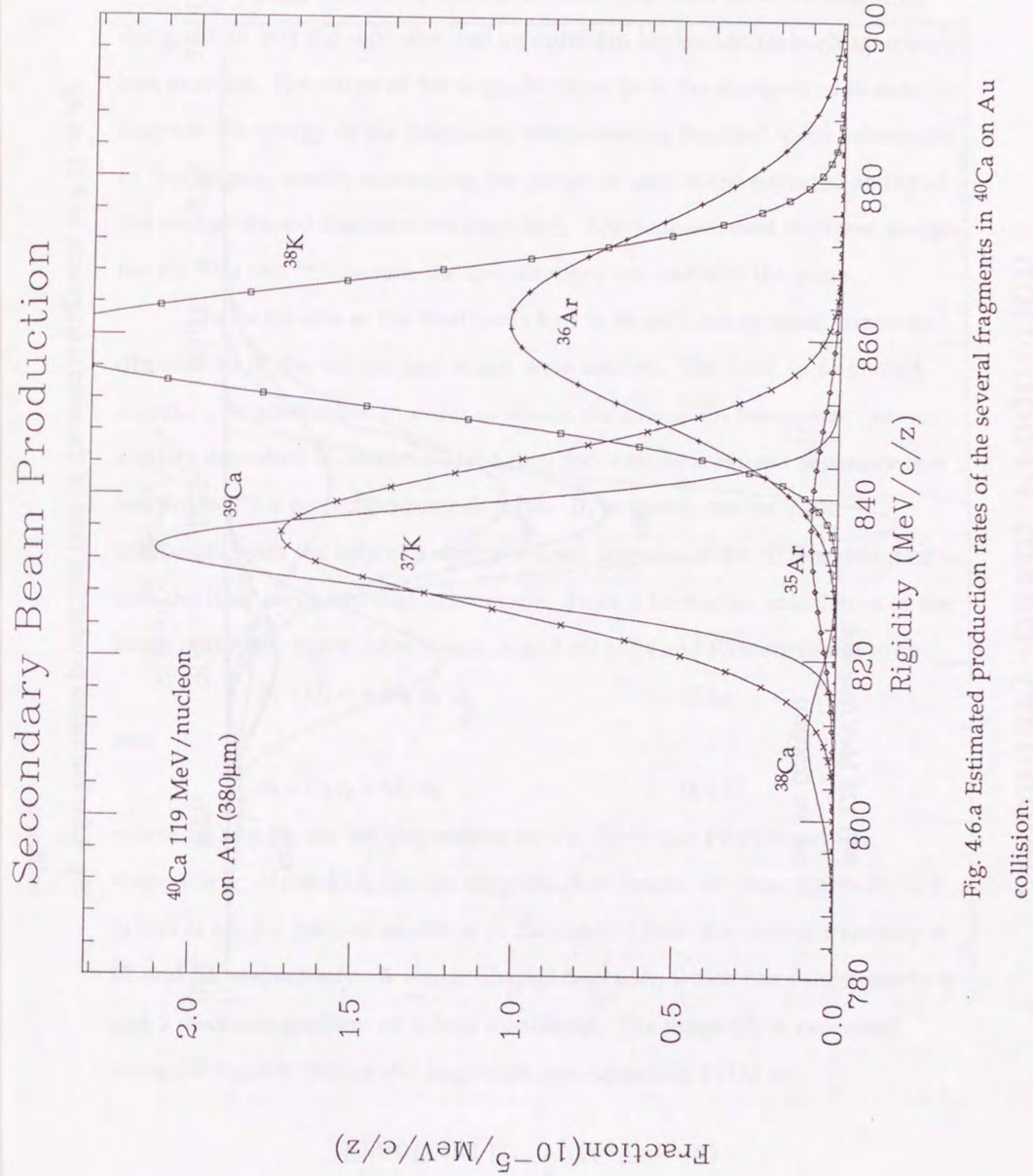

Fig. 4.6.a Estimated production rates of the several fragments in ^{40}Ca on Au collision.

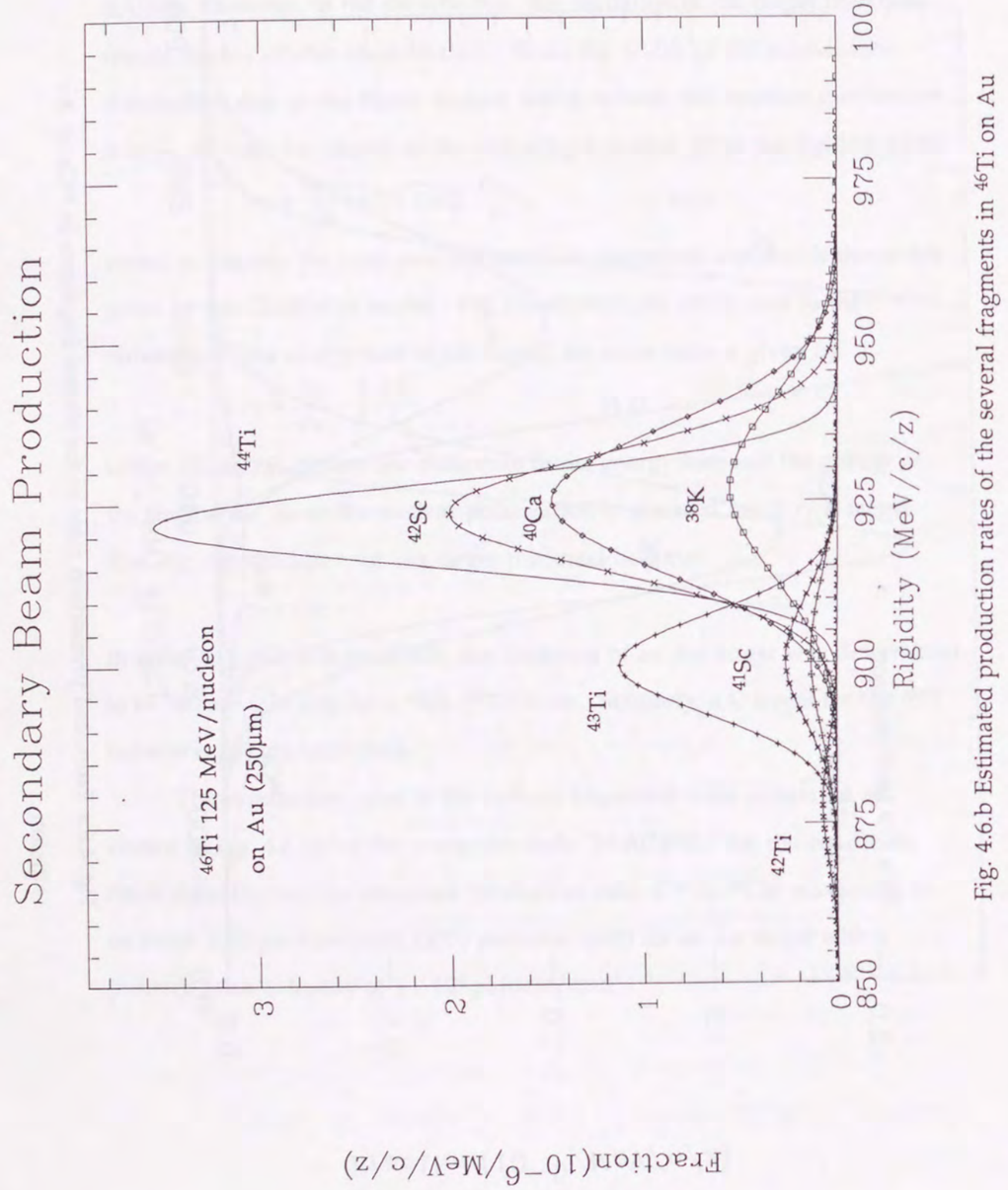

Fig. 4.6.b Estimated production rates of the several fragments in ^{46}Ti on Au collision.

4.2.2 Achromatic wedge in the separation

The energy-absorber placed at the first dispersive focus F4 should be designed so that the separator has an optimum separation through an energy-loss analysis. The shape of the degrader must be of the wedge type in order to degrade the energy of the fragments while keeping the final focus achromatic. In this section, details concerning the design as well as the expected ability of the wedge-shaped degrader are described. Although we used different wedges for the ^{40}Ca and ^{46}Ti beams, the specifications are basically the same.

The beam size at the final focus had to be sufficiently small, since the dimensions of the catcher and rf coil were limited. The final focus should therefore be achromatic in order to obtain the minimum beam size. As already described in Section 4.1, the final focus of the fragment separator was not originally a perfect achromatic focus. It, however, can be made achromatic with the help of a wedge-shaped degrader at F4. It was designed so that the final focus becomes achromatic. From a first-order calculation of the beam optics, the beam sizes (x-axis σ_4 and σ_5) at F4 and F5 were found to be

$$\sigma_4 = D_4 r_3 + M_4 \sigma_3 \qquad (4.4.a)$$

and

$$\sigma_5 = D_5 r_4 + M_5 \sigma_4 \quad , \qquad (4.4.b)$$

where D_4 and D_5 are the dispersions for the F3-F4 and F4-F5 intervals, respectively; M_4 and M_5 are the magnification factors for these intervals; and r_3 and r_4 are the percent deviation of the rigidity from the central trajectory at F3 and F4, respectively. A wedge-shaped degrader, which has a thickness of t_c and a thickness gradient of η, was considered. The range (R) is expressed using the rigidity ($B\rho$) of the fragments (see Appendix 1-(1).) as

$$R = k \frac{Z^{2\gamma+2}}{A^{2\gamma+1}} B\rho^{2\gamma} , \qquad (4.5)$$

where the parameter γ is close to 1.75 in the energy region and k is a constant. The momentum width of the fragment after the wedge degrader at F4 is thus given by

$$r_4 = \left(\frac{B\rho_3}{B\rho_4} \right)^{3.5} r_3 - \frac{\eta}{3.5\,k} \frac{A^{2.5}}{Z^{1.5}} \frac{1}{B\rho_4{}^{3.5}} \sigma_4 , \qquad (4.6)$$

where $B\rho_3$ and $B\rho_4$ are the rigidities at F3 and F4. We put Equation (4.6) into Equation (4.4) and obtained following relation:

$$\sigma_5 = \left\{ \left(\frac{B\rho_3}{B\rho_4} \right)^{3.5} D_5 - \frac{\eta}{3.5\,k} \frac{A^{2.5}}{Z^{1.5}} \frac{1}{B\rho_4{}^{3.5}} D_5\ D_4 + M_5\ D_4 \right\} r_3 + \left\{ M_5 - \frac{\eta}{3.5\,k} \frac{A^{2.5}}{Z^{1.5}} \frac{1}{B\rho_4{}^{3.5}} D_5 \right\} M_4\ \sigma_3 . \qquad (4.7)$$

The achromatic condition requires the first term to be zero:

$$\left(\frac{B\rho_3}{B\rho_4} \right)^{3.5} D_5 - \frac{\eta}{3.5\,k} \frac{A^{2.5}}{Z^{1.5}} \frac{1}{B\rho_4{}^{3.5}} D_5\ D_4 + M_5\ D_4 = 0 . \qquad (4.8)$$

From this condition, the thickness gradient (η) is given as

$$\eta = 3.5\,k \frac{Z^{1.5}}{A^{2.5}} B\rho_4{}^{3.5} \left\{ \left(\frac{B\rho_3}{B\rho_4} \right)^{3.5} \frac{1}{D_4} + \frac{M_5}{D_5} \right\} . \qquad (4.9)$$

When this condition is fulfilled, the beam size at F5 is determined by the second term in Equation (4.7), as

$$\sigma_5 = - \frac{D_5}{D_4} \left(\frac{B\rho_3}{B\rho_4} \right)^{3.5} M_4\ \sigma_3 . \qquad (4.10)$$

The beam-line parameters of B44 are listed in Table 4.1. The original rigidity ($B\rho_3$) just after the target is determined at Section 4.2.1. It turns out that the smaller is the rigidity ($B\rho_4$) after the degrader, the smaller is the beam size at F5. However, we must also consider the separation power of the separator regarding the design. When different isotopes pass through the absorber, the energy-loss was different, as was the deviation of the rigidity at F4 (r_4). From Equation (4.4.b), the focus position (X_5) at F5 for different isotopes is given by

$$X_5 = D_5\, r_4 . \qquad (4.11)$$

From this equation, it can be seen that the larger is the deviation of the rigidity, the better is the separability at F5. This means that the thicker is the degrader, the better is the separability. Using Equations (4.6) and (4.9), the focus position (X_5) is given as

$$X_5 = \frac{D_5}{3.5\,k\,r_3} \varepsilon , \qquad \varepsilon = \frac{1.5}{Z} dz - \frac{2.5}{A} dA . \qquad (4.12)$$

It is now clear that we can obtain the optimum thickness of the degrader to achieve both good focusing and separability. In the actual design, due to a limitation in the rf-coil size, the width of the F5 slit was determined to be ± 8 mm. The degrader was made of Acryl ($C_5H_8O_2$) plate because of the ease in machining, as well as the light constituting element.

The thickness and gradient of the wedge-shaped degrader for ^{43}Ti was designed to be t_c = 0.393 cm and η = 0.441%, according to the above discussion. The beam size of ^{43}Ti at the final focus was expected to σ_5 = 1.1 cm. These parameters were t_c = 0.25 cm, η = 0.0%, and σ_5 = 0.6 cm in the case of ^{39}Ca.

The actual wedge-shaped degrader for ^{43}Ti experiment is shown in Fig. 4.7. The homogeneity in the thickness was as good as ± 0.5%.

4.2.3 Mass separation

The rigidity analysis is carried out using a dipole magnet (S1M7) located between F3 and F4, and a slit at F4. The rigidity for nuclei having an atomic number (Z) and mass number (A) is given by

$$B\rho = 0.1439 \frac{A}{Z} \sqrt{E_n} \sqrt{1 + \frac{E_n}{2m_u}} , \qquad (4.13)$$

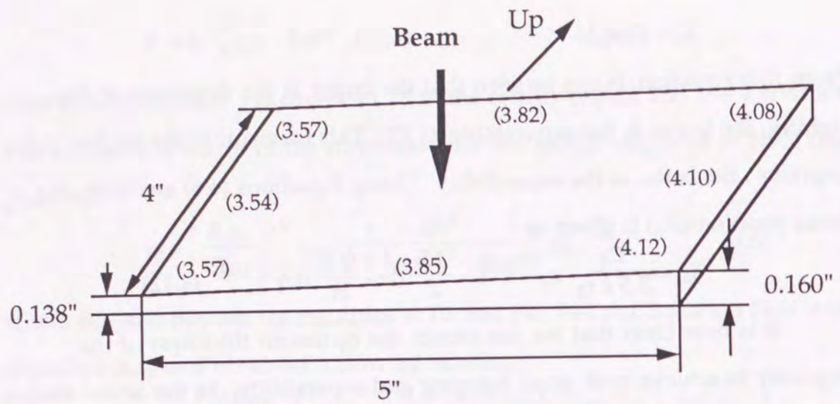

( ) : measured thickness (unit : mm)

Fig. 4.7 Achromatic wedge degrader used for ^{43}Ti experiment.

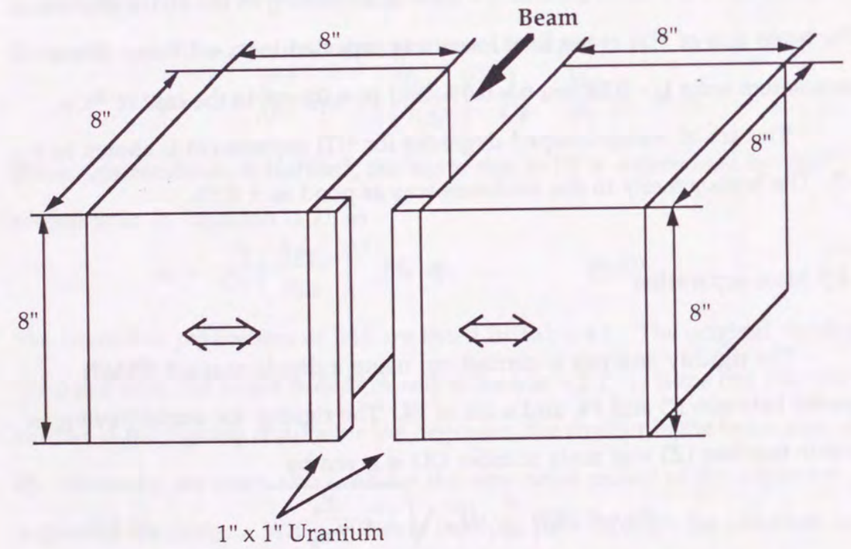

Fig. 4.8 F4 momentum selecting slit-jaws.

where E_n is expressed in MeV per nucleon and m_u is the atomic mass unit (DU86). The E_n of each fragment is almost constant, since their velocities are very close to that of the primary beam. By the rigidity analysis, fragments are separated based on the mass-over charge ratio (A/Z). The maximum rigidity of S1M7 is 7.2 Tm. Simulated rigidity distributions of each fragments ejected from an Au target are shown in Fig. 4.6 for the cases of the ^{46}Ti and ^{40}Ca beams. A schematic view of the slit located at F4 is shown in Fig. 4.8.

There are two ways to carry out a range analysis, as discussed in the former section. In one of them, using an achromatic wedge, a proper separation can be obtained at the final focus. The results from a simulation of the separation of mirror nuclei are shown in Fig. 4.9. From the simulated results, the opening of the F5 aperture was designed to be ± 8 mm (Fig. 4.10).

Another method involves a direct range analysis which combines a thin catcher and an energy degrader, the thickness of which is controllable. The energy degrader essentially comprises double-wedge-shaped plastic-plates, as given in Fig. 4.11. Simulated range distributions are shown in Fig. 4.12. Since the range of the particle is proportional to the ratio ($Z^{2\gamma-2}/A^{2\gamma-1}$) for a given rigidity, and the parameter γ is very close to 1.75 in the present energy region (DU86), the fragments are separated based on the ratio $Z^{1.5}/A^{2.5}$.

4.2.4 Momentum and angular selection

In the present work, selections of the momentum and the production angle of fragments were essential. However, it was not easy to swing the entire fragment separator for a finite production angle. The primary beam was therefore swung so as to introduce the production angle using two dipole magnets, as is shown in Fig. 4.13.a. The first magnet swung the beam off the

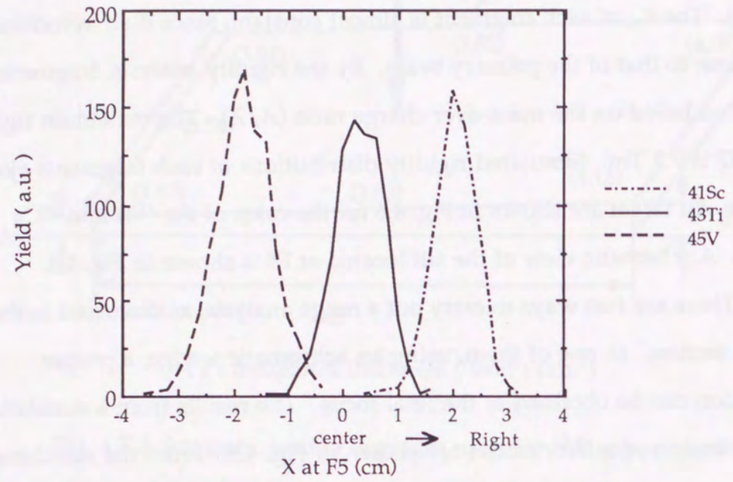

Fig. 4.9 Spatial distribution of the several fragments at the final focus (F5) predicted by the Monte Carlo simulations.

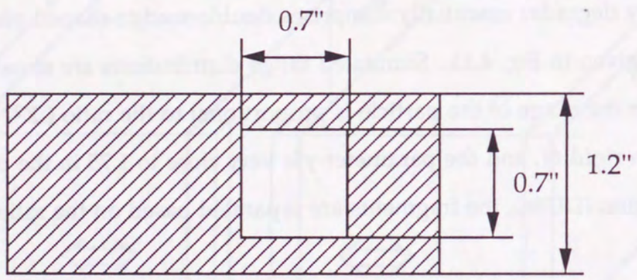

Material : Cu

Thickness : 1/8"

Fig. 4.10 F5 aperture.

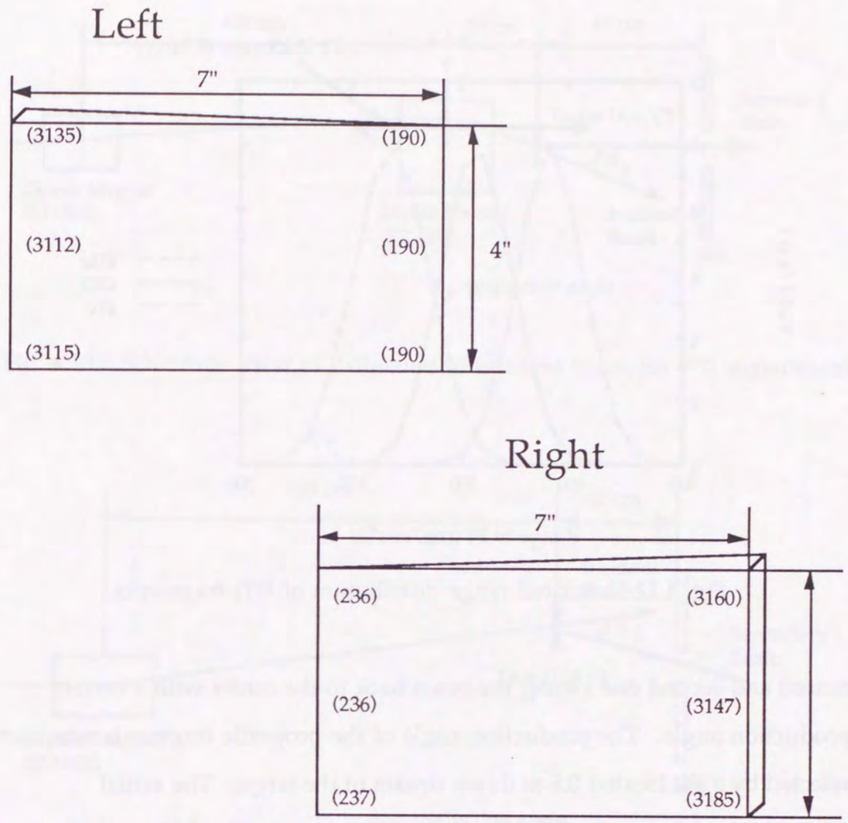

( ) : measured thickness (unit : μm)

Fig. 4.11 F5 degraders for range adjustment.

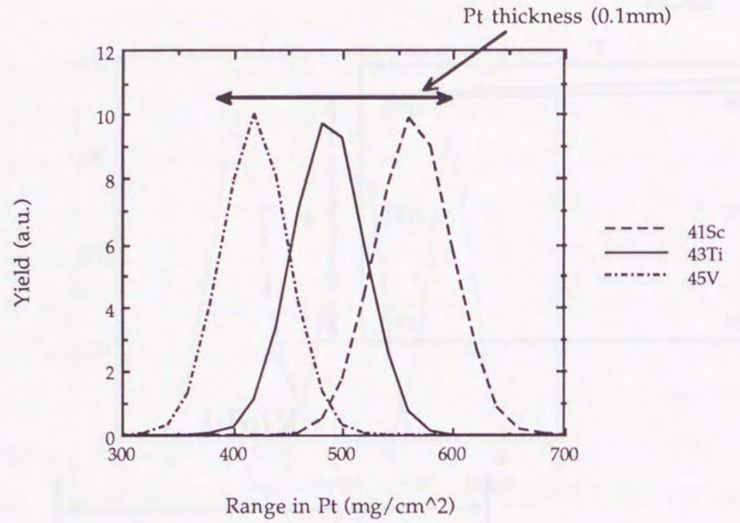

Fig. 4.12 Simulated range distribution of ^{43}Ti fragments.

center; and second one swung the beam back to the center with a certain production angle. The production angle of the projectile fragments was then selected by a slit located 0.6 m down stream of the target. The actual dimensions of the angle-defining slit-jaw are given in Fig. 4.14.

In the case of a ^{40}Ca beam, only one dipole magnet (S1M6S) was used for the same purpose, as is shown in Fig. 4.13.b. The difference, however, is not essential for the present study.

The momentum of the fragments was selected by the dipole magnet (S1M7) and the slit located at F4.

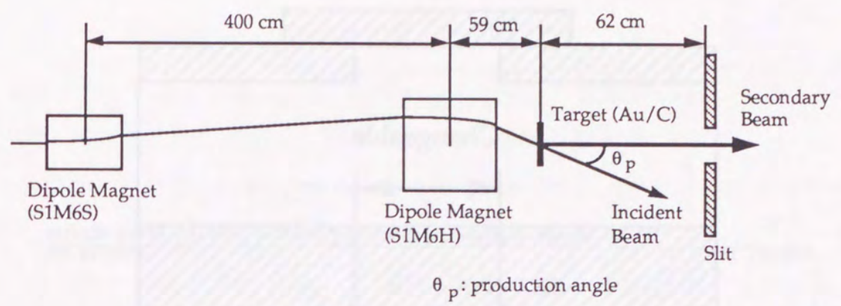

Fig. 4.13.a Schematic view of deflection of incident beam for ^{43}Ti experiment.

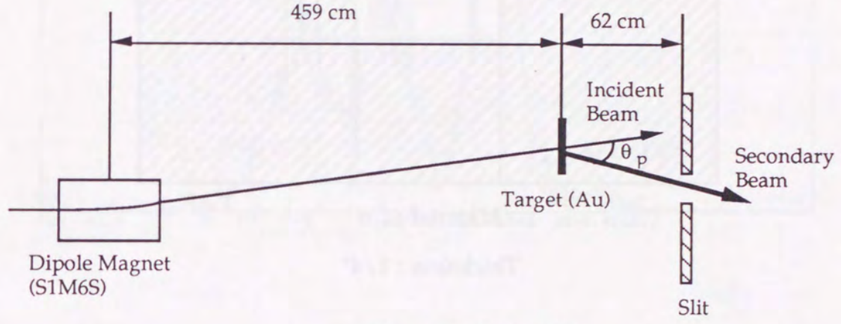

Fig. 4.13.b Schematic view of deflection of incident beam for ^{37}K and ^{39}Ca experiment.

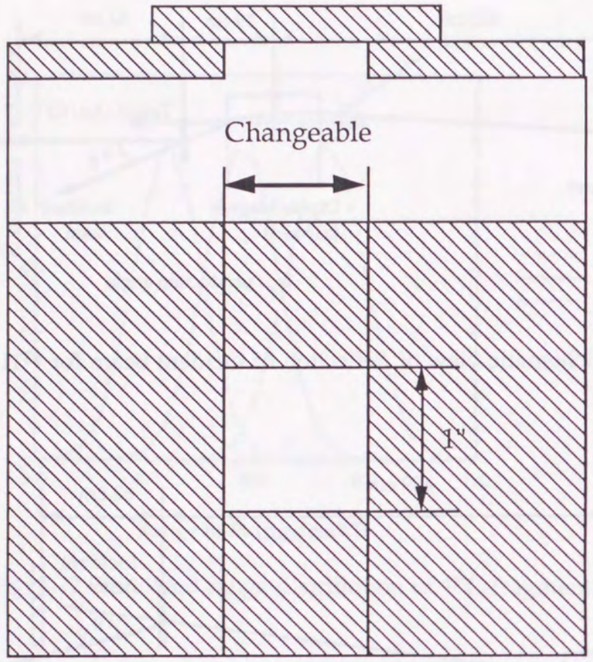

Material : Cu

Thickness : 1/4"

Fig. 4.14 F3 angle-defining slit.

4.2.5 Example of separated fragments

In this section the separation of fragments by fragment separator B44 is shown. Especially, the ^{43}Ti experiment is described as an example.

The results from a rigidity analysis are shown in Fig. 4.15. In this figure we see some contaminants, with A/Z=2.00 in the dominant fragments with A/Z=1.95.

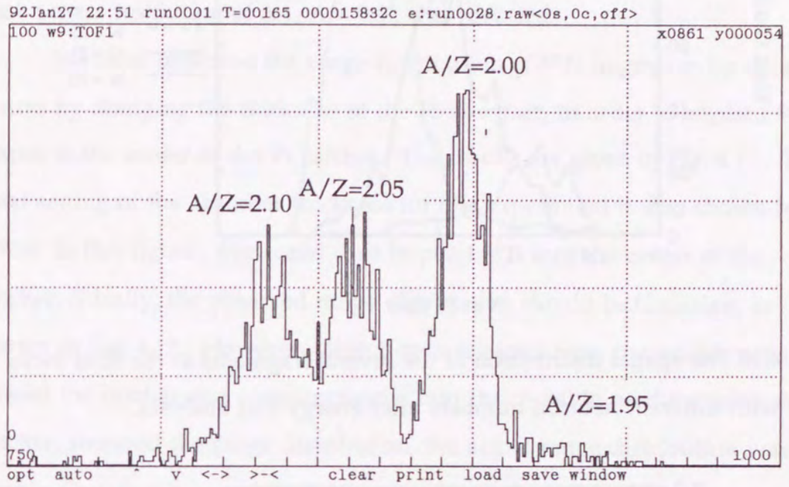

Fig. 4.15 TOF spectrum of fragments after rigidity analysis.

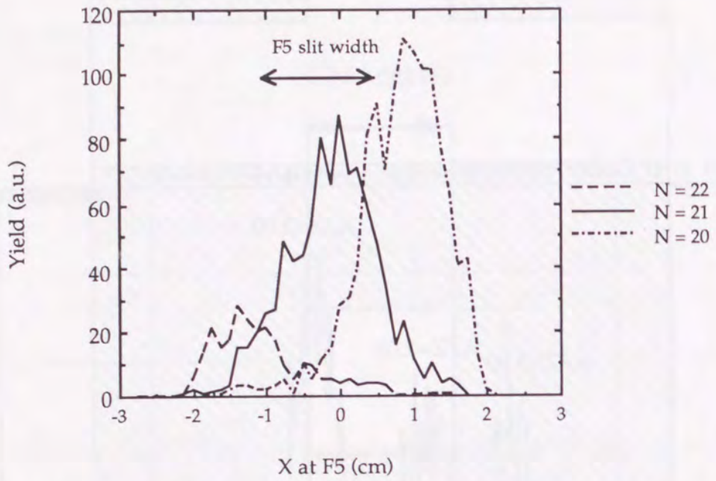

Fig. 4.16 The spatial distribution of the several fragments at the final focus (F5) with different neutron numbers after energy-loss analysis.

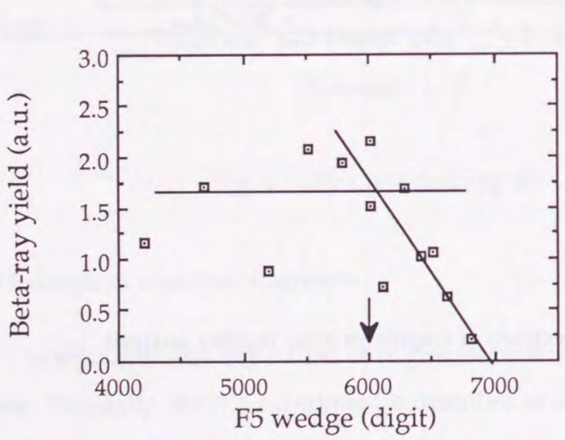

Fig. 4.17 Range distribution of the ^{43}Ti fragment.
Solid lines are to guide the eye. Arrow denotes the setting of the F5 wedge in the present study.

The results of the energy-loss analysis are shown in Fig. 4.16. The figure shows the position X distribution of each fragments at the final focus (F5). Comparing the result with the simulation shown in Fig. 4.9, we conclude that the separation power was quite consistent with the design and that a mass resolution of $\Delta A/A = 0.02$ was revealed.

We have observed the range distribution of ^{43}Ti fragments by detecting β-rays by changing the thickness of the F5 absorber, in order to implant ^{43}Ti nuclei in the center of the Pt catcher. The results are given in Fig. 4.17. The final setting of the absorber thickness for this experiment is also shown by the arrow in this figure. We could thus implant ^{43}Ti into the center of the catcher. (Ideally, the observed range distribution should be Gaussian, as shown in Fig. 4.12. However, since β-rays released from the nuclei, which passed the catcher and were implanted into the rf-coil located just after the catcher, smeared the range distribution, the actual range distribution was not simple Gaussian.)

In order to identify ^{43}Ti, we performed measurements of the time spectrum of β-rays. A typical time spectrum is shown in Fig. 4.18. This spectrum was analyzed by a χ^2-fitting analysis using the following function, which comprises two decay components and a constant back ground:

$$N = A_1 \exp\left(-\frac{\ln 2}{509}t\right) + A_2 \exp\left(-\frac{\ln 2}{680}t\right) + A_3 , \qquad (4.14)$$

where A_1, A_2 and A_3 are fitting parameters; 509 and 680 are the half-lives of ^{43}Ti and ^{42}Sc, respectively. The fitting results are shown in the figure, where the solid, the dotted and the dashed lines denote the components of ^{43}Ti, ^{42}Sc and constant-background, respectively. χ^2 was 0.90 in the analysis. From this analysis ^{43}Ti was identified. However, it is noted that ^{42}Sc, which is an isotone of ^{43}Ti, was observed at the same time, though ^{42}Sc ideally could be

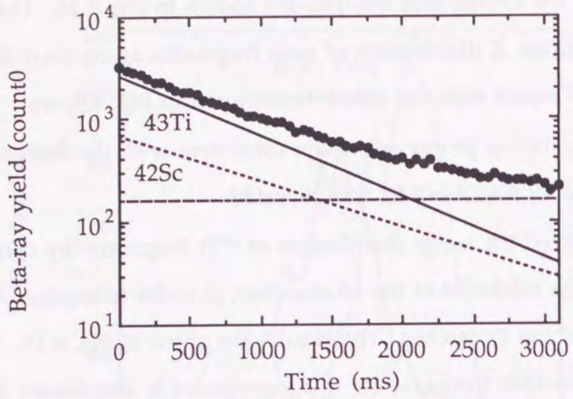

Fig. 4.18 Typical β-ray time spectrum of the ^{43}Ti fragment.
A solid line denotes the component of ^{43}Ti. A dotted line and a dashed line denote the components of ^{42}Sc and constant back-ground, respectively.

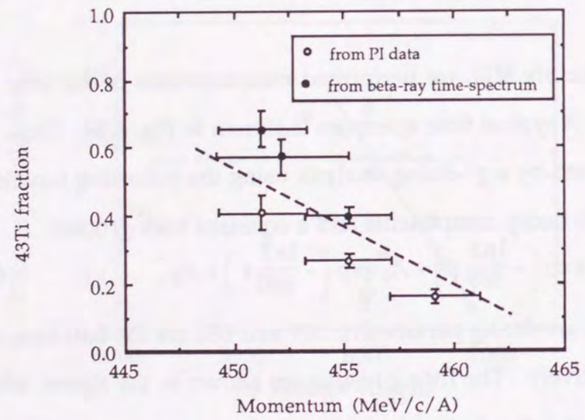

Fig. 4.19 Fraction of ^{43}Ti in the total particle yield as a function of fragment momentum. A dashed line is to guide the eye.

separated by a rigidity analysis. (Since the production cross-section of ^{42}Sc is larger than that of ^{43}Ti, as shown in Fig. 4.6.b, a part of ^{42}Sc, which could not be separated by the rigidity analysis, can be observed at the final focus (F5).)

Thus, the ^{43}Ti fraction is necessary in order to precisely evaluate the amount of the polarization. By integrating Equation (4.14) for each components we can estimate the ^{43}Ti fraction. Several time spectra were measured for different momentum windows. The obtained fractions for the momentum windows are shown in Fig. 4.19. We can also evaluate the ^{43}Ti fraction from the results of particle identification. We identified the nuclei which passed into F5, and also counted the number of the nuclei. The results are also shown in Fig. 4.19. They are consistent with each other. Although the ^{43}Ti fraction was small (~0.2) on the high-momentum side, it was large (~0.5) on the low-momentum side. This tendency is consistent with the prediction given in Fig. 4.6; the ^{43}Ti fraction, however, is less than the predicted value.

4.3 Particle identification

Tuning the fragment separator to the desired projectile fragments is very important. We had to tune the separator for the optimum separation, not just for delivering the beam to the final focus. In this process, the identification of fragments is crucial. In order to identify projectile fragments, the energy-loss ($-dE/dx$) and time-of-flight (TOF) were measured. In this section, the principle of particle identification (Section 4.3.1), detectors for identification (Section 4.3.2) and circuits and control system (Section 4.3.3) are described.

4.3.1 Principle of particle identification

Particle identification is completed when the mass (A), atomic number (Z) and velocity (v) of passing nuclei are determined. The charge state can also be important in some cases, but is not considered here since passing nuclei are fully stripped in the present energy region (~100 MeV/nucleon) (See Appendix 1-(3).). In order to determine these parameters, we measured the TOF, energy-loss and rigidity of passing nuclei. (Here, the equations are treated non-relativistically because of the present energy region.)

(i) TOF measurements of passing nuclei

The velocity is given by

$$v = \ell / \tau , \qquad (4.15)$$

where ℓ denotes the flight length and τ is the TOF.

(ii) Measurements of the energy-loss ($-dE/dx$)

The energy-loss in a material is roughly given by

$$-\frac{dE}{dx} \sim D\frac{Z_{med}\,\rho_{med}}{A_{med}}\left(\frac{Z}{v}\right)^2 , \qquad (4.16)$$

where "med" is a parameter of the host material (see Appendix 1-(1).).

(iii) Measurements of the rigidity ($B\rho$)

The rigidity is obtained from Equation (4.13), and is roughly given by

$$B\rho \sim k_2 \frac{A}{Z} v \text{ , where } k_2 = 0.1439. \qquad (4.17)$$

By combing these measurements, the mass, atomic number and velocity of passing nuclei can be determined. From Equations (4.15) and (4.16), the atomic number (Z) is given by

$$Z \sim c\sqrt{\left(-\frac{dE}{dx}\right)}\frac{\ell}{\tau} \text{, where } c = \sqrt{\frac{A_{med}}{D\,Z_{med}\,\rho_{med}}} . \qquad (4.18)$$

On the other hand, upon combining Equations (4.16) and (4.17), the mass (A) is given by

$$A \sim \frac{c}{k_2}(B\rho)\sqrt{\left(-\frac{dE}{dx}\right)} . \qquad (4.19)$$

Here, the resolution of particle identification is referred to. Since measurements in (i) - (iii) have some errors, we should consider them. The resolutions in the mass and atomic numbers are given by

$$\frac{\delta Z}{Z} \sim \sqrt{\left(\frac{\delta(-dE/dx)}{(-dE/dx)}\right)^2 + \left(\frac{\delta\tau}{\tau}\right)^2} \qquad (4.20.a)$$

and

$$\frac{\delta A}{A} \sim \sqrt{\left(\frac{\delta(-dE/dx)}{(-dE/dx)}\right)^2 + \left(\frac{\delta(B\rho)}{B\rho}\right)^2} . \qquad (4.20.b)$$

In the present study, the mass and atomic number of passing nuclei were about 40 and 20, respectively. Thus, in order to achieve particle identification, a resolution of 1% for the mass and 2% for the atomic number were necessary.

4.3.2 Detectors

For the particle identification described above, TOF counters were placed at F4 and F5, and a SSD counter at F5, as shown in Fig. 4.4. The TOF counters comprised two plastic-scintillation counters called a 'start' counter (F4), and a 'stop' counter (F5). These two scintillation counters are shown in Fig. 4.20. (The 'stop' counter was plungerable so that it could be removed from the beam line after it was tuned.) The flight length (the distance between the 'start' and 'stop' counters) was about 7.9 m.

TOF START COUNTER (unit : mm)

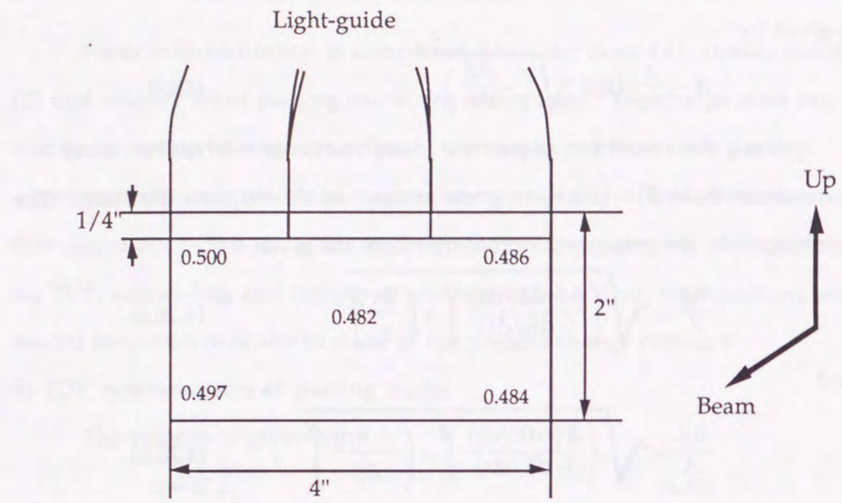

TOF STOP COUNTER (thickness : 0.50 mm)

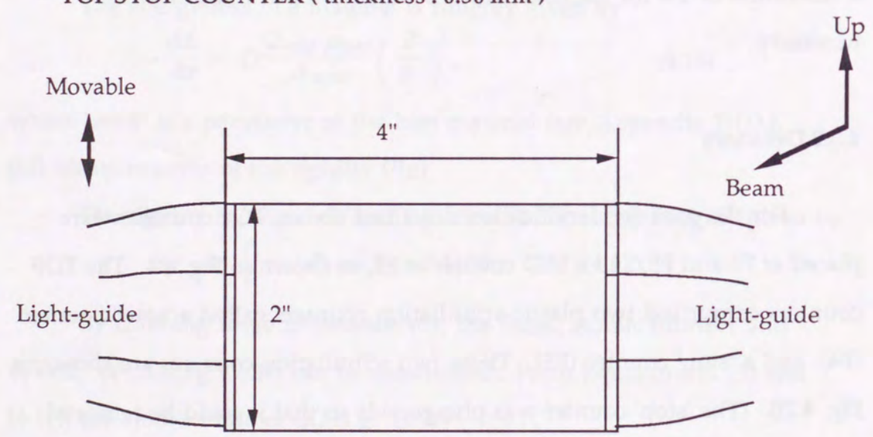

Fig. 4.20 TOF counters.

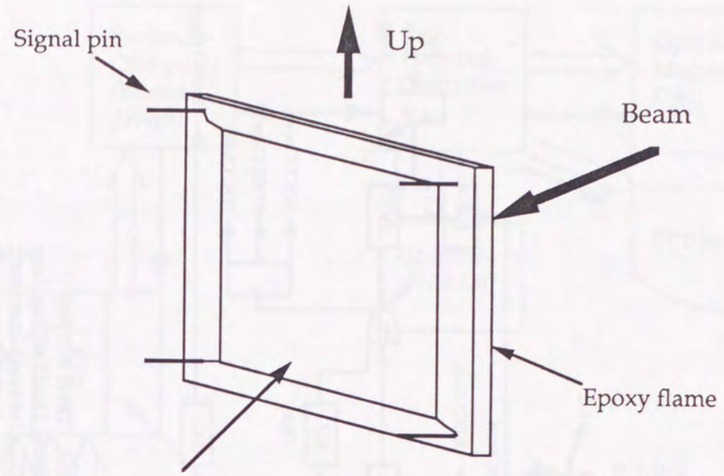

SSD ; Effective area : 45mm x 45mm
Thickness : 300 μm

Fig. 4.21 ΔE (SSD) counter.

The energy-loss of fragments was measured using a Si solid-state detector (SSD) located just after the TOF stop-counter at F5, as shown in Fig. 4.21. This SSD is sensitive to the position, so that it can be used to measure the beam size. The SSD is also plungerable.

4.3.3 Data-taking system for particle identification

A circuit diagram for particle identification is given in Fig. 4.22 and a block diagram of the data taking system is given in Fig. 4.23. Two personal computers (NEC's PC-9801) were used for the data accumulation. Digitized data converted in each CAMAC modules from the signals were read through the crate controller. The first computer was used to read the data, and then

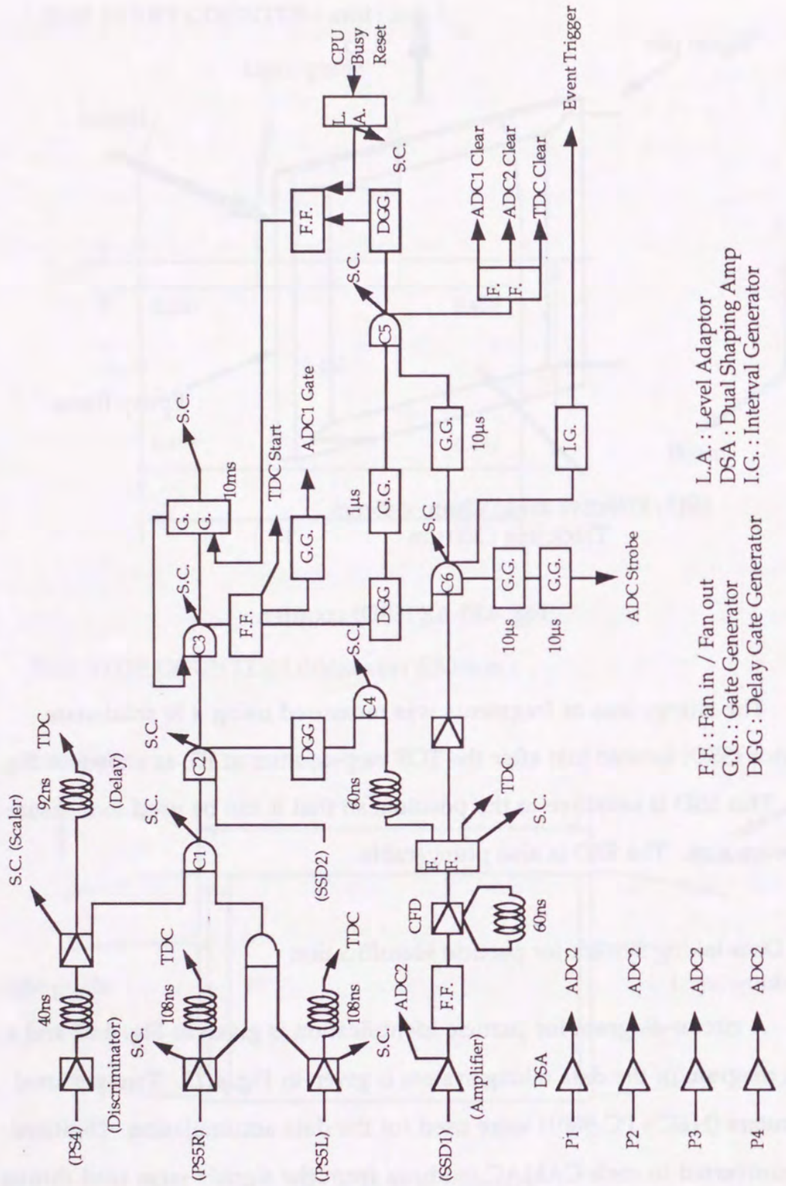

L.A. : Level Adaptor
DSA : Dual Shaping Amp
I.G. : Interval Generator
F.F. : Fan in / Fan out
G.G. : Gate Generator
DGG : Delay Gate Generator

Fig. 4.22 Electronics used in particle identification.

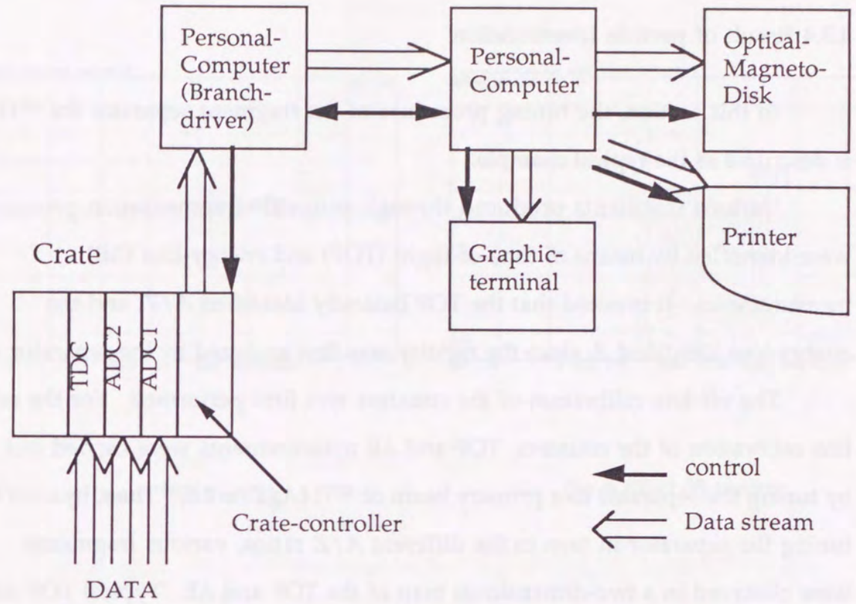

Fig. 4.23 Block diagram of the data-taking system for particle identification.

transfer it to the second computer. The second computer analyzed the data and stored them into a magneto optical disk.

The software used for the system was basically developed at INS (Kakuken-Online-Data-AcQuisition system KODAQ (OM91)). A flow chart is given in Appendix 5. The original version of the program was for only a few measurements, where only one PC and few CAMAC modules were used. For the present work, however, a revised version was developed for a faster response, in which two personal computers were used.

4.3.4 Result of particle identification

In this section, the tuning procedure of the fragment separator for ^{43}Ti is described as the typical example.

Various fragments produced through projectile-fragmentation process were identified by means of time-of-flight (TOF) and energy-loss (ΔE) measurements. It is noted that the TOF basically identified A/Z, and the energy-loss identified Z, since the rigidity was first analyzed by the separator.

The off-line calibration of the counters was first performed. For the on-line calibration of the counters, TOF and ΔE measurements were carried out by tuning the separator to a primary beam of ^{46}Ti (A/Z = 2.1). Then, by tuning the separator in turn to the different A/Z ratios, various fragments were observed in a two-dimensional map of the TOF and ΔE. Typical TOF-ΔE maps are shown in Fig. 4.24, where the F4 thin wedge was out of the beam path. Fig. 4.24.a shows a calibration using the primary beam; only ^{46}Ti can be seen in the figure. The field strength of all the separator magnets was then reduced by 2.5% in order to tune the separator to nuclei whose A/Z ratio is equal to 2.05. At that setting, ^{45}Ti and ^{43}Sc can be seen in the TOF-ΔE map, as shown in Fig. 4.24.b. In the next setting, nuclei with A/Z=2.00 appeared on the map (Fig. 4.24.c). In the final setting (A/Z=1.95) (7.5% lower magnetic field), ^{43}Ti was seen on the map (Fig. 4.24.d). Thus, identification of ^{43}Ti and tuning the separator to ^{43}Ti were completed. A similar procedure was also performed using the thin wedge at F4 for an energy-loss analysis. Typical TOF-ΔE maps under this condition are shown in Fig. 4.25.

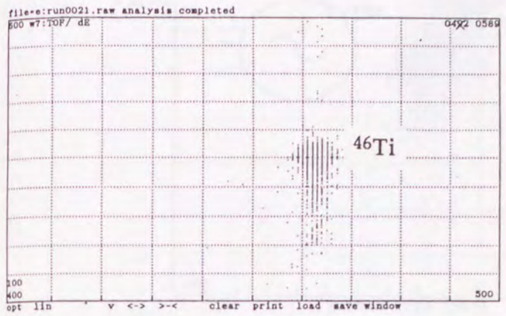

(a) Primary beam ^{46}Ti tuning.

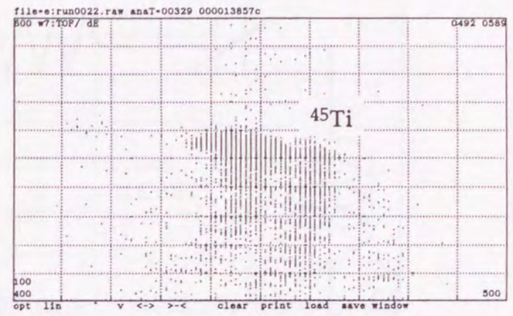

(b) A/Z=2.05 tuning.

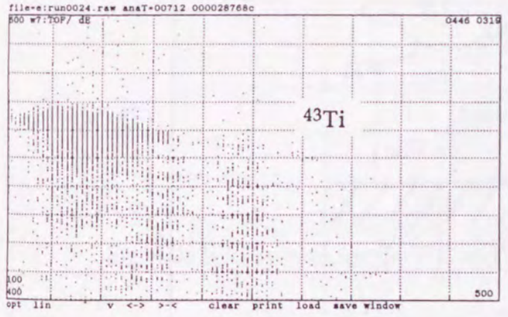

(d) A/Z=1.95 tuning.

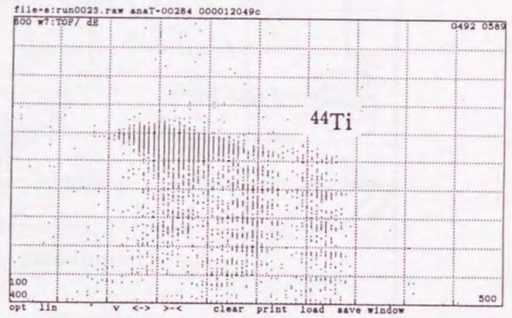

(c) A/Z=2.00 tuning.

Fig. 4.24 Typical TOF-ΔE maps of ^{43}Ti tuning without the F4 wedge degrader.

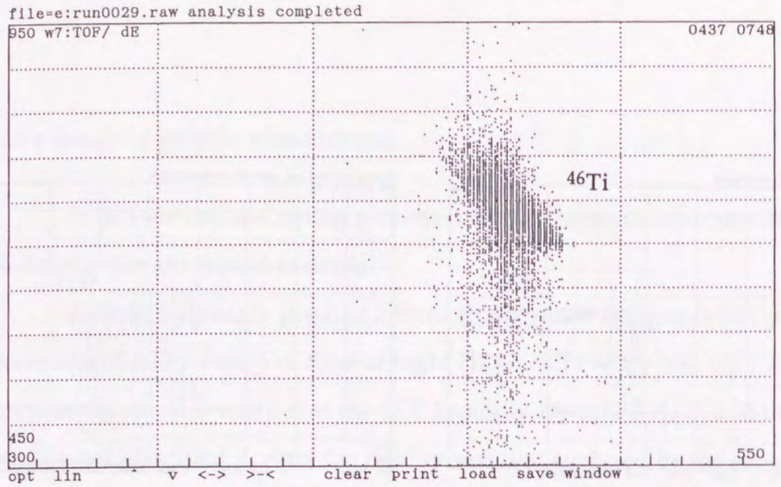

(a) Primary beam ^{46}Ti tuning.

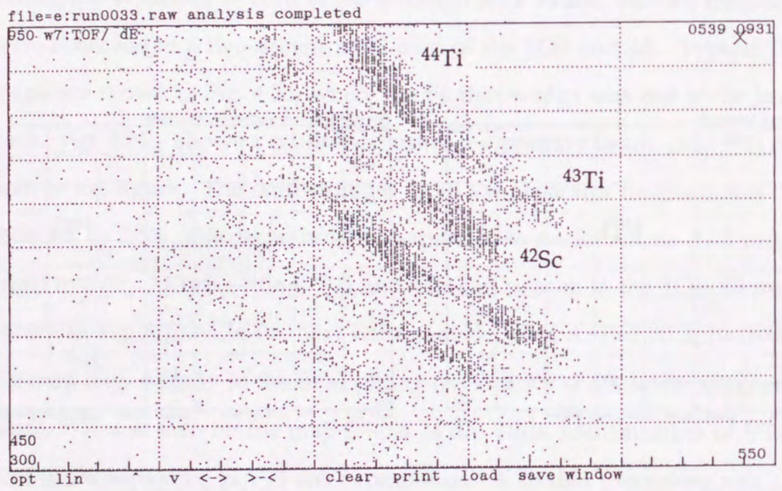

(b) A/Z=1.95 tuning.

Fig. 4.25 Typical TOF-ΔE maps of ^{43}Ti tuning with the F4 wedge degrader.

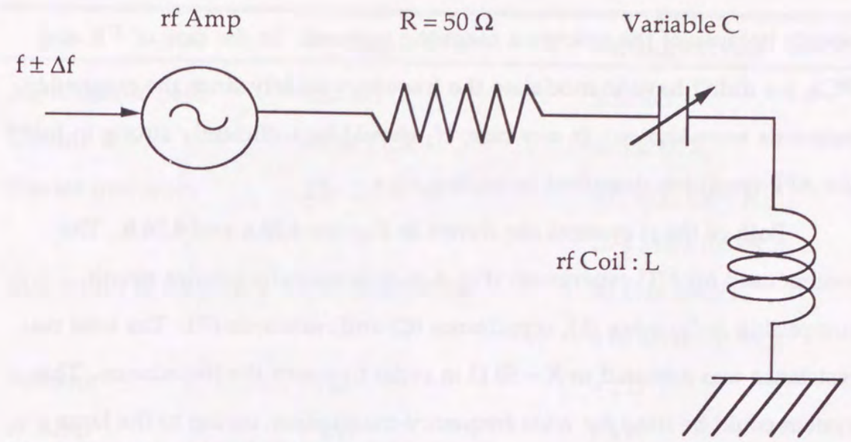

Fig. 4.26.a Rf system for the ^{43}Ti experiment.

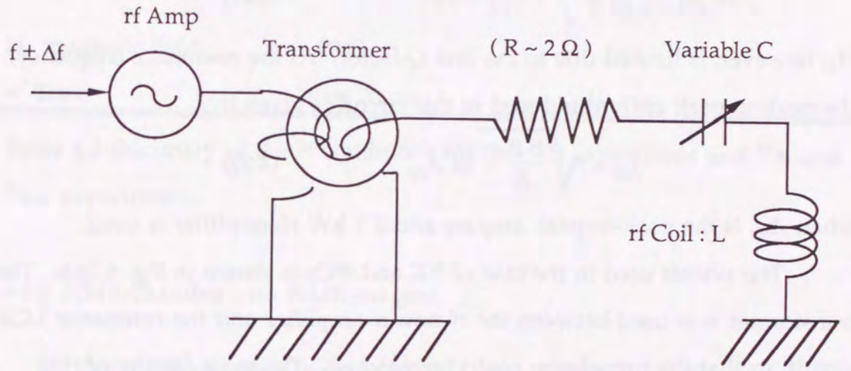

Fig. 4.26.b Rf system for the ^{37}K and ^{39}Ca experiment.

4.4 β-NMR apparatus

4.4.1 Rf system

This Rf system is one of the most important parts in the β-NMR technique. The system was slightly different between the ^{37}K and ^{39}Ca cases and the ^{43}Ti case. In the case of ^{43}Ti, it is important to modulate the frequency

widely because of the unknown magnetic moment. In the case of ^{37}K and ^{39}Ca, we didn't have to modulate the frequency widely since the magnetic moments were known. In any case, H_1 should be sufficiently strong to fulfill the AFP condition described in Section 3.1.4.

Both of the rf systems are shown in Figures 4.26.a and 4.26.b. The system used for ^{43}Ti experiment (Fig. 4.26.a) is basically a series circuit comprising inductance (L), capacitance (C) and resistance (R). The total real resistance was adjusted to $R = 50\ \Omega$ in order to match the impedance. This system could be used for wide frequency-modulation, owing to the large resistance (50 Ω),

$$\frac{1}{Q} = \frac{\Delta f}{f} = \frac{R}{2L} \sim 10^{-1}. \qquad (4.21)$$

H_1, however, is limited due to the low Q-factor. At the resonance frequency, the peak-to-peak current induced in this circuit is given by

$$I_{pp} = \sqrt{\frac{8P}{R}} \sim 16\ A_{pp}\ , \qquad (4.22)$$

when A_{pp} is the peak-to-peak ampare and a 1 kW rf-amplifier is used.

The system used in the case of ^{37}K and ^{39}Ca is shown in Fig. 4.26.b. The transformer was used between the rf power-amplifier and the resonance LCR circuit, so that the impedance could be matched. The main feature of this system was a larger H_1, since we could make the resistance (R) smaller than that in the former case. The frequency modulation was narrower (see Equation (4.21)). R was limited to about 2 Ω, because of the resistance of the rf coil.

The characteristics of these two rf systems are summarized in Table 4.3. A typical amplitude of rf coil H_1 is shown in Fig. 4.27; H_1 was monitored using the voltage between both ends during runs.

	^{43}Ti case	^{37}K and ^{39}C case
H_0 magnetic field	6.87 kG	5.16 kG
Circuit	serial LCR	serial LCR
Center frequency	1.0 - 1.3 MHz	535 kHz for ^{37}K
		2.78 MHz for ^{39}Ca
Full width of frequency	0.12 - 0.40 MHz	30 kHz for ^{37}K
		0.10 MHz for ^{39}Ca
Resistor	50 Ω	~ 2 Ω
rf Amp	1 kW	1 kW
Inductance of rf coil	~ 35 μH	~ 27 μH for ^{37}K
		~ 16 μH for ^{39}Ca
H_1 magnetic field	~ 20 G	~ 30 G
rf Time	10 or 20 ms	10 ms

Table 4.3 Summary of the rf conditions for the ^{43}Ti experiment and ^{37}K and ^{39}Ca experiments.

4.4.2 NMR-chamber and NMR-magnet

The NMR-chamber is made of 3F-Tefron, which is good for a vacuum (out gassing is small). A drawing of this chamber is given in Fig. 4.28.

For the ^{43}Ti experiment, the Pt plate was cooled down to liquid-nitrogen temperature and then used as a catcher. (See Section 4.4.3 for details.) The liquid-nitrogen cryostat is shown in Fig. 4.29. The temperature at the catcher center was about 85 K without any rf. With rf (H_1 ~ 20 G and duty is 1/100), the temperature rise was about 3 K, which was negligible for

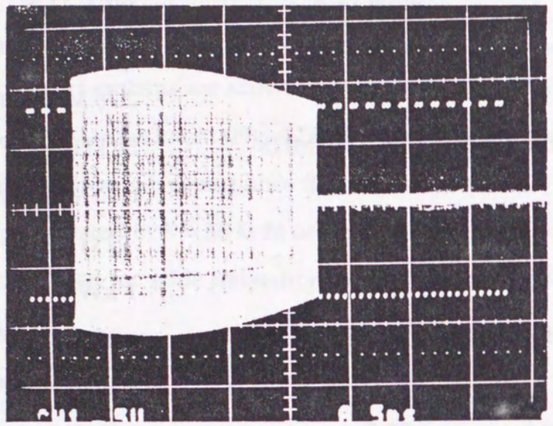

20 ms

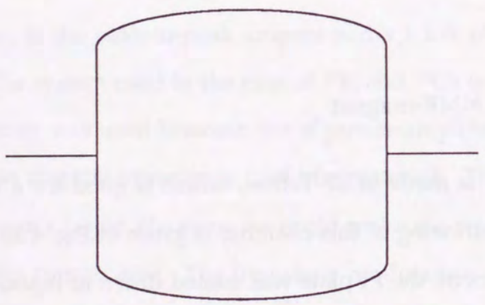

18.8	19.5	14.4	Voltage (V_{pp})
16.2	18.8	15.8	H_1 (G)
1.30		1.26	Frequency (MHz)

Fig. 4.27 Typical amplitude of rf magnetic field H_1.

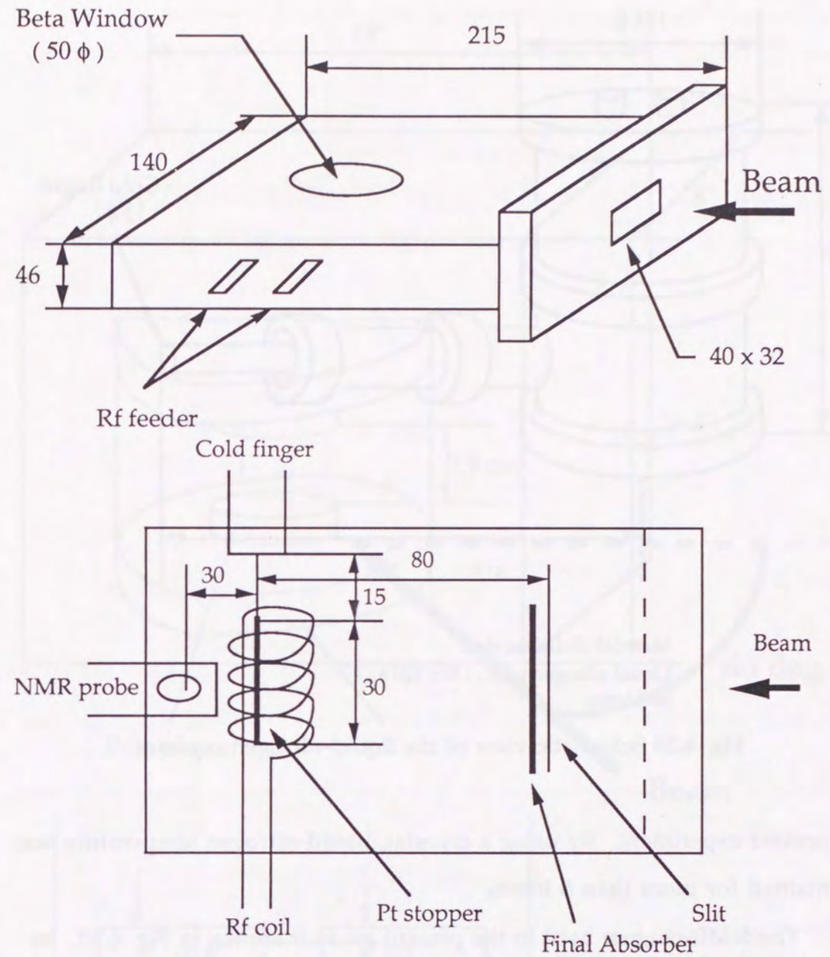

unit : mm

Fig. 4.28 Schematic view of the NMR-chamber.

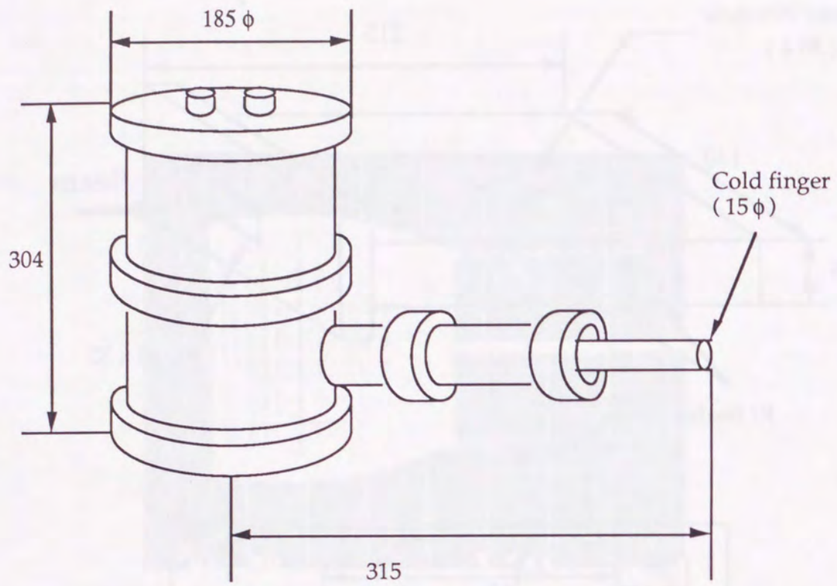

Material : Stainless steel
Liquid nitrogen tank : 120 x 120 ϕ
unit : mm

Fig. 4.29 Schematic view of the liquid-nitrogen cryostat.

the present experiment. By using a cryostat, liquid-nitrogen temperature was maintained for more than 8 hours.

The NMR-magnet used in the present study is shown in Fig. 4.30. Its pole faces were designed so as to improve the homogeneity of the magnetic field (H). The shape of the pole face is also shown in this figure. The characteristics of the magnet are summarized in Table 4.4. The observed deviation of the magnetic field is shown in Fig. 4.31. In this figure, the deviation in the magnetic field is defined by $\Delta H/H_{(r=0)}$ ($\Delta H=H_{(r)}-H_{(r=0)}$), where $H_{(r=0)}$ is the magnetic field at the center of the NMR-magnet. As

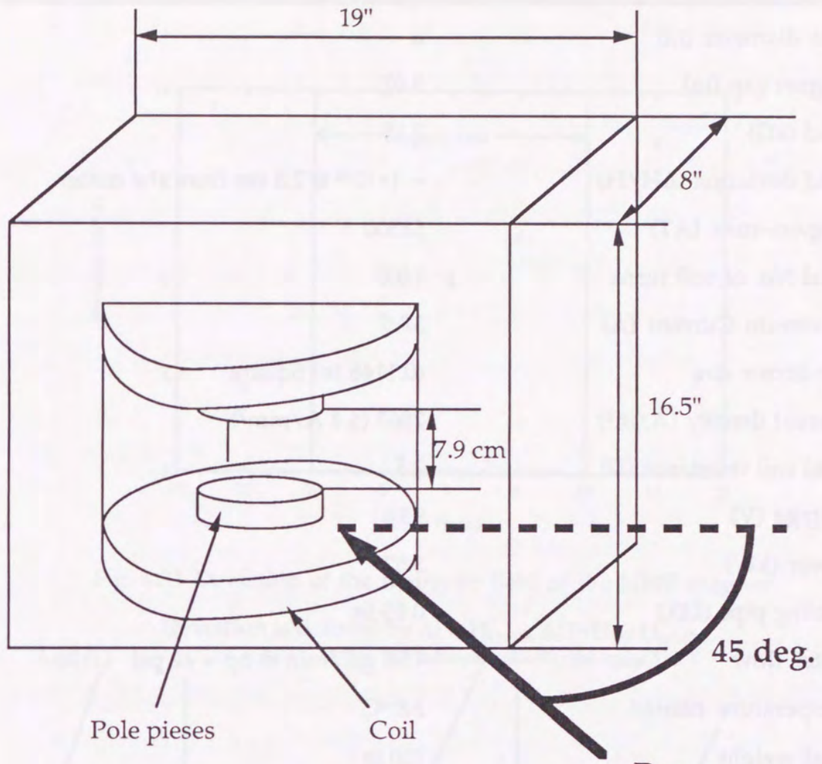

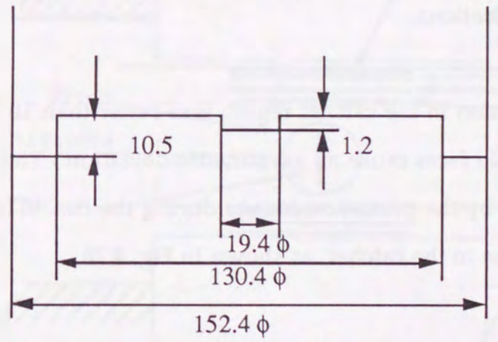

A vertical sectional picture of pole pieses.

Fig. 4.30 Schematic view of the NMR-magnet.

Pole diameter (in)	6
Magnet gap (in)	3.07
Field (kG)	7.15
Field deviation ($\Delta H/H$)	~ 1×10^{-3} @ 2.5 cm from the center
Ampere-turn (AT)	52500
Total No. of coil turns	1400
Maximum Current (A)	37.5
Conductor size	(0.1146 in) Square
Current density (A/in^2)	2863 (4.4 A/mm^2)
Total coil resistance (Ω)	2.5
Voltage (V)	93.8
Power (kW)	3.52
Cooling pipe (I.D.)	0.15 in
Water flow	4.98 gal/min @ Δp = 42 psi
Temperature rise	2.8 °C
Total weight	720 lb

Table 4.4 NMR-magnet specifications.

shown in the figure, the deviation in the catcher region was better than 10^{-3}. (The slight gradients of the pole faces cause an asymmetric deviation.) The magnetic field was monitored by the proton resonance during the run. The monitor point was located close to the catcher, as shown in Fig. 4.28.

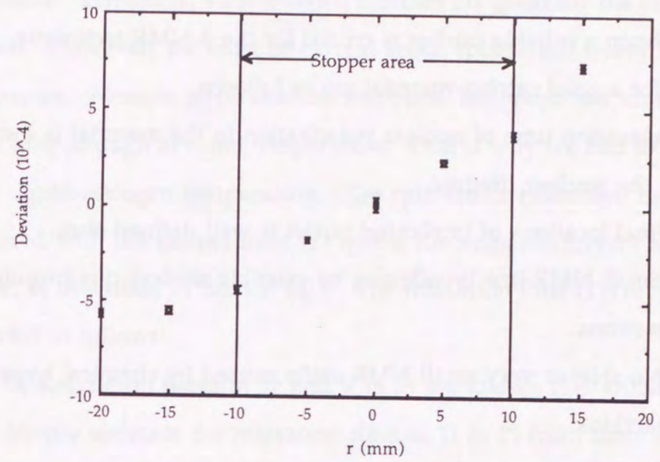

Fig. 4.31 Deviation of the magnetic field of the NMR-magnet.

Deviation is defined by $\Delta H/H_{(r=0)}$, $\Delta H = H_{(r)} - H_{(r=0)}$.

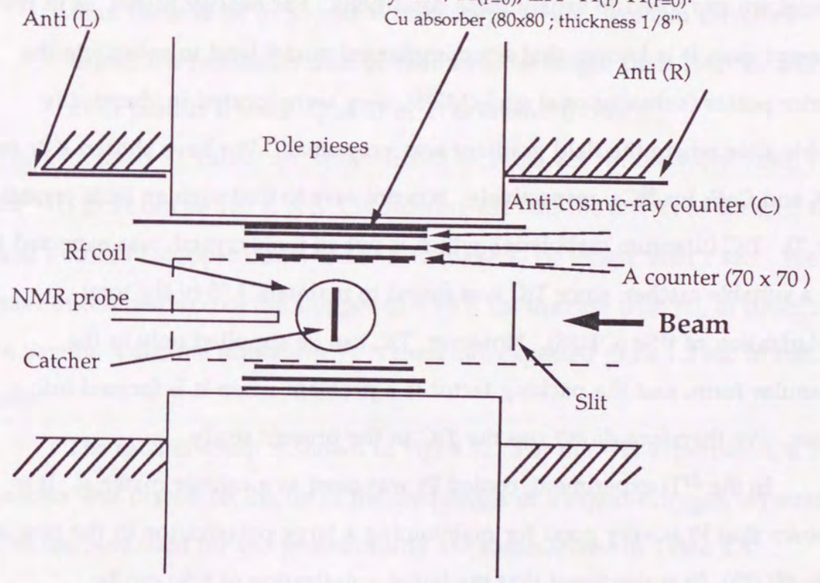

Fig. 4.32 Typical setup around the catcher. (A vertical sectional figure.)

4.4.3 Implantation media (Fragment catcher)

To obtain a suitable catcher is crucial for the β-NMR technique. The conditions for a good catcher-material are as follows:

(i) Relaxation time of nuclear polarization in the material is longer than the nuclear lifetime.

(ii) Final locations of implanted nuclei is well defined sites.

(iii) Small NMR-line broadening by possible nuclear quadrupole interactions.

(iv) No shift or very small NMR shifts caused by chemical hyperfine interactions.

(v) Easy to prepare and purchase.

Ionic crystals with cubic symmetry containing isotopes of the implanted nuclei are supposed to satisfy these conditions. For heavier nuclei, as in the present case, it is known that since implanted nuclei tend to substitute the lattice points (substitutional site) (MI76), they were located in chemically stable sites where the field gradient was very small. We have chosen KBr for ^{37}K and CaF_2 for ^{39}Ca, respectively. It is not easy to find such an ionic crystal for Ti. TiC (titanium carbolyde), which is not an ionic crystal, was expected to be a suitable catcher, since TiC was found to maintain 1/5 of the total polarization of ^{41}Sc (OH88). However, TiC can be supplied only in the granular form, and the packing factor is a problem when it is formed into a plate. We therefore didn't use the TiC in the present study.

In the ^{43}Ti experiment, cooled Pt was used as a catcher material. It is known that Pt is very good for maintaining a large polarization in the case of ^{41}Sc (SU73). (It is predicted that the initial polarization of ^{41}Sc can be maintained in the catcher.) Pt is a paramagnetic metal with a fcc structure

(cubic). It is thus expected that the initial polarization of ^{43}Ti can be maintained. Generally, such metallic samples are good for the catcher material. However, we must be careful about spin-lattice relaxation phenomena. Because of conduction electrons, the relaxation time (T_1) may not be long enough at room temperature. That is why we had to cool it down to the liquid-nitrogen temperature. The spin-lattice relaxation time (T_1) is associated with the temperature (T) by the Korringa relation for a metal sample, as described in Section 3.2.1. The relaxation time (T_1) of ^{43}Ti in Pt was estimated as follows:

(i) Relaxation times of Sc and V in Pt are known (TE74)(IN80). We can simply estimate the relaxation time of Ti in Pt from these examples because the Ti was located just between Sc and V in the periodic table.

(ii) It is well known that relaxation times of Sc and V in Pt are longer than those of Sc in Sc and V in V, respectively. We can therefore expect the relaxation time of Ti in Pt to be longer than Ti in Ti, and even predict it since T_1 of Ti in Ti is known (NA67).

The estimated T_1 values are summarized in Table 4.5. In the worst case, T_1T for ^{43}Ti in Pt can be 120 K sec. Considering the half-life of ^{43}Ti (~ 0.5 sec), we had to cool Pt stopper down to 120 K to make T_1 be longer than 1 sec. We have succeeded to cool the stopper to ~ 90 K (in the case with rf), as described in Section 4.4.2; the minimum T_1 is therefore expected to be 1.3 sec in this case.

The catcher setup is shown in Fig. 4.32. For the ^{43}Ti experiment, a Pt catcher was placed on the tip of the cold finger of a liquid-nitrogen cryostat. The catchers used for the present study are summarized in Table 4.6.

	^{45}Sc	^{43}Ti	^{49}Ti	^{51}V
I	7/2	7/2	7/2	7/2
g-factor	+1.359 [1]	[0.20]	-0.315 [1]	+5.1487 [1]
Q (b)	-0.22 [1]	[-0.21]	+0.24 [1]	-0.033/-0.052 [1]
T_1T_{exp} (pure) (s K)	1.6(1) [2]	[370(60)]	150(20) [3]	0.795 [4]
T_1T_{exp} (in Pt) (s K)	20(3) [2]	[120 ~ 4000]	[50 ~ 1500]	2.3(3) [5]

1) Atomic Data and Nuclear Data Table 42 (1989) 189

2) Journal of Phys. Soc. Japan 36 (1974) 130

3) Physical Review 162 (1967) 162

4) Journal of Phys. Soc. Japan 22 (1967) 238

5) Journal of Phys. Soc. Japan 48 (1980) 1123

Table 4.5 Predictions of relaxation-time ^{43}Ti in Pt.

Square brackets indicate the prediction values.

	^{37}K	^{39}Ca	^{43}Ti
Material	KBr	CaF_2	Pt
	Ionic crystal	Ionic crystal	Metal
density	2.1 g/cm^3	3.2 g/cm^3	21.7 g/cm^3
Thickness	~ 0.5 mm	0.3 mm	0.1 mm

Table 4.6 Summary of catchers used for the present study.

(Anti L & R)

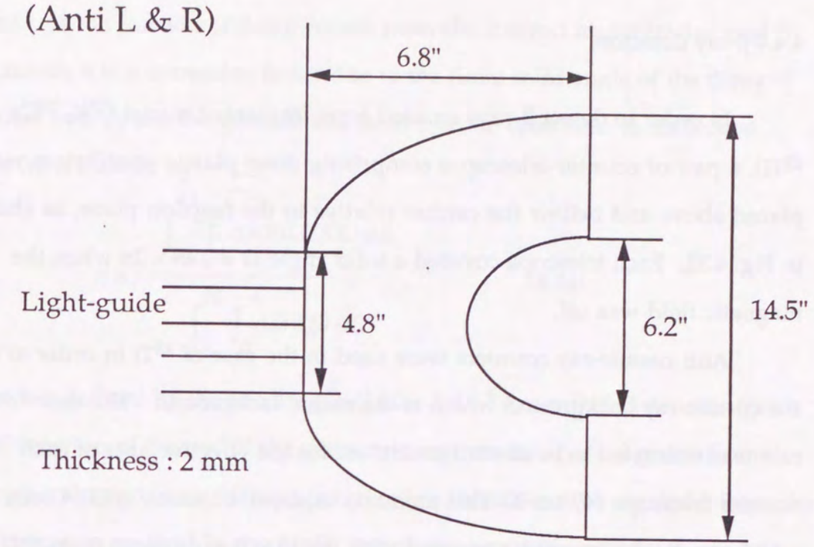

(Anti C)

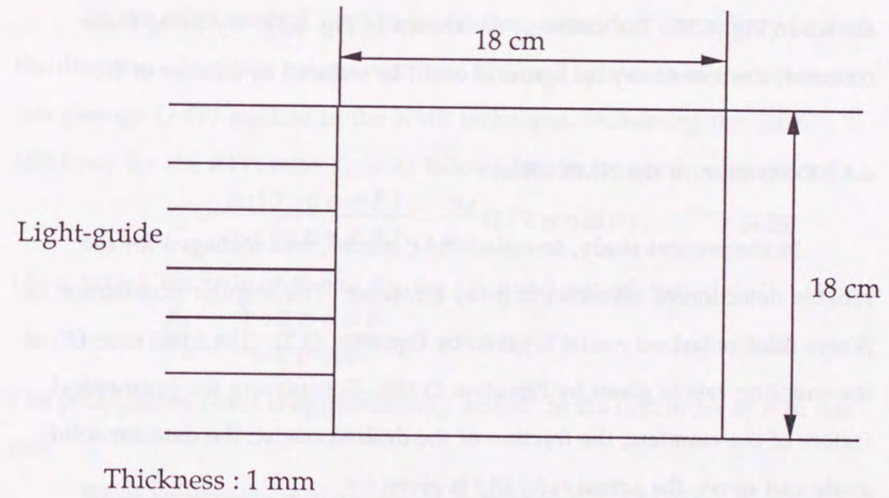

Fig. 4.33 The anti-cosmic-ray counters.

4.4.4 β-ray detectors

In order to detect β-rays emitted from implanted nuclei (^{37}K, ^{39}Ca and ^{43}Ti), a pair of counter-telescopes comprising three plastic scintillators was placed above and bellow the catcher relative to the reaction plane, as shown in Fig. 4.32. Each telescope covered a solid angle $\Omega = 0.45 \times 2\pi$ when the magnetic field was off.

Anti cosmic-ray counters were used in the case of ^{43}Ti in order to reject the cosmic-ray background which is the major background. The cosmic-ray rate was estimated to be about 1 count/sec for the effective area of each counter telescope (49 cm^2). This amounts to about 4 counts/spill (4 sec), which can not be ignored compared with the true β-ray counts from ^{43}Ti (~ 40 counts/spill were expected for the case of an Au target.). The anti cosmic-ray counters were placed in between the β-counters and the NMR-magnet, as shown in Fig. 4.32. The counters are shown in Fig. 4.33. By using these counters, the cosmic-ray background could be reduced by a factor of 10.

4.4.5 Derivation of the NMR effect

In the present study, so-called "8AP mode", was managed for the reliable detection of asymmetric β-ray emission. The angular distribution of β-rays from polarized nuclei is given by Equation (3.1). The ideal ratio (R) of the counting rate is given by Equation (3.10). Considering the geometrical factors of the counters, the fraction of the desired nuclei, the detector solid-angle and so on, the actual ratio (R_I) is given by

$$R_I = \frac{\varepsilon_U (1 + \alpha \eta \mathcal{A} P)}{\varepsilon_D (1 - \alpha \eta \mathcal{A} P)} \sim \frac{\varepsilon_U}{\varepsilon_D} (1 + 2 \alpha \eta \mathcal{A} P) , \qquad (4.23)$$

where α is the fraction of β-ray counts from the desired nuclei in the total β-ray counts; η is a correction factor due to the finite solid angle of the β-ray counters and ε's are the geometrical factors of the counters. A correction factor (η) is defined by

$$\eta \equiv \frac{\int_{Ei}^{Ef} \int_0^a \cos\theta \, d\Omega \, f(E) \, dE}{\int_{Ei}^{Ef} \int_0^a d\Omega \, f(E) \, dE} , \qquad (4.24)$$

where a is defined by the solid angle Ω ($\Omega = 2\pi (1 - \cos a)$); $f(E)$ denotes the Fermi function of β-rays. If the geometric asymmetry ($\varepsilon_U / \varepsilon_D$) given from separate measurements without polarization (which can be obtained from the depolarization method in the NMR technique) the polarization (P) can be obtained. In this mode, the asymmetry from the polarization effect to be observed is approximately $2\alpha\eta\mathcal{A}P$, taking the first order of the polarization.

In the other method used to cancel the geometrical asymmetry ($\varepsilon_U / \varepsilon_D$), the direction of nuclear polarization was inverted by means of the adiabatic fast passage (AFP) method in the NMR technique. Assuming the 100% efficiency for the AFP, ratio R_{II} is as follows for the inverted polarization:

$$R_{II} = \frac{\varepsilon_U (1 - \alpha \eta \mathcal{A} P)}{\varepsilon_D (1 + \alpha \eta \mathcal{A} P)} \sim \frac{\varepsilon_U}{\varepsilon_D} (1 - 2 \alpha \eta \mathcal{A} P) . \qquad (4.25)$$

Upon taking the ratio of R_I and R_{II}, the ε's cancel out, giving

$$\frac{R_I}{R_{II}} = \frac{1 + 2 \alpha \eta \mathcal{A} P}{1 - 2 \alpha \eta \mathcal{A} P} \sim 1 + 4 \alpha \eta \mathcal{A} P . \qquad (4.26)$$

The polarization effect is approximately $4\alpha\eta\mathcal{A}P$ in the first order of P in this case.

Since asymmetry measurements with inverted polarization were carried out during different beam-count cycles in the method mentioned

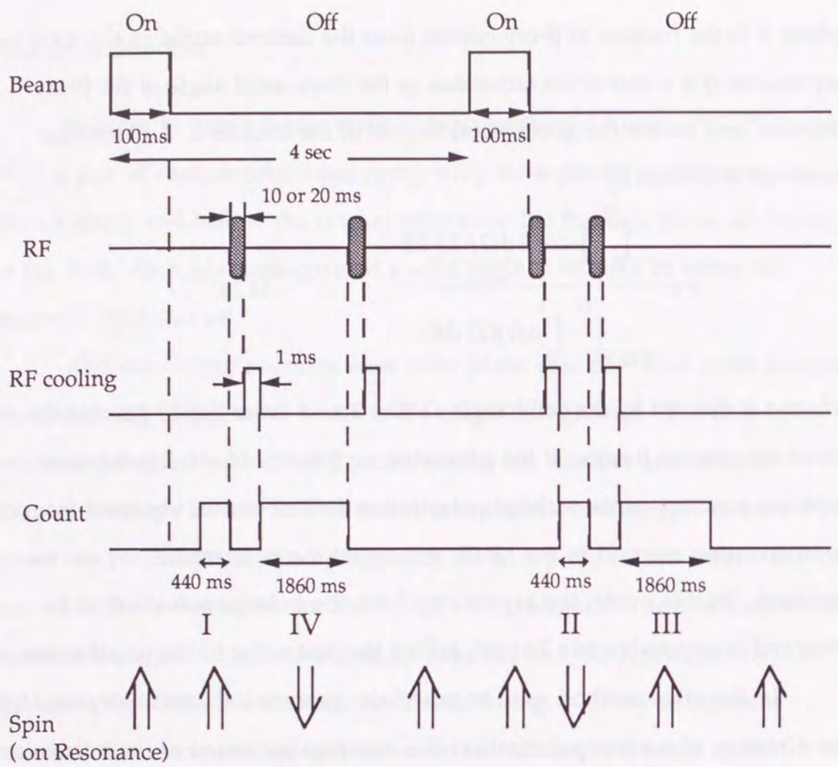

Fig. 4.34 Timing chart of the 8AP mode.

above, beam-fluctuation may cause a periodic changing the intensity and/or position; it often induce a small spurious polarization effect. In other words, any geometrical asymmetry in the counters can remain uncanceled in the case of above the AFP mode. In order to reject asymmetry, we developed a more advanced spin-handling technique. In this technique, the beam time was followed by two counting sections. Polarization was then inverted in between the two counting section. A pair of beam-count cycles with a

reversed spin sequence was repeated, as shown in Fig. 4.34. The ratio of R_I and R_{IV} is given by

$$\frac{R_I}{R_{IV}} = \frac{1 + 2\,\alpha\,\eta\,\mathcal{A}\,P}{1 - 2\,\alpha\,\eta\,\mathcal{A}\,P} \sim 1 + 4\,\alpha\,\eta\,\mathcal{A}\,P\,. \qquad (4.27)$$

We thus don't have to worry about the effect of the beam-fluctuation, since the R_I and R_{IV} are measured during the same beam-count cycle. We can make another ratio of R_{II} and R_{III}. By combining these two ratios, we can obtain the NMR effect free from any possible spurious effects as,

$$R = \frac{R_I\,R_{III}}{R_{IV}\,R_{II}} \sim \frac{1 + 4\,\alpha\,\eta\,\mathcal{A}\,P}{1 - 4\,\alpha\,\eta\,\mathcal{A}\,P} \sim 1 + 8\,\alpha\,\eta\,\mathcal{A}\,P\,. \qquad (4.28)$$

In this case the asymmetry is approximately $8\alpha\eta\mathcal{A}P$ in the first order of P. This is why we call it the "8AP mode". The polarization effect ($\alpha\eta\mathcal{A}P$) without an approximation is

$$\alpha\,\eta\,\mathcal{A}\,P = \frac{R^{1/4} - 1}{R^{1/4} + 1}\,. \qquad (4.29)$$

4.4.6 Data taking and control system

Circuit and block diagrams of the β-ray detection system are shown in Figures 4.35 and 4.36, respectively. The coincidence logic for $A\otimes B\otimes B'\otimes\bar{L}\otimes\bar{R}\otimes\bar{C}$ was created from the signals of the β-counters and was registered by the scalers inside a personal computer. The personal computer (NEC's PC9801) was used to read the data accumulated in the scalers, reset and restart the scalers at the proper timings. The data was analyzed and stored into floppy disks by the computer.

A block diagram describing the control of the rf system is given in Fig. 4.37. The computer was used to control the time sequence of the rf system,

i.e., to generate the proper timing for the rf time and the cooling time of the rf.

In the present study we used two computers in order to reduce the dead time during data accumulation. A flow chart of the program for data-taking and rf control is shown in Appendix 6.

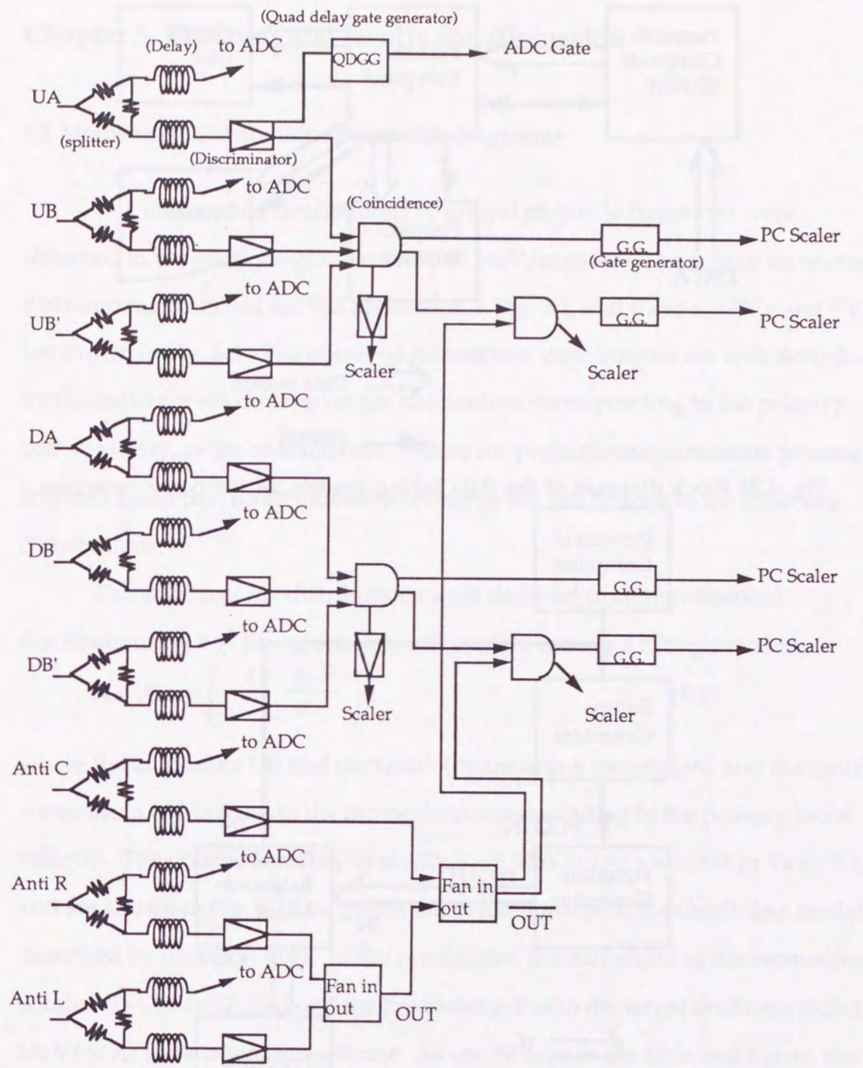

Fig. 4.35 Electronics used in the β-ray detection.

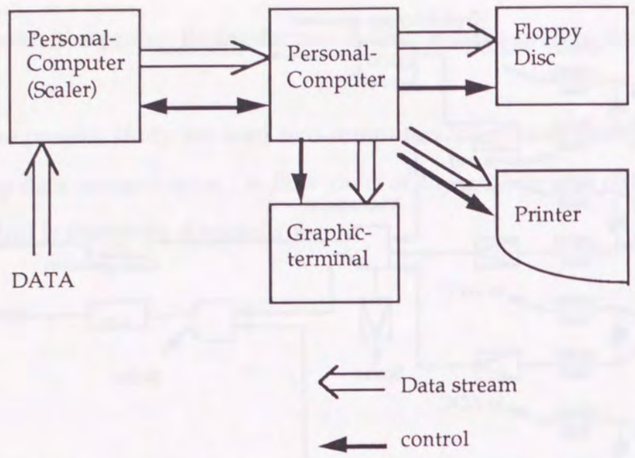

Fig. 4.36 Block diagram of the data taking system for the β-ray detection.

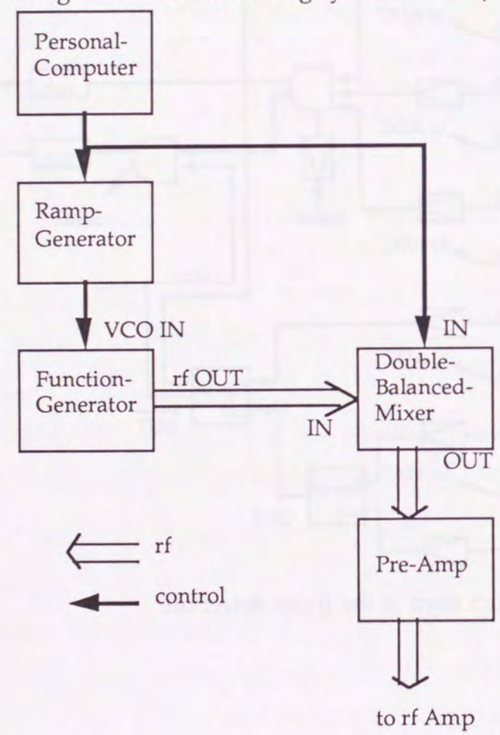

Fig. 4.37 Block diagram of rf control system.

Chapter 5. Experimental results and discussion

5.1 Momentum distribution of projectile fragments

The momentum distributions of several projectile fragments were observed in the energy region around 100 MeV/nucleon. The typical momentum distributions observed for ^{43}Ti are shown in Fig. 5.1, and those for ^{39}Ca and ^{37}K are shown in Fig. 5.6. The observed momentum distributions are well described by Gaussian curves centered at the momentum corresponding to the primary beam velocity, as the characteristic feature for projectile-fragmentation process. It is also noted that no significant low-energy tail can be seen in the observed distributions.

The widths of the distributions were deduced from the observed distributions by a χ^2 fitting analysis using a Gaussian as a fitting function,

$$N = A \exp\left\{ -\frac{(p - p_0)^2}{2\sigma^2} \right\}, \qquad (5.1)$$

where the amplitude (A) and the width (σ) are fitting parameters, and the central momentum (p_0) is fixed to the momentum corresponding to the primary beam velocity. The obtained widths (typically 3 ~ 5 MeV/c/A) are listed in Table 5.1, and are shown in Fig. 5.2 along with the predictions from the Goldhaber model described by Equation (2.7). In the predictions, the half width of the momentum window (~1.9 MeV/c/A) and the broadening due to the target thickness (0.5~2.5 MeV/c/A) were taken into account. As can be seen in the table and figure, the obtained widths are fairly consistent with the predictions from the Goldhaber model. This shows that in the present energy region (~100 MeV/nucleon) the projectile-fragmentation process already overtakes the transfer process, which is

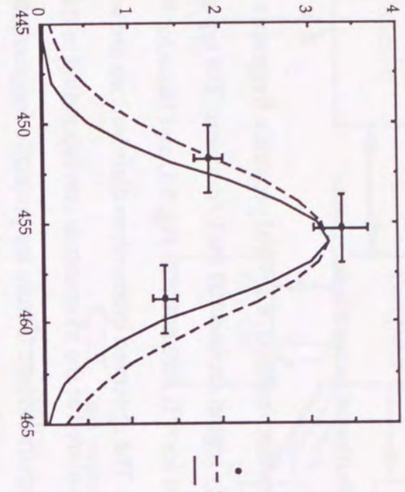

(a) The case of Au target ; $\theta = 2.0 \pm 1.1$ deg.

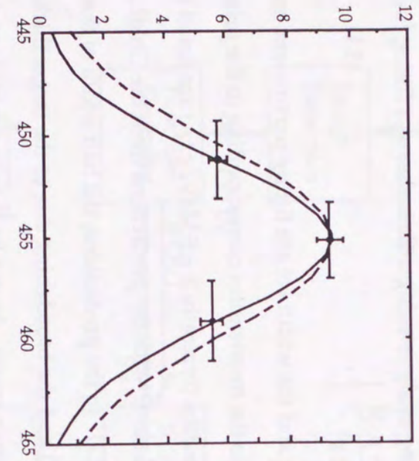

(b) The case of C target ; $\theta = 1.5 \pm 0.7$ deg.

Fig. 5.1 Typical momentum distributions of the ^{43}Ti fragment.
Solid lines denote the best fit from Equation (5.1). σ_{Tot} in Table 5.1 is used as the theoretical value (dashed lines).

Incident nuclei	^{40}Ca				^{40}Ca			^{46}Ti		
Target	Au				Au			Au	C	
Fragment	^{37}K				^{39}Ca			^{43}Ti	^{43}Ti	
Angle (deg)	0.0(6)	1.5(6)	2.0(6)	2.5(6)	0.0(6)	2.0(6)	2.5(6)	2.0(11)	0.0(3)	1.5(7)
σ_{obs} (MeV/c/A)	5.5(4)	5.6(5)	5.0(2)	5.1(4)	4.6(3)	3.4(1)	3.3(1)	3.1(5)	4.5(2)	3.9(1)
σ_{wid} (MeV/c/A)	1.9				1.9			1.7	1.9	
σ_{tar} (MeV/c/A)	0.5				0.5			0.9	2.5	
σ_{Gold} (MeV/c/A)	4.6				2.6			4.0		
σ_{Tot} [1] (MeV/c/A)	5.0				3.3			4.4	5.1	

1) $\sigma_{Tot} = \sqrt{(\sigma_{wid})^2 + (\sigma_{Tar})^2 + (\sigma_{Gold})^2}$

Table 5.1 Analysis of momentum distribution of ^{37}K, ^{39}Ca and ^{43}Ti.
"obs" means the experimental values of the present study. "wid", "tar" and "Gold" indicate the momentum-window width, the broadening due to difference of the energy loss in target material and the width from the Goldhaber model including the relativistic correction.

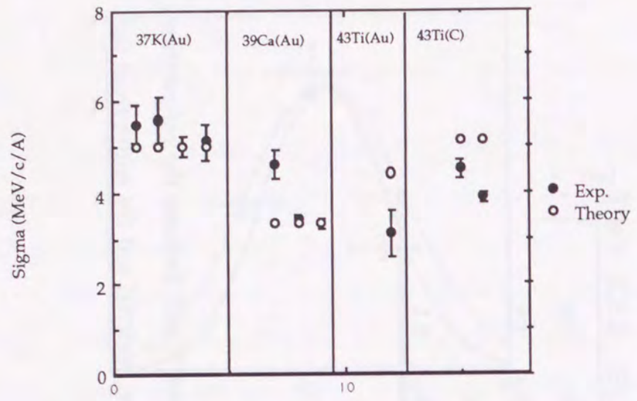

Fig. 5.2 Experimental widths of the momentum distribution.
Closed and open circles mean the experimental widths (σ_{obs} in Table 5.1) and theoretical widths (σ_{Tot} in Table 5.1), respectively.

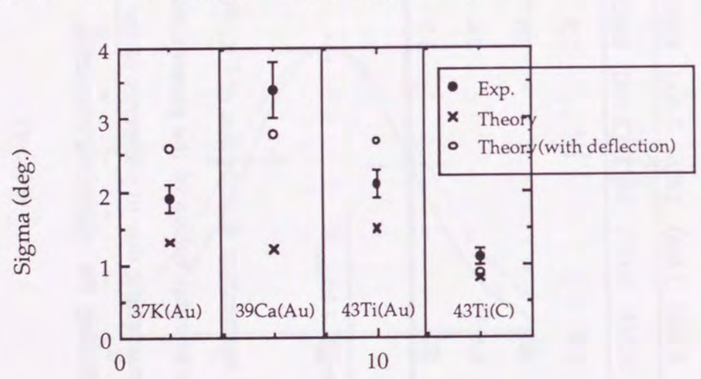

Fig. 5.4 Experimental widths of the angular distribution.
Closed and open circles mean the experimental widths (σ_{obs} in Table 5.2) and theoretical widths without deflection (σ_{Tot}' in Table 5.2), respectively. Crosses mean the theoretical widths with deflection (σ_{Tot} in Table 5.2).

observed at lower energies (10~80 MeV/nucleon), as has also been discussed by other authors (GU83).

We also observed the momentum distributions at different production angles for some fragments. The shapes of the distributions were quite similar to those observed at 0°, and the widths were almost independent of the production angle, as shown in Table 5.1.

5.2 Angular distribution of projectile fragments

The angular distributions were observed for several fragments produced through collisions with both heavy and light targets, i.e., Au and C. In order to obtain the angular distribution, it is usually necessary to integrate the momentum distribution. However, this procedure was not necessary in the present case, where the observed momentum distributions have similar shapes and widths for different production angles, as already described in the former section. The typical angular distributions obtained for ^{43}Ti are shown in Fig. 5.3. The observed angular distributions were well described by Gaussian distributions as the momentum distributions.

From a χ^2 fitting analysis of these angular distributions using a function similar to Equation (5.1) with $p_0 = 0$, the widths of the angular distributions were obtained (Table 5.2); they shown in Fig. 5.4 along with predictions from the Goldhaber model. (The obtained widths are 1.1 ~ 3.4 deg..) In the predictions, the half width of the angle slit (0.6~1.1 deg.), the broadening due to multiple-scattering of the fragments in the target (0.1~0.9 deg.) and the angular spread of the primary beam (0.6 deg.) were taken into account (The calculation method to obtain the multiple-scattering is shown in Appendix 1-(2).). In the relativistic energy region, the Goldhaber model explains not only the widths of the

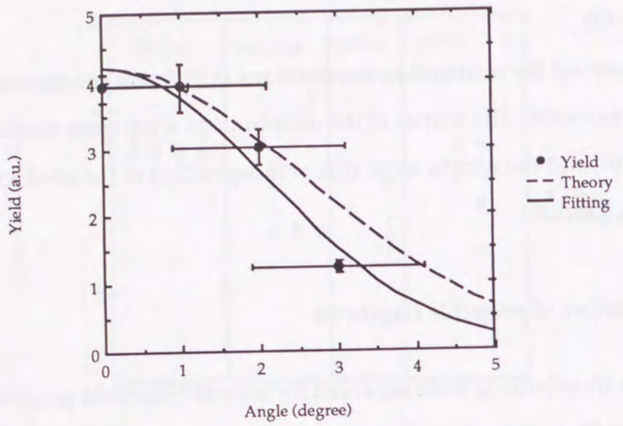

(a) The case of Au target

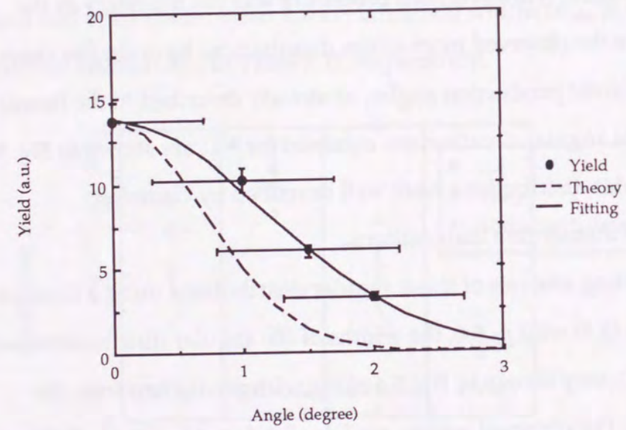

(b) The case of C target

Fig. 5.3 Typical angular distributions of the ^{43}Ti fragment.
Solid lines denote the best fit from Equation (5.1) with p_0=0. σ_{Tot}' in Table 5.2 is used as the theoretical width (dashed lines).

Incident nuclei	^{40}Ca	^{40}Ca	^{46}Ti	
Target	Au	Au	Au	C
Fragment	^{37}K	^{39}Ca	^{43}Ti	^{43}Ti
σ_{obs} (deg)	1.9(2)	3.4(4)	2.1(2)	1.1(1)
σ_{wid} (deg)	0.8	0.8	1.3	0.7
σ_{Gold} (deg)	0.5	0.3	0.5	0.5
σ_{sct} (deg)	0.9	0.9	0.6	0.1
σ_{def} (deg)	+2.3	+2.5	+2.2	-0.3
σ_{Tot}' (deg) [1]	1.3	1.2	1.5	0.8
σ_{Tot} (deg) [2]	2.6	2.8	2.7	0.9

1) $\sigma_{Tot}' = \sqrt{(\sigma_{wid})^2 + (\sigma_{Gold})^2 + (\sigma_{sct})^2}$

2) $\sigma_{Tot} = \sqrt{(\sigma_{wid})^2 + (\sigma_{Gold})^2 + (\sigma_{sct})^2 + (\sigma_{def})^2}$

Table 5.2 Analysis of the angular distribution of ^{37}K, ^{39}Ca and ^{43}Ti.
Here, "obs" means the experimental value of the present study; "wid", "Gold", "sct" and "def" indicate the angular-window width, including broadening of the incident beam on targets (±10 mrad), the width from the Goldhaber model, the broadening due to multiple scattering inside the target and the broadening due to the orbital deflection, respectively.

momentum distributions of the fragments, but also the widths of the angular distributions. However, the present experimental widths are significantly broader than the predictions from the model, for both heavy and light targets. This is one of the characteristic features of the projectile-fragmentation process in the present energy region (~ 100 MeV/u), as shown in other experiments (BI79).

The broad angular distributions of the fragments can be understood in terms of the Coulomb deflection in the case of heavy targets, like Au. However,

Coulomb deflection is not sufficient for explaining broadening in the case of a light targets. In such cases, the attractive nuclear force is supposed to play an important role in the deflection of fragments. This leads to the idea of orbital deflection of the fragments by a combined Coulomb-nuclear potential of the target, as was first introduced by Bibber et al.(BI79). In order to understand the present broadening of the observed angular distributions, the classical deflection angles given by the combined Coulomb-nuclear potential were estimated based on their idea. The Woods-Saxon potential with a radius parameter (r_0) of 1.2 fm, a diffuseness parameter (a) of 0.6 fm, and a well depth (V_0) of 65 MeV was used for the nuclear potential; we took V_0 from that given by one nucleon in the low-energy region, since no observation has been made of the present energy and mass regions. A point-charge Coulomb-potential and a potential with parabolic form were used in the nuclear interior and inside the nucleus, respectively. The combined potential is therefore given by

$$V(r) = \frac{-V_0}{1+\exp((r-R_{eff})/a)} + V_c(r) \qquad (5.2)$$

and

$$V_c(r) = 1.44\frac{Z_p Z_t}{r}\ (\mathrm{MeV}) \quad \text{for } r > R_{eff}$$
$$= 0.72\frac{Z_p Z_t}{r}\left[3-\left(\frac{r}{R_{eff}}\right)^2\right] \quad \text{for } r < R_{eff}\ ,$$

where Z_p and Z_t are the atomic numbers of the projectile and the target, respectively, and R_{eff} is the sum of the nuclear radii of the projectile and target nuclei. The impact parameter (b) depends on the fragments. We used the optimum impact parameters obtained from a calculation involving the abrasion-ablation model. The calculated deflection angles (-0.3 ~ +2.5 deg.) are also summarized in Table 5.2. It is noted that the sign of the deflection angle is predicted to be positive for Au target, due to the strong Coulomb field, and to be negative for C target due to the relatively strong nuclear force, compared with

the Coulomb force. Comparing the theoretical widths, including the deflection angle ($\sigma_{Tot}{}^{2)}$) with the experimental widths (σ_{obs}) given in the table and figure, we can understand that the broadening is almost explained by the orbital deflection due to the combined Coulomb-nuclear potential of the target.

Although the orbital deflection by the combined Coulomb-nuclear potential explains the broad angular distributions, this picture conflicts with the conclusions by Wong et al. (WO82) and Silk et al. (SI88) concerning the sign of the scattering angle; they pointed out that the positive-angle scattering is dominant, regardless of the target (See Chapter 2.3.). Polarization measurements were required in order to make any conclusive statements concerning this matter.

5.3 Production cross-sections of projectile fragments

The production cross-sections for the fragments were obtained by integrating both the momentum and angular distributions. The observed production cross-sections for ^{37}K and ^{39}Ca fragments are 4.3 (10) mb, 72 (18) mb for Au target, and the observed production cross-sections for the ^{43}Ti fragment are 0.33 (8) mb and 1.27 (24) mb for Au and C targets, respectively, as shown in Table 5.3. The predictions obtained from the abrasion-ablation model (HÜ75) and an empirical model by Silberberg and Tsao (SI73) (The cross-sections are calculated by the computer code "FRAGBNL".) are also shown in the table. The predictions for ^{37}K and ^{39}Ca fragments by the abrasion-ablation model (the empirical model) are 17 mb (176 mb) and 147 mb (124 mb) for an Au target; the predictions for ^{43}Ti fragment are 3.0 mb (14.4 mb) and 1.7 mb (7.1 mb) for Au and C targets, respectively, as also shown in the table. All of the observed cross-sections are smaller than any of the predictions. In most situations, the abrasion-

Incident (MeV/nucleon)	^{40}Ca (119)		^{46}Ti (125)	
Target	Au		Au	C
Fragment	^{37}K	^{39}Ca	^{43}Ti	^{43}Ti
σ(Exp) (mb)	4.3(10)	72(18)	0.33(8)	1.27(24)
σ(FRAGBNL) (mb)	176	124	14.4	7.1
σ(Abrasion) (mb)	12	161	4.0	2.2
σ(Abrasion-Ablation) (mb)	17	147 *	3.0	1.7

FRAGBNL ; calculation by the computer code "FRAGBNL"

Abrasion ; calculation based on the abrasion model (HÜ75)

Abrasion-Ablation ; calculation based on the abrasion-ablation model (HÜ75)

* ; including the cross section of the electromagnetic dissociation

Table 5.3 Production cross sections of ^{37}K, ^{39}Ca and ^{43}Ti.

	^{38}K (g.s.)	^{38m}K
Excitation level	0 MeV	0.13 MeV
Nuclear spin	3^+	0^+
Transition	$3^+ \Rightarrow 2^+$	$0^+ \Rightarrow 0^+$
Half-life	7.636(18) min	923.9(6) msec
Branching ratio	99.849(12) %	100 %
β-ray energy	2.85 MeV	5.02. MeV

Table 5.4 β-decay information for ^{38m}K and ^{38}K(g.s.) (EN90).

ablation model fits the data better, except for the three-neutron removal case (^{46}Ti --> ^{43}Ti). In this case, the cross-section for the Au target is significantly smaller than that for the C target. The target-mass dependence of the cross-section can not be reproduced by these models, in which the cross-section increases as the target mass. This result suggests that a new process, such as Coulomb breakup during fragmentation, plays an important role in the three-neutron removal case, in addition to the abrasion-ablation process.

5.4 Production ratio between the yields of the ground and isomeric states of ^{38}K

Fragments are usually in excited states immediately after a collision. It is interesting to study the production cross sections as a function of the excitation energies. Although such studies are not easy, and have been rarely done, when the fragments are in an isomeric state, the production cross section can be obtained for this state, in addition to the ground state. This may lead to a better understanding of excitation after a collision.

For this purpose, we observed the production ratio of the ground state ^{38}K to its isomeric state ^{38m}K in a ^{40}Ca on Au collision at 106 MeV/nucleon. They were able to be separated by the difference in their β-decay lifetimes. As can be seen in the decay properties for ^{38}K and ^{38m}K (summarized in Table 5.4), the half-lives are 0.93 sec and 7.6 min, for ^{38m}K and ^{38}K, respectively. In the present time scale (4 sec), the half-life of the ground state can be treated as a constant component in the β-ray time-spectrum.

The observed time spectrum is shown in Fig. 5.5. We analyzed the time spectrum by a χ^2 fitting analysis using a function,

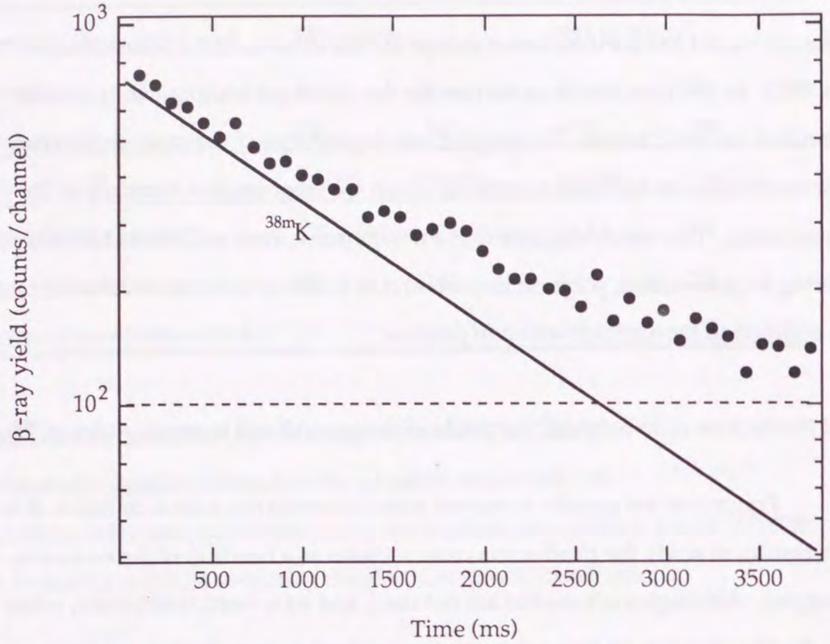

Fig. 5.5 Typical β-ray time spectrum of the ^{38}K and ^{38m}K.
The solid and dashed lines denote the components of ^{38m}K and the constant, respectively.

$$N_\beta(t) = A_1 \exp\left(-\frac{\ln 2}{930}t\right) + A_2 \ , \qquad (5.3)$$

where the amplitudes (A_1 and A_2) of the two components are the fitting parameters. In order to obtain the production ratio, the decaying component and the constant component were integrated individually over the counting time. In the present observation, cosmic-rays were the major background. From an off-line check, the count rate of the cosmic-ray background in the present counter system was determined to be 85 (4) counts/min. We therefore subtracted the total number of cosmic-ray counts in the present observation time (15.4 min) from the integrated counts for the constant component. The production ratio of

the isomeric state to the ground state without other corrections described later was thus deduced to be

$$(^{38m}\mathrm{K} \,/\, ^{38}\mathrm{K})_{\mathrm{n.c.}} = 3.62(24) \ . \qquad (5.4)$$

Although the β-ray counting time was only 15.4 min, we spent more than 90 min to adjust the detection circuits, which was long enough to saturate the ^{38}K component, whose half-life is 7.6 min. We therefore didn't need to correct the pile-up effect on the yield of ^{38}K. However, corrections due to a difference in the β-ray maximum energy had to be considered. In this experiment, we used a strong magnetic field (H_0 ~ 5.2 kG) in order to increase the detection efficiency of β-rays. We had to correct the difference in the effective solid angle caused by the difference in the maximum β-ray energy. The difference in the maximum β-ray energy also caused a difference in the detection efficiency, due to the finite threshold energy. The correction factor for these effects was calculated to be $\Omega(^{38m}\mathrm{K})/\Omega(^{38}\mathrm{K}) = 1.26(36)$, where the error came from the ambiguity in the threshold energy of the present β-ray counting system (1.4(2) MeV). Thus, the final result including the correction is obtained as

$$\begin{aligned}(^{38m}\mathrm{K}/^{38}\mathrm{K})_{\mathrm{corr.}} &= \Omega(^{38}\mathrm{K})/\Omega(^{38m}\mathrm{K}) \times (^{38m}\mathrm{K}/^{38}\mathrm{K})_{\mathrm{n.c.}} \\ &= 2.9\ (8)\ . \qquad (5.5)\end{aligned}$$

The ground and isomeric states are populated after cooling down by γ-ray emission from the excited states of ^{38}K. The production ratio thus contains information concerning the initial excitation energy at the collision. According to the abrasion-ablation model, the populations of the excited levels can be estimated. In the case of a one-nucleon removal channel, the predicted population decreases sharply with the excitation energy; the population is proportional to (a - Ex), where a denotes a constant and Ex is the excitation energy. On the other hand, the population has the optimum excitation energy for

three- and more-nucleon removal-channels (Below the particle-emission thresholds, the population is proportional to the excitation energy; population ∝ *Ex.*). In the case of ^{38}K, where two nucleons have to be removed from the incident ^{40}Ca beam, the population function should be in an intermediate situation. Since the energy levels and branching ratios of γ-decays have been well investigated below the proton threshold-energy for the ^{38}K (EN90), we can deduce the ground-isomer production ratio when the population function is known. The ratio must therefore be a good testing probe for the population function.

We compared the observed production ratio with that calculated from different population functions, as is summarized in Table 5.5. Although the decreasing functions (population is proportional to *a* - *Ex* as well as exp(-*Ex*)) can favorably explain the experimental value, none of the test functions can explain the data correctly. The reason may be because the portion of the direct ^{38}K production is only 1/3 of the total production. The remainder comes from proton emission of excited ^{39}Ca and neutron emission of excited ^{39}K; the population after particle emission is not known. In addition, there may be microscopic structure effects, by which the isomeric state becomes more populated after the collision.

5.5 Reduction of polarization

Before discussing the polarization of fragments, the remaining factor regarding the initial polarization must be summarized. There are three major causes which reduce the initial polarization produced in the projectile-fragmentation process. They are:

Trial function of population	^{38m}K/^{38}K
constant to Ex	1.13
∝ + Ex	1.07
∝ constant - Ex	1.29
∝ exp(- Ex)	1.48
Experimental value	2.7 (5)

Table 5.5 Production ratio of ^{38m}K and ^{38}K.
Ex denotes the excitation energy of the fragment.

	^{37}K	^{39}Ca	^{43}Ti
R_{rem} : Particle emission	>0.15	>0.76	>0.27;Au/0.26;C
R_{rem} : γ rays	~0.82	~0.83	~0.74
R_{rem} : Relaxation	>0.63	>0.72	>0.65
R_{rem} : total	>0.08	>0.45	>0.13

Table 5.6 Remaining factors of the initial polarization for ^{37}K, ^{39}Ca and ^{43}Ti.

(i) Mixing of the fragments fed from the other channels by particle emission. For example, proton emission (^{38}Ca --> ^{37}K + p) of the ^{38}Ca fragments also produces ^{37}K, in addition to the direct production of ^{37}K fragments.

(ii) Degradation of the initial polarization by γ-decay from the excited states to the ground state of the fragment.

(iii) The spin-lattice interaction of implanted nuclei of the projectile fragments in the catcher.

The first two rapid processes were estimated by utilizing the results from other experiments and/or theoretical calculations. The last effect was determined from our own experimental check.

We define the remaining factor of the initial polarization (R_{rem}) by $R_{rem} = P/P_0$, where P_0 is the amount of initial polarization.

(i) Particle emission

The particle-emission processes after the projectile-fragmentation process may reduce the amount of polarization, although the sign of the polarization may remain unchanged during the process. Since no experimental data exist concerning particle emission for the present reaction channels, we estimated the remaining factor using the abrasion-ablation model.

As already described in Section 2.1, according to the abrasion-ablation model, we can calculate the excitation energy as well as the production cross-sections of fragments for any reaction channel. The total production cross-sections should include the production through particle emission from other fragments. It is too difficult to estimate the remaining factor of initial polarization after particle emission, since we don't know the total spin before and after particle emission. However, the minimum remaining factor can easily be deduced if we assumes the non-polarization of the fragments produced by particle emission. Under this assumption, we estimated the minimum remaining factor (R_{rem}) from the portion of direct production in the total cross section. The obtained results are 0.15 for ^{37}K, 0.76 for ^{39}Ca, 0.26 for ^{43}Ti (C target) and 0.27 for ^{43}Ti (Au target), respectively, as shown in Table 5.6. In the case of ^{39}Ca, the electromagnetic dissociation (ED) of ^{40}Ca is included in particle emission. A detailed calculation-method of the ED is shown in Appendix 1-(4).

(ii) γ-decay

The reduction of the initial polarization by γ-decay is estimated as follows.

The substate population after a γ-emission is related to the initial population as,

$$a(m_f) = \sum_{m_i=-J_i}^{J_f} | < J_f\, m_f\, \lambda\, m_i - m_f \mid J_i\, m_i > |^2\, a(m_i)\,, \quad (5.6)$$

where λ is the multipolarity of the γ-decay; suffix i and f represent the quantities of the initial and the final states, respectively. The remaining factor of the initial polarization (R_{rem}) is therefore given as

$$R_{rem} = (-1)^{\lambda - J_i - J_f + 1}\, W(J_i J_i J_f J_f ; 1\, \lambda) \sqrt{\frac{J_i (2J_i + 1)(J_f + 1)(2J_f + 1)}{(J_i + 1) J_f}}\,, \quad (5.7)$$

where $W(J_i J_i J_f J_f ; 1\, \lambda)$ is a Racah coefficient. Using a direct expression for the Racah coefficient, the final form of the remaining factor is given as

$$R_{rem} = \frac{1}{2} \frac{J_i(J_i + 1) + J_f(J_f + 1) - \lambda(\lambda + 1)}{(J_i + 1) J_f}\,. \quad (5.8)$$

The total remaining factor can be calculated using Equation (5.8) for each transitions in a decay chain. Among the nuclei studied (^{37}K, ^{39}Ca and ^{43}Ti), only the excited states of ^{37}K have been well investigated. For the other nuclei (^{39}Ca and ^{43}Ti), the excited states of their mirror parents (^{39}K and ^{43}Sc) were used for the present estimation utilizing the charge symmetry of the nuclear force. Information concerning the population of excited states is also necessary in order to calculate the remaining factor. However, no experimental data is available. We therefore used the following population functions, which are fairly consistent with the result from the abrasion-ablation model:

Population $\propto a - Ex$ ($Ex < 7.5$ MeV) for ^{39}K

Population $\propto + Ex$ ($Ex < 7.5$ MeV) for ^{37}K and ^{43}Sc . (5.9)

Here, a is the constant and Ex is the excitation energy.

Thus the remaining factors, considering the reduction due to γ-decays, are 0.82 for ^{37}K, 0.83 for ^{39}Ca and 0.74 for ^{43}Ti, respectively (Table 5.6).

(iii) Spin-lattice relaxation effects

For ^{37}K and ^{39}Ca, we observed the polarization as a function of time during a counting time of about 4 sec. The spin-lattice relaxation time (T_1) was deduced from the time spectra. Since the observed T_1 has some uncertainty due to the imperfect achievement of AFP, we can know at least the minimum value of the spin-lattice relaxation time. The minimum T_1 was obtained to be 3 sec for both ^{37}K in KBr and ^{39}Ca in CaF_2.

The spin-lattice relaxation time for ^{43}Ti in cooled Pt was estimated as described in Section 4.4.3, instead of using experimental T_1, since the statistical error is too large to deduce T_1. The estimated spin-lattice relaxation time of ^{43}Ti in cooled Pt (T~90K) is larger than 1.3 sec.

The remaining factor due to the spin-lattice relaxation was calculated according to

$$R_{rem} = \frac{\int_0^t P(t)\,Y(t)\,dt}{\int_0^t Y(t)\,dt} = \frac{1}{\tau/T_1+1}\,\frac{1-1/\exp(1+\tau/T_1)}{1-1/e}, \quad (5.10)$$

where $P(t)$ and $Y(t)$ are the polarization and yield as functions of time, respectively; τ is a lifetime of implanted nuclei. The obtained remaining-factors are 0.63 for ^{37}K, 0.72 for ^{39}Ca and 0.65 for ^{43}Ti, respectively, as summarized in Table 5.6.

By multiplying the remaining factors in (i) ~ (iii), the total remaining factors can be obtained (0.08 for ^{37}K, 0.45 for ^{39}Ca and 0.13 for ^{43}Ti), as summarized in Table 5.6. It is noted that the factors indicate the minimum values in terms of the above discussions.

5.6 Polarization of ^{37}K and ^{39}Ca produced through the ^{40}Ca on Au collision

The fragment polarization of ^{37}K and ^{39}Ca produced through the ^{40}Ca on Au collision at 106 MeV/nucleon was observed at production angles of around the classical grazing angle.

The momentum window was ± 0.9 MeV/c/A and ± 1.7 MeV/c/A, for ^{37}K and ^{39}Ca, respectively. The momentum dependence of the fragment polarization was measured at a production angle $\theta = 2.0^o \pm 0.6^o$, as shown in Figure 5.6. The experimental results are also summarized in Table 5.7. Here, the sign of the polarization parallel to $p_i \times p_f$ is defined as being positive, where p_i and p_f are the momentum vectors of incoming and outgoing particles. To extract the polarization, we considered the corrections due to an admixture from other fragments as well as the finite detection angle. The fraction (α) of true β-rays was determined from an analysis of the β-ray time-spectra (typically, α~0.5 in the high-momentum side and α~0.9 in the low-momentum side); the correction factor (η) for the finite detection angle of the β-ray counters was estimated from the geometry of the detection system, while taking into account the trajectories of β-rays in the high magnetic field (H_0~5.2kG) between the catcher and the detectors (η~0.63 for ^{39}Ca and η~0.62 for ^{37}K. The slight difference between ^{39}Ca and ^{37}K results from the differences in the β-ray maximum energies as well as the threshold of the β-ray counters.), as described in Sections 4.2.5 and 4.4.5, respectively. The asymmetry factor ($\mathcal{A}$) was empirically estimated to be +0.83

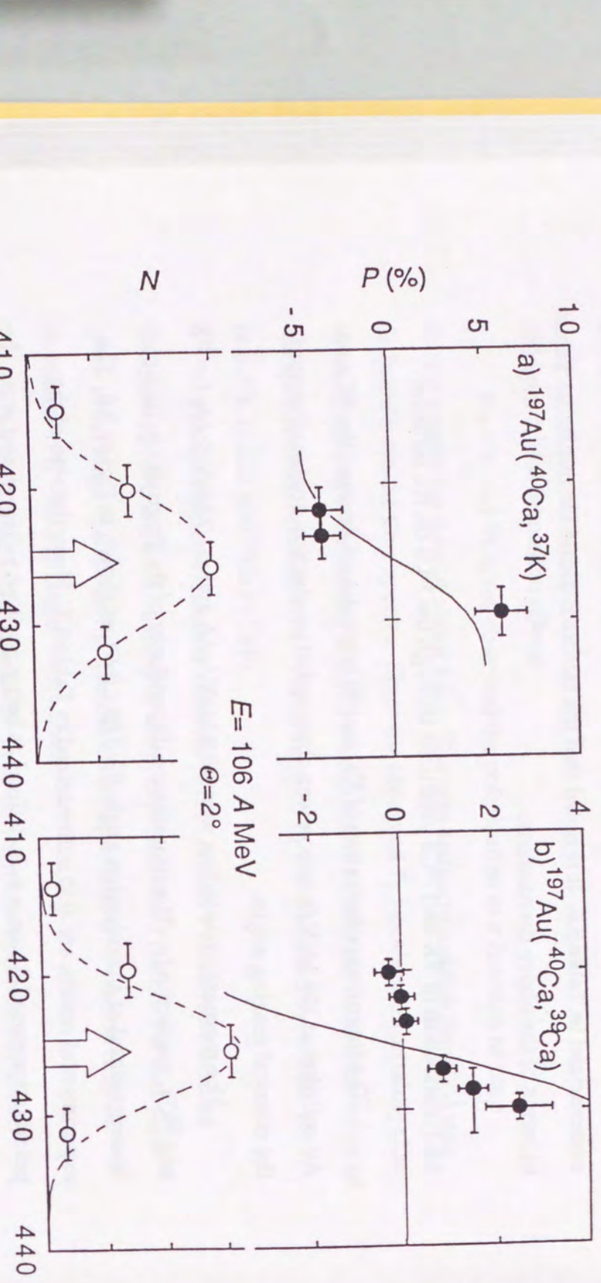

Fig. 5.6 Momentum dependence of the polarization for ^{37}K (left) and ^{39}Ca (right).

The closed circles are polarization. The open circles are the relative yields of the fragments. Horizontal bars show the momentum window. The momentum corresponding to the beam velocity is shown by the arrows. The solid lines represent the calculated polarization by a simple model multiplied by 1/20, and broken lines are the best from Equation (5.1).

Nuclei	Angle	p_f	Effect	αηAP	α	η	A	P
	deg	MeV/c/A	%	%				%
^{39}Ca	2.0(6)	429.9(9)	-4.77(82)	+0.61(11)	0.47(11)	0.63(1)	0.83	+2.48(71)
		427.1(9)	-2.84(102)	+0.36(13)	0.82(7)			+0.84(32)
		423.6(9)	-0.24(97)	+0.03(12)	0.88(9)			+0.07(26)
		421.9(9)	0.03(96)	+0.00(12)	0.89(11)			-0.01(26)
		420.1(9)	+1.01(119)	-0.13(15)	0.89(18)			-0.27(32)
	2.0(6)	429.5(23)	-3.82(58)	+0.49(8)	0.63(9)			+1.49(31)
	1.5(6)		-2.43(71)	+0.31(9)				+0.94(31)
	-1.5(6)		-2.83(69)	-0.36(9)				-1.10(31)
	2.5(6)		-2.65(44)	+0.34(6)				+1.03(23)
^{37}K	2.0(6)	429.5(17)	+8.84(186)	-1.06(0.21)	0.51(7)	0.62(1)	-0.57	+5.89(141)
	2.0(6)	423.7(17)	-8.78(227)	+1.15(31)	0.85(4)			-3.83(106)
	2.0(6)	421.9(17)	-9.15(251)	+1.20(35)	0.87(4)			-3.92(125)
	1.5(6)	421.9(17)	-3.11(219)	+0.39(28)	0.84(9)			-1.33(97)

Table 5.7 Polarization of ^{37}K and ^{39}Ca.

and -0.57 for ^{39}Ca and ^{37}K, respectively, as described in Section 3.1. These corrections are also listed in Table 5.7.

The polarizations of ^{37}K and ^{39}Ca fragments were also measured at other production angles of $\theta = 1.5^{o}$ and 2.5^{o}. The angular window was $\pm 0.6^{o}$. The momenta were set to the low-momentum side (421.7±1.7 MeV/c/A) for ^{37}K and the high-momentum side (429.5±2.3 MeV/c/A) for ^{39}Ca. The results are given in Fig. 5.7, and are summarized in Table 5.7 with the corrections. It was confirmed that in the case of ^{39}Ca the absolute sign of the observed polarization is reversed at the opposite production angle, as shown at the bottom in the figure (by a circle with a dot).

The observed fragment polarization was positive in the higher momentum side of the fragment distribution, and was negative in the lower momentum side, for both ^{37}K and ^{39}Ca. This trend remained unchanged at the other production angles. The observed trend in the momentum dependence of the polarization is the same as that observed for the projectile-like fragments in heavy-ion collisions at much lower energies (~10 MeV/nucleon) around the quasi-elastic peak, where the transfer process is dominant (SU77). The same trend has also recently been reported in the polarization of a projectile-like fragment (^{12}B) produced in ^{14}N + Au collisions at an intermediate energy (40 MeV/nucleon) (AS90). Thus, the fragment polarization around the quasi-elastic peak persistently showed the same trend over a wide range of projectile energies for various projectile masses and numbers of nucleons removed from the projectile.

In order to explain the observed trends regarding fragment polarization, a simple projectile fragmentation model (described in Section 2.4) was applied. This model assumes a participant-spectator mechanism regarding the fragmentation and peripheral natures of the collision. Assuming positive-angle

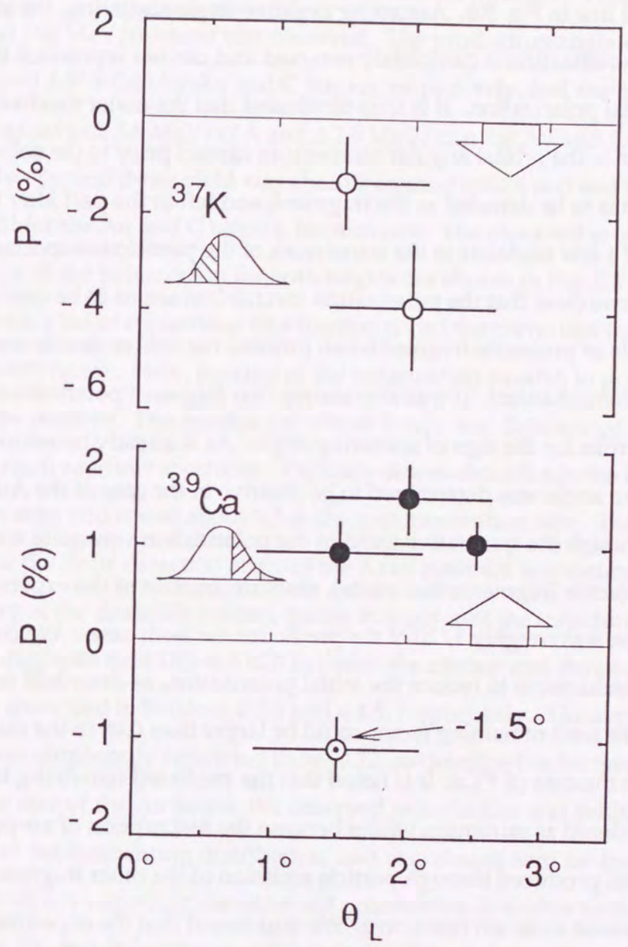

Fig. 5.7 Angular dependence of the polarization for ^{37}K and ^{39}Ca. The arrows show the classical grazing angle for the ^{40}Ca on Au collision.

scattering for the fragments, the observed trend in the momentum dependence of the fragment polarization is qualitatively accounted for by the model, as shown by the solid line in Fig. 5.6. Assuming negative-angle scattering, the sign of predicted polarization is completely reversed and can not reproduce the experimental polarization. It is thus concluded that the major mechanism of the polarization is the orbital angular momentum carried prior to the collision by the part, which is to be detected as the fragment, and left in the part after the sudden abrasion of a few nucleons in the framework of the participant-spectator picture. It also became clear that the polarization mechanism seems to be similar for quasi-elastic or projectile-fragmentation process, regardless details concerning the reaction mechanism. It was also shown that fragment polarization can be an excellent probe for the sign of scattering angle. As is already mentioned, the sign of scattering angle was determined to be positive in the case of the Au target.

Although the qualitative trend in the polarization was quite well by the simple projectile fragmentation model, absolute amount of the experimental polarization was roughly 1/20 of the prediction for both cases. We considered possible mechanisms to reduce the initial polarization, as described in the former section. The total remaining factor could be larger than 0.08 in the case of ^{37}K and 0.45 in the case of ^{39}Ca. It is noted that the predicted remaining factors have to be considered as minimum values because the assumption of no-polarization in the nuclei produced through particle emission of the other fragmentation channels seems to be too restrictive. We thus found that the experimental polarizations are smaller than the predicted values even after corrected depolarization effects. In order to explain the quenching, contribution from the scattering with opposite sign must be mixed in the main scattering component.

5.7 Polarization of ^{43}Ti produced through the ^{46}Ti on Au and C collisions

The polarization of the ^{43}Ti fragment produced through ^{46}Ti on Au and C collisions at 108 MeV/nucleon was observed. The production angle was set to $2.0° \pm 1.1°$ and $1.5° \pm 0.6°$ for Au and C targets, respectively, and the momentum window was set to ± 2.6 MeV/c/A and ± 2.0 MeV/c/A for Au and C targets, respectively. Typical β-ray yield was about 2 counts/spill(4 sec) and 50 counts/spill for the Au and C targets, respectively. The observed momentum dependences of the polarization for both targets are shown in Fig. 5.8 and Table 5.8 along with a list of corrections (the fraction α and the correction factor η) and the asymmetry factor. Here, the sign of the polarization parallel to $p_i \times p_f$ is again defined to be positive. The fraction (α) of true β rays was determined from an analysis of the β-ray-time spectrum. Typically α was about 0.4 in the high-momentum side, and α was about 0.7 in the low-momentum side. The correction factor (η) for the finite detection angle of the β-ray counters was estimated from the geometry of the detection system, taking into account the trajectories of β rays in the high magnetic field (H_0~6.9 kG) between the catcher and the detectors (η~0.58), as described in Sections 4.2.5 and 4.4.5, respectively. The asymmetry factor ($\mathcal{A}$) was empirically estimated to be -0.72, as described in Section 3.1.

In the case of the Au target, the observed polarization was positive for the higher side of the momentum distribution, and was almost zero for the lower side. The tendency regarding the observed polarization is similar to that observed for ^{37}K and ^{39}Ca produced through the ^{40}Ca on Au collision, indicating that the sign of scattering angle is positive. It is shown that the general tendency concerning the fragment polarization is similar to heavy-ion collisions on a heavy target, like Au, regardless of the incident beam or the fragment species.

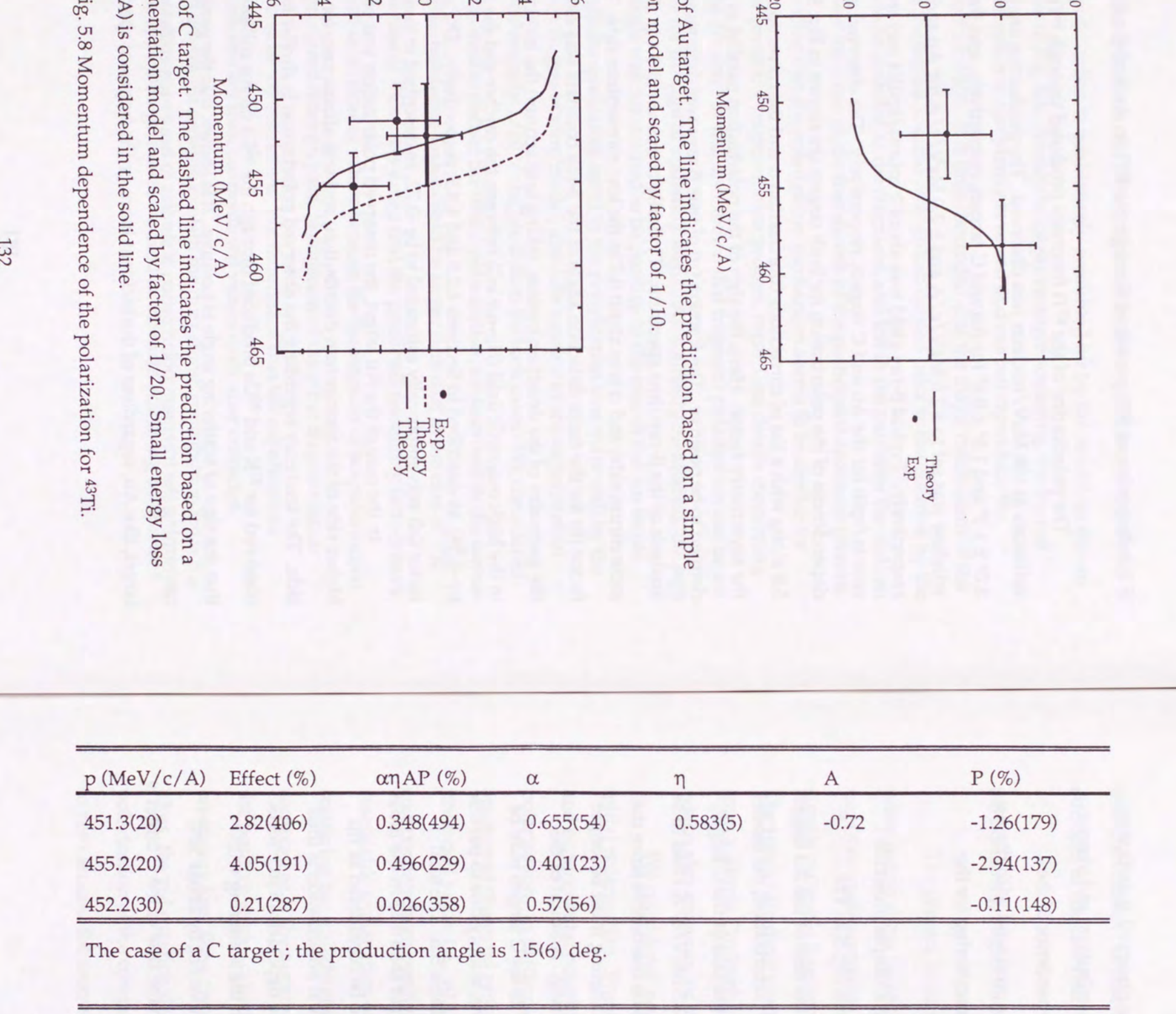

(a) The case of Au target. The line indicates the prediction based on a simple fragmentation model and scaled by factor of 1/10.

(b) The case of C target. The dashed line indicates the prediction based on a simple fragmentation model and scaled by factor of 1/20. Small energy loss (2.5MeV/c/A) is considered in the solid line.

Fig. 5.8 Momentum dependence of the polarization for ^{43}Ti.

p (MeV/c/A)	Effect (%)	αηAP (%)	α	η	A	P (%)
451.3(20)	2.82(406)	0.348(494)	0.655(54)	0.583(5)	-0.72	-1.26(179)
455.2(20)	4.05(191)	0.496(229)	0.401(23)			-2.94(137)
452.2(30)	0.21(287)	0.026(358)	0.57(56)			-0.11(148)

The case of a C target ; the production angle is 1.5(6) deg.

p (MeV/c/A)	Effect (%)	αηAP (%)	α	η	A	P (%)
458.4(26)	-12.0(53)	-1.60(75)	0.392(20)	0.583(5)	-0.72	+9.67(459)
452.0(26)	-3.4(84)	-0.43(109)	0.425(37)			+2.41(607)

The case of an Au target ; the production angle is 2.0(11) deg.

Table 5.8 Polarization of ^{43}Ti.

On the other hand, in the case of the C target, the observed polarization was negative for the center region of the momentum distribution, and almost zero for the lower side. This decreasing momentum dependence of the polarization is in contrast with the cases of ^{37}K and ^{39}Ca produced with the Au target. This reversed tendency suggests negative-angle scattering for the fragment.

The theoretical polarization was calculated using a simple projectile fragmentation model described in Section 2.4 as shown in Fig. 5.8. The theoretical polarization was scaled by factor of 1/10 in the case of the Au target and 1/20 in the case of the C target, respectively. After factorization, the model explained the data well in the case of the Au target. In the case of the C target, the negative-angle scattering and a slight energy-loss (2.5 MeV/c/A) had to be assumed to explain the data. This assumption seems to be reasonable since the contact time for the component of the negative-angle scattering must be longer than that for the component of the positive-angle scattering. Amount of the experimental polarization (~1/10 for Au target and ~1/20 for C target) may be explained by considering the depolarization mechanisms, mainly due to particle emission after excitation by the collisions, as shown in Table 5.6. The total remaining factor of the initial polarization for ^{43}Ti is larger than 0.13 in the table. However, again, the predicted remaining factors have to be considered as the minimum values (see previous section). The experimental polarization is thus smaller than the predicted value even after corrected the depolarization effects. In order to explain the quenching, the contribution from the scattering with opposite sign must be mixed in the main scattering component by about 50% level. One may claim that the amount of polarization in the case of the C target is

less than that in the case of the Au target. This suggests that the mixing is stronger in the case than the case of the Au target.

5.8 Scattering-angles in the projectile-fragmentation process

The present results concerning the momentum dependence of the polarization show positive-angle scattering in the case of a heavy target (Au) and negative-angle scattering in the case of a light target (C) in the framework of a simple projectile fragmentation model based on the participant-spectator picture. The results are quite consistent with the signs of the scattering angle predicted from a simple Coulomb-nuclear field of the target as discussed in Section 5.2, which also accounts for the broadening of the angular distributions.

We considered possible mechanisms that would cause a reduction in the initial polarization. From the quantitative comparison between the theoretical and experimental polarization, we found the quenching of the experimental polarization. In particular, in the case of ^{43}Ti produced with the C target, the amount of observed reduction factor, ~1/20, was clearly smaller than the predicted value; i.e., >0.13 (the minimum remaining factor). The mixing of components from positive- and negative-angle scattering can be the most reasonable explanation of the discrepancy. The component of the negative-angle scattering has a slight energy-loss, which is explained by the contact time in the component of the negative-angle scattering longer than that in the component of the positive-angle scattering. If the component of positive-angle scattering has no-energy loss, these two components mix around the optimum momentum. Thus, the polarization decreases around the optimum momentum, since the polarization of the component of positive-angle scattering is expected to be close to zero around the momentum. On the other hand, the shift of the momentum

distribution is smaller than the shift of the zero crossing point in the polarization, and may not be detected in the present momentum distribution. This picture is consistent with the prediction based on the microscopic simulation method described in Section 2.4.

In particular, in the case of ^{39}Ca, the amount of observed reduction factor, ~1/20, was much smaller than the prediction with the depolarization correction (>0.45; from the minimum remaining factor). Furthermore, in this case, the amount of polarization in the lower momentum side (~0) is smaller than that observed in the higher momentum side (~1/20), as shown in Fig. 5.6. A simple mixing of the components of both signs can not explain the asymmetry. An unexpectedly large contribution of the other polarization mechanisms, such as frictional force which was important for the polarization phenomena in deep inelastic collisions at low energies of around 10 MeV/nucleon, may play an important role in the present asymmetry.

The results concerning the signs of the scattering angle in the present study strongly support the idea of orbital deflection originally introduced by Bibber et al. (BI79). The present conclusion conflicts with the conclusion reported by Wong et al. (WO82) and Silk et al. (SI88), who claimed positive-angle scattering for both heavy and light targets by considering the Coulomb final-state interaction and the final-state interaction, respectively.

Wong et al. claimed that negative-angle scattering for light targets can not reproduce the Z_F (the atomic number of the fragment) dependence of the angular width. However, it might be possible that the components from the negative- and positive-angle scattering are mixed due to various reasons, and that the component of positive-angle scattering determines the total Z_F dependence of the width. Thus, the theoretical prediction of the Z_F dependence according to the

Coulomb final-state interaction must be improved so that it can be applied also to such a mixed case.

The measurements of Wong et al. and Silk et al. had less sensitivity for determining the sign of the scattering angle than our measurements and were rough since they didn't observe the main component ($\theta \sim 0^o$). Their assumption was also rough since they neglected the contribution of the participant come from the target nucleus. Thus, they might be led to the wrong conclusion. However, it is noted that the production-angles in their experiments ($2^o < \theta < 8^o$) are different from those in our experiments ($\theta \sim 2^o$ for Au target and $\theta = 1.5^o$ for C target). Therefore, the conflicting situation regarding the sign of the scattering angle may suggest the angular dependence of the sign. For a conclusive discussion, precise measurements of the angular distributions in the region $\theta < 2^o$, and the fragment polarization in the region $\theta > 2^o$ are necessary at the present energy.

Chapter 6. Future prospects:

Measurement of the magnetic moment of the ^{43}Ti

(a) Experimental magnetic moment

As a first step to extend our study, the present technique used to polarize radioactive nuclear beams was applied to a study of the magnetic moments for $f_{7/2}$ shell mirror nuclei. In the application, we observed the NMR on the ^{43}Ti fragments produced through the ^{46}Ti on Au and C collisions.

For the Au target the production angle was set to 2.0 ± 1.1°; the momentum window was set to the higher momentum side (458.4 ± 2.6 MeV/c/A). For the C target the production angle was set to 1.5 ± 0.6°; the momentum window was set to the optimum in the momentum distribution (455.2 ± 2.0 MeV/c/A). For both cases, the static magnetic field was set to H_0=6.87 kG and a Pt catcher, which was cooled down the liquid-nitrogen temperature (T~90K), was used.

The observed NMR spectra for the cases of Au and C targets are shown in Figures 6.1 and 6.2, respectively. For the case of the Au target, it was not sufficient to determine the magnetic moment of ^{43}Ti because of poor statistics. For the C target, in order to determine the magnetic moment, we summed the wide and narrow frequency modulation, as shown in Fig. 6.3. A bump can be seen in the high-frequency region in the spectrum. From the resonance frequency (f=(1.27 ± 0.03) MHz) the magnetic moment of ^{43}Ti was determined as follows:

$$|\mu| = 0.85\ (2)\ \text{nm}\ . \qquad (6.1)$$

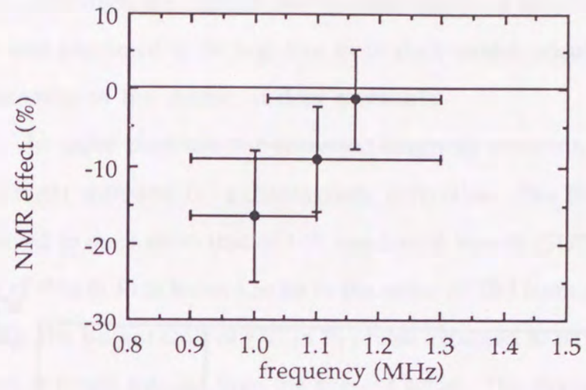

Fig. 6.1 Observed NMR spectrum of ^{43}Ti in the case of Au target.

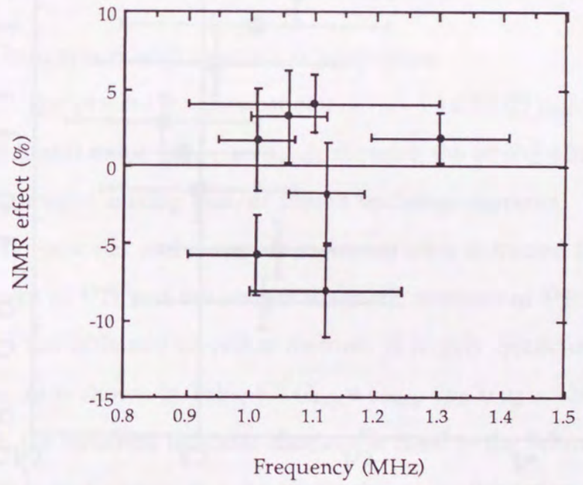

Fig. 6.2 Observed NMR spectrum of ^{43}Ti in the case of C target(wide and narrow frequency modulation.).

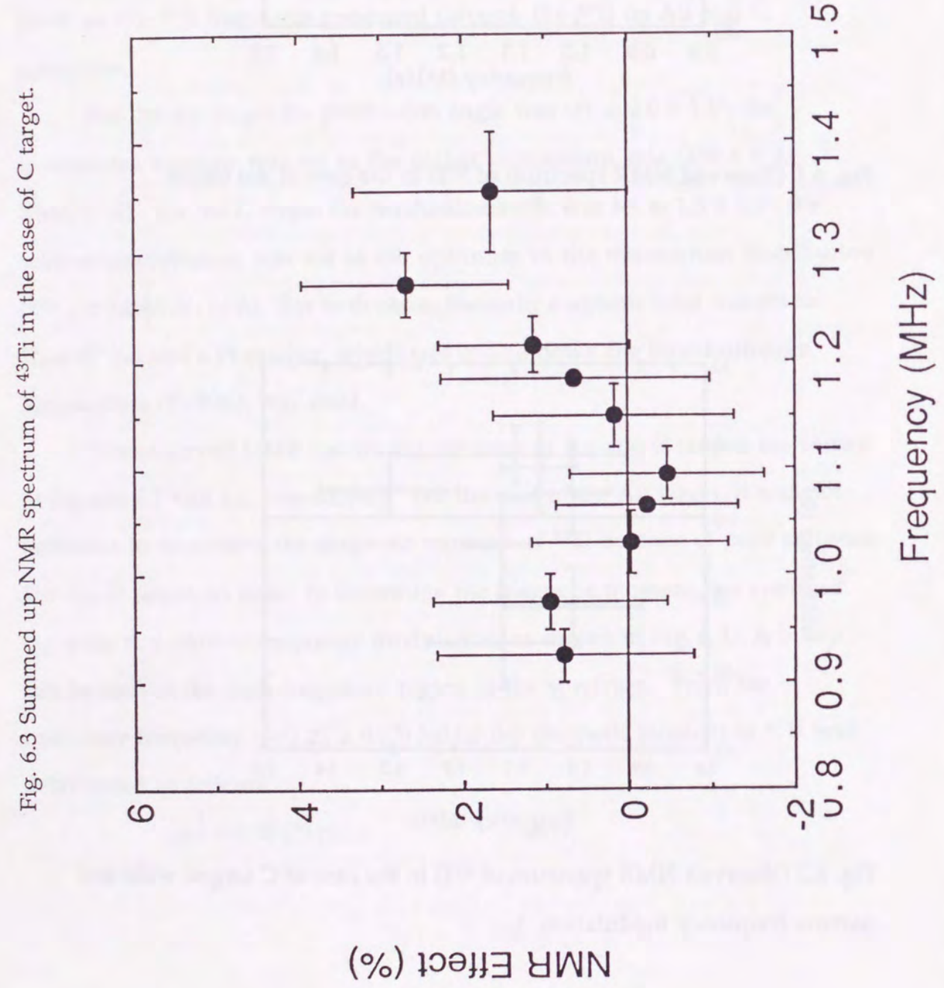

Fig. 6.3 Summed up NMR spectrum of ^{43}Ti in the case of C target.

Although the sign of the magnetic moment was not determined, the sign was predicted to be negative from shell-model calculations as well as the systematics of the mirror nuclear moments.

In order to obtain the corrected magnetic moment, we must consider (i) the Knight shift and (ii) a diamagnetic correction. The Knight shift is expected to be close to that of ^{41}Sc implanted into Pt (SU73). Since the Knight shift of ^{41}Sc in Pt is known to be in the order of 10^{-4} from a recent study (MI90), the Knight shift of ^{43}Ti in Pt is also expected to be of the order of 10^{-4}, which is much smaller than the present error. The diamagnetic correction was found to be $\sigma = + 1.66 \times 10^{-3}$ from theoretical calculations which included the relativistic effects (JO83), assuming the charge state Ti^{4+}. This is also negligibly small compared with the error in the present magnetic moment. We therefore adopt the value in Equation (6.1) as the magnetic moment of ^{43}Ti.

(b) Comparison with theoretical predictions

The present magnetic moment (μ = (-) 0.85 (2) μ_N) greatly deviates from the Schmidt value (μ_S = -1.91 μ_N), showing the strong effects due to configuration mixing and/or meson exchange currents. To see it more clearly, isoscalar and isovector moments were extracted from the present moment of ^{43}Ti and the known magnetic moment of ^{43}Sc (Table 6.1).

The obtained isovector moment is largely quenched from the Schmidt value, as is shown in Table 6.2 ($\delta_{exp} \equiv (\mu_{exp} - \mu_S)/\mu_S \sim$ - 30 %). On the other hand, the obtained isoscalar moment is close to the Schmidt value ($\delta_{exp} \sim$ - 3 %). It is thus shown that the effects due to configuration mixing and/or meson exchange currents are of the isovector type.

A	Nuclei		I^{π}	μ_s (nm)	μ_{exp} (nm)
39	^{39}K		$3/2^+$	+ 0.124	+ 0.392 [1]
	^{39}Ca		$3/2^+$	+ 1.148	(+) 1.022 [1]
		$2\mu^{(0)}$		+ 1.272	+ 1.414
		$2\mu^{(1)}$		- 1.024	- 0.630
41	^{41}Sc		$7/2^-$	+ 5.793	(+) 5.431 [2]
	^{41}Ca		$7/2^-$	- 1.913	- 1.595 [1]
		$2\mu^{(0)}$		+ 3.880	+ 3.836
		$2\mu^{(1)}$		+ 7.706	+ 7.026
43	^{43}Sc		$7/2^-$	+ 5.793	+ 4.62 (4) [1]
	^{43}Ti		$7/2^-$	- 1.913	(-) 0.85 (2) [3]
		$2\mu^{(0)}$		+ 3.880	+ 3.77 (5)
		$2\mu^{(1)}$		+ 7.706	+ 5.47 (5)

1) ; (RA89) 2) ; (MI90) 3) ; Present result

$2\mu^{(0)} \equiv \mu_{(p\text{-}odd)} + \mu_{(n\text{-}odd)}$

$2\mu^{(1)} \equiv \mu_{(p\text{-}odd)} - \mu_{(n\text{-}odd)}$

Table 6.1 Magnetic moments of A=39, 41, 43 mirror nuclei.
$\mu^{(0)}$ and $\mu^{(1)}$ are the isoscalar moment and the isovector moment, respectively. μ_s and μ_{exp} denote the Schmidt value and the experimental value, respectively.

For more precise discussions, we introduce the correction from first-order configuration-mixing. The results are summarized in Table 6.2, where the calculations by Ogawa et al. and Richter et al. (see Appendix 2.6) are used. The quenching in the isovector moment can be well explained by first-order configuration-mixing ($\delta_{1'stc.m.} \sim$ - 30 %). This suggests that the amount of the

Isoscalar moment ($\equiv \mu_{(p\text{-}odd)} + \mu_{(n\text{-}odd)}$)

A	Schmidt (nm)	Model	δ:1'stc.m. (%)	δ:2'nd.c.m. (%)	δ:ex (%)	δ:Total. (%)	δ:Exp. (%)	Δ (%)
39	+ 1.272	IBA	—	+ 12.5	+ 3.0	+ 15.5	+ 11.2	+ 4.3
		T.K.	—	+ 9.9	-1.1	+ 8.8		- 2.4
41	+ 3.880	IBA	—	+ 2.9	-2.7	+ 0.2	- 1.1	+ 1.3
		T.K.	—	+ 0.3	-1.9	- 1.6		- 0.5
43	+ 3.880	OG	+ 0.9	?	?	+ 0.9	- 2.8(10)	+3.7(10)
		RI	+ 0.7	?	?	+ 0.7		+3.5(10)
		RI_{eff}	—	—	—	- 3.2		-0.4(10)

Isovector moment ($\equiv \mu_{(p\text{-}odd)} - \mu_{(n\text{-}odd)}$)

A	Schmidt (nm)	Model	δ:1'stc.m. (%)	δ:2'nd.c.m. (%)	δ:ex (%)	δ:Total. (%)	δ:Exp. (%)	Δ (%)
39	- 1.024	IBA	—	+ 42.2	- 48.3	- 6.1	- 38.5	+ 32.4
		T.K.	—	+ 40.8	- 64.8	- 24.0		+ 14.5
41	+ 7.706	IBA	—	- 23.1	+ 19.9	- 3.2	- 8.8	+ 5.6
		T.K.	—	- 20.8	+ 19.8	- 1.0		+ 7.8
43	+ 7.706	OG	- 29.7	?	?	- 29.7	-29.0(5)	-0.7(5)
		RI	- 32.7	?	?	- 32.7		-3.7(5)
		RI_{eff}	—	—	—	- 29.6		-0.6(5)

$\delta = (\mu - \mu_s) / \mu_s$ $\Delta \equiv$ (Total - Exp.)

IBA ; (AR88), TK ; (TO83), OG ; (OG89), RI ; (RI91)

Table 6.2 Theoretical and experimental magnetic moments of mirror pairs in A = 39, 41 and 43 systems.

second-order configuration-mixing and the meson exchange currents must be completely canceled in the isovector moment, similar to the case of the A=41 system ($\delta_{2'ndc.m.} \sim -20$ % and $\delta_{ex} \sim +20$ % in the A=41 system, as shown in Table 6.2).

On the other hand, in the isoscalar moment of the A=43 system, we found a small, but non-negligible, deviation (Δ) between the experimental value and a prediction which included first-order configuration-mixing ($\Delta \equiv (\delta_{Theory} - \delta_{exp}) \sim +3$ %). For the isoscalar moment in the A=39 and 41 systems, by considering second-order configuration-mixing and meson exchange currents, the deviation between the experimental and Schmidt values could be accounted for quantitatively, as shown in the Table 6.1. Thus, the deviation of the isoscalar moment in the A=43 system ($\Delta \sim +3$ %) suggests the importance of second-order configuration mixing and/or meson exchange currents in the isoscalar moment.

For a conclusive discussions which include the interesting quark-deconfinement effect (MI90), precise measurements and calculations of the magnetic moments in the A=43 system are necessary.

Chapter 7. Conclusion

106 MeV/nucleon ^{40}Ca beam and 108 Mev/nucleon ^{46}Ti beam were used to bombard Au and C targets. The spin polarization as well as the momentum and angular distributions of the projectile fragments (^{37}K, ^{39}Ca and ^{43}Ti) were measured at forward angles ($\theta \sim 2^{o}$). From measurements of the momentum distributions, it was confirmed that the participant-spectator picture is effective for the prediction of the observed widths in the distributions. The widths reflect the Fermi motion of the nucleons inside the nucleus (the Goldhaber model). The observed widths of the angular distributions, however, were broader than those predicted from the Goldhaber model. This broadening was the unsolved problem for the study of the reaction mechanism in the present energy region. The broadening of the widths strongly suggests the importance of the interaction between colliding nuclei and/or that between the participant and the spectator fragment. Since the conventional measurements such as the angular distribution had the limit for the further investigation of the mechanism, we introduced a new observable; i.e., the spin polarization which is expected to probe the sign of the scattering angle.

The observed trend in the momentum dependence of the fragment polarization was qualitatively accounted for by a simple fragmentation model based on the participant-spectator picture assuming either positive- or negative-angle scattering. So, it was found that the major polarization mechanism is the orbital angular momentum left in the spectator fragment by the sudden disappearance of the nucleons. It was also shown that the fragment polarization is an excellent probe for the sign of the scattering angle.

From the precise measurement of the polarization, the sign was determined to be positive in the case of the Au target and negative in the case of the C target. So, it is concluded that the positive-angle scattering by the relatively strong Coulomb potential is the main component for the case of the Au target and the negative-angle scattering by the nuclear attractive potential is the main component for the case of the C target, where the Coulomb potential is negligibly small. For the quantitative comparison between the measured angular distributions and the theoretical ones, orbital deflection due to the simple combined Coulomb-nuclear field of the target was calculated. As a result, the combined Coulomb-nuclear field almost accounted for the experimental broadening of the angular distributions.

By considering possible mechanisms for reducing the initial polarization up to the maximum, reduction of the amount of polarization may be explained in the case of the Au target at the first glance. However, it is noted that the predicted remaining factors have to be treated as minimum values because the assumption of no-polarization for the nuclei produced through particle emission from other fragment channels seems to be too restrictive. We thus found the quenching of the fragment polarization. In order to explain the quenching, contribution from the scattering with opposite sign must be mixed in the main scattering component. In the case of the C target, the mixing is stronger than the case of the Au target.

For the light target, the present conclusion; i.e., the negative-angle scattering by the nuclear potential, disagrees with the conclusions reported by other authors given based on an analysis of the angular distribution using Coulomb final-state interaction. In their discussion, the extrapolation from the large-angle component ($2^o < \theta < 8^o$) in the angular distribution was too

rough for determining the sign of the scattering angle. For the conclusive discussion, it is also necessary to consider the mixing of the components from the positive- and negative-angle scattering even in their case.

As an application of fragment polarization, we have measured the magnetic moment of ^{43}Ti. The preliminary result shows the strong effects due to configuration mixing and/or meson exchange currents. We discussed the isoscalar and isovector moment for the A=43 mirror pair in terms of this measurement. In the isoscalar moment, the observed value is close to the Schmidt value, but slightly deviates from the value determined by a shell-model calculation which included first-order configuration-mixing. Further, in the isovector moment the observed value is found to be greatly deviated from the Schmidt value, but well reproduced by the shell-model calculation. It is therefore suggested that the second-order configuration-mixing and the meson exchange currents play important roles in the isoscalar moment for the A=43 system.

Appendix 1. Atomic and nuclear interactions of high-energy heavy-ions with matter.

(1) Energy-loss and range

When a heavy ion passes through matter, it collides with atoms in matter so many times and that it loses energy. This energy loss is given by Bethe's formula (AH80):

$$-\frac{dE}{dx} = \frac{4\pi N Z_1^2 e^4 Z_2}{m_e c^2 \beta_c^2}\left[\ln\left\{\frac{2 m_e c^2 \beta_c^2}{I(1-\beta_c^2)}\right\} - \beta_c^2 - \frac{C}{Z_2} - \frac{\delta}{2} + M - B_{nr} + B_{rc}\right] J . \qquad (A.1.1)$$

Here, M is the Mott term, which accounts for the finite size of the charge distribution; B_{nr} and B_{rc} are Bloch terms used to properly describe electron binding in close-collision events, $\delta/2$ denotes the density effect, J denotes the low-velocity Barkas effect, C/Z_2 denotes the inner-shell corrections, Z_1 and Z_2 are the nuclear charges of passing ions and atoms in the material, respectively. Further, e and m_e are the charge and mass of the electron respectively, β_c is the velocity of the ion, N is the number of atoms per unit volume, and I is the mean ionization energy of the atoms in the material. This formula can be approximated by Equation (4.16), since the value in the square brackets is not very large.

Using the stopping power, the range for an ion having a kinetic energy of E_i is given by

$$R(E_i) = \int_{Ei}^{0} \frac{1}{dE/dx(E)}\, dE . \qquad (A.1.2)$$

Since this range formula is very complicated, the next approximation is helpful in calculation in some cases (DU86):

$$R = k\frac{A}{Z^2}E\gamma + C\,A\,. \qquad \text{(A.1.3)}$$

Here, k, γ and C are constants which depend only on the stopping material, and the unit of E is energy per nucleon. From this equation, Equation (4.5) can be easily deduced.

(2) Multiple scattering

Collisions with stopping materials can cause a broadening of the angular divergence of fragments. This is known as multiple scattering. Several theoretical studies are available for high-energy ions. We used a much simpler formula to estimate the multiple scattering of the ions (PA84):

$$\sigma(\theta) = \frac{14.1\ (\mathrm{MeV/c})}{\sqrt{p_i\,\beta_i\,p_f\,\beta_f}}\,Z_1\sqrt{d/L_r}\left[\,1+\frac{1}{9}\log\frac{d}{L_r}\right], \qquad \text{(A.1.4)}$$

where d/L_r is the thickness (in radiation lengths) of the scattering medium.

This formula gives the standard deviation of the intensity per solid angle in terms of the radiation length (L_r). p_i and p_f are the momenta and β_i and β_f the velocities of the ion before and after a degrader.

For a homogeneous monoatomic medium ($Z > 5$) the radiation length is given by

$$\frac{1}{L_r} = \frac{Z^2}{716.405\,A}\times$$
$$\left\{\ln\left(\frac{184.15}{Z^{1/3}}\right)+\frac{1}{Z}\ln\left(\frac{1194}{Z^{2/3}}\right)-1.202\,\alpha^2Z^2+1.0369\,\alpha^4Z^4-\frac{1.008\,\alpha^4Z^6}{1+\alpha^2Z^2}\right\}, \qquad \text{(A.1.5)}$$

where Z and A are the atomic number and weight of the medium and α is the fine-structure constant.

(3) Charge-state distributions

Generally, targets or degraders are sufficiently thick to ensure charge-state equilibrium. It can be desirable to know the charge-state distributions of

heavy ions after passing through the material. The cross sections for the loss and the capture of electrons are generally difficult to calculate, though the some empirical formula and experimental data are available. Empirically, the hydrogen-like atom is dominant at

$$v \sim v_0\,Z., \qquad \text{(A.1.6)}$$

where v_0 is the Bohr velocity ($= c/137$) and Z is the atomic number of the passing nuclei (SP81). Experimentally, for the case of Ar ions, fully stripped ions are dominant above 30 MeV/nucleon, and hydrogen-like is dominant around 12 MeV/nucleon (SH86).

(4) Electromagnetic dissociation

In the high-energy region, dissociation by the electromagnetic force can not be ignored. The cross section (σ_{ED}) of the electromagnetic dissociation (ED) of heavy ions is given by (BE75)

$$\sigma_{ED} = \int_0^\infty N_\gamma(E)\,\sigma_{GDR}(E)\,\mathrm{d}E\,, \qquad \text{(A.1.7)}$$

where $N_\gamma(E)$ is the virtual photon spectrum and $\sigma_{GDR}(E)$ is the cross section for the giant dipole resonance. $\sigma_{GDR}(E)$ can be approximated as a Lorentian, and is given by

$$\sigma_{GDR}(E) = \frac{\sigma_m}{1+(E^2-E_m^2)^2/(E^2\,\Gamma^2)}\,. \qquad \text{(A.1.8)}$$

The value of σ_m is given by

$$\int_0^\infty \sigma_{GDR}(E)\,\mathrm{d}E = \frac{\pi}{2}\,\sigma_m\,\Gamma = 60\frac{N_p\,Z_p}{A_p}\ (\mathrm{MeV\ mb})\,. \qquad \text{(A.1.9)}$$

The droplet-model prediction of the mean resonance energy (E_m) is

$$E_m = 167.23\,A_p^{-1/3}\,(1.959 + 14.074\,A_p^{-1/3})^{-1/2}\ \mathrm{MeV}\,. \qquad \text{(A.1.10)}$$

(For the case of ^{40}Ca, $\sigma_{GDR}(E)$ has been measured within a finite energy (VE74). We therefore used experimental values as σ_m, Γ and E_m in this case.)

For light projectiles and targets, the fragmentation process dominates the total cross section, and electromagnetic dissociation may be neglected. For heavy projectiles and targets, however, σ_{EMD} becomes of the same order of magnitude as the nuclear reaction cross sections.

Appendix 2. Nuclear magnetic moment

Studying magnetic moments is one of the oldest fields in nuclear physics, and is still a challenging field. The magnetic moment is not only the most strict testing probe for nuclear-structure models, but is also a probe for non-nucleonic degrees of freedom. The magnetic moments of, especially, light mirror nuclei have been vigorously studied, due to their simple nuclear structure. The magnetic moments of almost all nuclei in mirror nuclei below A=41 are presently known and have been studied theoretically in a non-relativistic framework.

Relativistic and quark models have recently been vigorously studied. It is now important to calculate the magnetic moments in terms of these new nuclear models. Such attempts must be referred to. Calculations of the magnetic moment of ^{43}Ti, which is a major object of this thesis, are also described in this section.

A.2.1 General formula of nuclear magnetic moment

The nuclear magnetic moment is defined as the expectation value of a magnetic moment operator (μ) for the state of the maximum z-projection, i.e.,

$$\mu = < \Phi_J \mid \mu \mid \Phi_J > . \qquad \text{(A.2.1)}$$

In this equation, μ is the operator of the magnetic moment and Φ_J is the wave function of the nucleus for the m=j state. We can also write μ as

$$\mu = g\, \mu_0\, I\,, \qquad \text{(A.2.2)}$$

where μ_0 is the nuclear magneton and I is the nuclear spin. We call the g in this equation the g-factor of the nucleus.

A.2.2 Single particle model

From the stand-point of the shell model, the operator of the magnetic moment is given by

$$\mu = \mu_0 \sum_{i=1}^{A} (g_l^i \, l_i + g_s^i \, s_i) \ , \qquad \text{(A.2.3)}$$

where l_i and s_i are the operator of the orbital angular momentum and the intrinsic spin respectively; g_l and g_s are the orbital and spin g-factors. For a free nucleon, these g-factors have the following values:

$$g_l^p = 1.0 \qquad g_l^n = 0.0 \qquad \text{(A.2.4.a)}$$

$$g_s^p = 5.585 \qquad g_s^n = -3.826 \ . \qquad \text{(A.2.4.b)}$$

To extract the magnetic moments from Equation (A.2.1), we need wave functions of the nucleus. In the non-relativistic framework, they are obtained by solving the following Schrödinger equation:

$$\mathcal{H} \, \Phi_I = E \, \Phi_I \ , \qquad \text{(A.2.5)}$$

$$\text{where } \mathcal{H} = \sum_{i>j} (\frac{1}{2} \nabla_i^2 + V(r)_{ij}) \ .$$

Here, $V_{ij}(r)$ is the two-body nuclear potential. Since the two-body nuclear potential is not well understood, it is very difficult to solve this equation without any assumptions and/or approximations. The two-body nuclear potential is thus usually replaced by a one-body average potential. If we adopt the Woods-Saxon potential as the one-body nuclear potential, we can solve Equation (A.2.5) mathematically. We can thus obtain nucleus wave functions.

In the simplest form of the shell model, the single-particle model, the nuclear spin is supposed to be determined according to the angular momentum (I) and the intrinsic spin (s) of the last odd nucleon,

$$I = j = l + s \ . \qquad \text{(A.2.6)}$$

Based on this assumption, Equation (A.2.3) can be rewritten simply as

$$\mu_{sp} = (g_l J + (g_s - g_l) s) \mu_0 \ . \qquad \text{(A.2.7)}$$

We can obtain the value of the magnetic moment by substituting Equation (A.2.7) for μ in Equation (A.2.1) as follows:

$$\mu_{sp} = j (g_l \pm \frac{g_s - g_l}{2 l + 1}) \mu_0 \quad \text{for } j = l \pm 1/2 \ . \qquad \text{(A.2.8)}$$

When we use the free nucleon values of g_l and g_s, as shown in Equation (A.2.4), μ_{sp} in Equation (A.2.8) gives the Schmidt line corresponding to $j=l+1/2$ or $j=l-1/2$. It can be seen from Fig. A.2.1 that almost all of the nuclear magnetic moments that have already been measured are distributed within Schmidt lines. We therefore agree that the single particle model works well as a 0th order approximation.

A.2.3 First-order configuration-mixing

From Fig. A.2.1, it can be seen that there are significant discrepancies between the experimental values and the Schmidt values. The reason for these discrepancies, which we first point out, is that the one-body nuclear potential can not completely describe the actual nucleus. We therefore introduce the residual interaction as a perturbation to the one-body nuclear potential, as shown in the following Hamiltonian:

$$\mathcal{H} = \mathcal{H}_{core} + \mathcal{H}_{sp} + V \ . \qquad \text{(A.2.9)}$$

Here, $\mathcal{H}_{sp}$ is the single-particle potential and V is the residual interaction. Further, the wave function of the nucleus can be written as a linear combination of the basis vectors ϕ_a,

$$\Phi_I = \sum_a c_a \, \phi_a \ , \qquad \text{(A.2.10)}$$

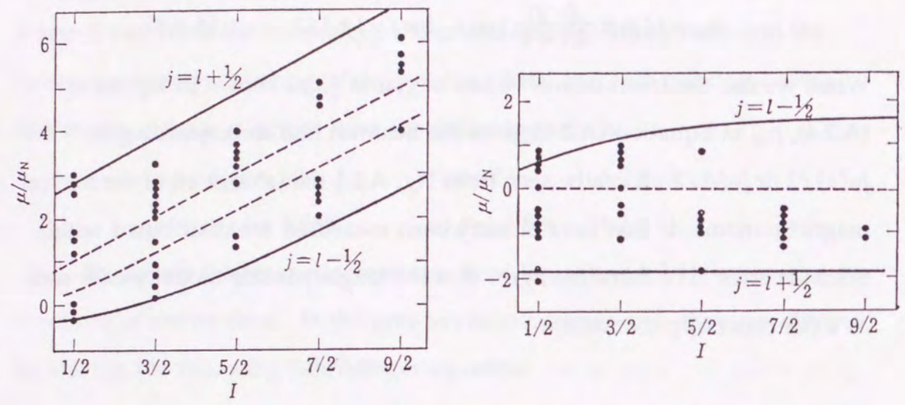

Fig. A.2.1 Magnetic moments of odd-proton nuclei (left) and odd-neutron nuclei (right). Solid lines are the Schmidt values and the dashed line is value for Dirac nucleons.

where c_a indicates the amplitude for each basis vector.

Substituting Equations (A.2.9) and (A.2.10) for Φ_I and $\mathcal{H}$ in Equations (A.2.5), we obtain

$$\sum_a < \phi_a \mid V \mid \phi_a > c_a^2 = (E_b - \varepsilon_{sp}) c_b^2 \quad , \qquad \text{(A.2.11)}$$

where E_b is the remaining value after reducing the energy of the core from the total unit energy (E); ε_{sp} is the single-particle energy. After diagonalizing the matrix $<\phi \mid V \mid \phi>$, we obtain the energy eigenvalues (E_b-ε_{sp}) and amplitudes (c_b's) of the wave functions.

There are two ways to determine the wave function and energy eigenvalues:

(i) To give the residual interaction (V) and the single-particle energies (ε_{sp}).

(ii) To give the parameters in V by χ^2 fitting to the actual energy levels as energy eigenvalues (E_b - ε_{sp}). (The residual interaction determined by this method is called the "effective residual interaction".)

Using the wave functions given by either (i) or (ii), we can calculate the magnetic moments. The operator of the magnetic moment in Equation (A.2.3) may be changed to

$$\mu = \mu_0 \sum_{i=A_c+1}^{A} (g_l^i \, l_i + g_s^i \, s_i) \quad , \qquad \text{(A.2.12)}$$

where the core is filled up with A_c nucleons. Equation (A.2.12) shows that only the nucleons out of the core contribute to the magnetic moment. The effective g-factors (g_l and g_s) can have different values for different orbitals. In order to obtain good visibility, we assume that the g-factors have the same values for different orbitals. The moment operator can thus be written as

$$\mu = \mu_0 \sum_{i=A_c+1}^{A} (g_l \, l_i + g_s \, s_i) \quad . \qquad \text{(A.2.13)}$$

By considering first-order configuration-mixing, Brown et al. could calculate the magnetic moments of the sd-shell mirror nuclei (BR83). Similar calculations have also been performed for p-shell (CO65). The predictions and the experimental moments are shown in Fig. A.2.2. In this figure, the full line indicates the calculated values from Equation (A.2.8). It is shown that agreement between the experimental and calculated values can be improved by considering of the first-order configuration mixing.

A.2.4 Exchange currents and core polarization

It is shown in the previous section that the experimental magnetic moments can be reproduced rather well by considering the first-order configuration-mixing. However, there still remain discrepancies between the calculated and experimental values. In particular, the discrepancies for A=17 and A=39 nuclei, which are the first and last nuclei in the sd-shell, are not explained at all. These discrepancies indicate that other corrections beyond the first-order configuration-mixing are necessary. Until now, it has been found that these discrepancies can be explained dramatically by second-order configuration-mixing, the meson exchange currents which include Δ isobar effects and the cross term between them (TO83) (AR88).

Considering the exchange currents, we must change the operator of the magnetic moment to

$$\mu = \mu_{free} + \mu_{ex} , \qquad \text{(A.2.14)}$$

where μ_{free} is the operator previously defined in Equation (A.2.3), and μ_{ex} is the contribution from newly introduced exchange currents. The exchange current contribution (μ_{ex})can be written as

$$\mu_{ex} = \mu_{int} + \mu_{Sach} , \qquad \text{(A.2.15)}$$

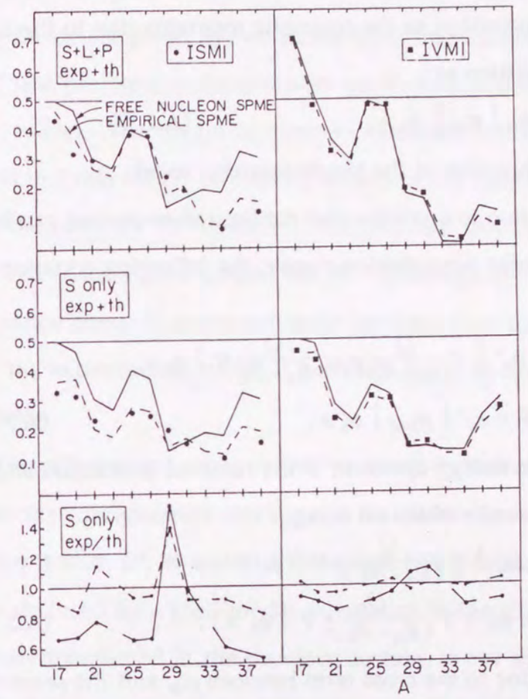

Fig. A.2.2 Comparison of normalized experimental values of the isoscalar and isovector magnetic moments (ISM1 and IVM1, respectively) for the mirror ground states of A = 17 - 39 nuclei with predictions of mixed-configuration sd-shell model wave functions. The solid lines are obtained with single-particle matrix elements set to the free-nucleon values, while the dashed lines are obtained with single-particle matrix elements set to the "final-fit" values of the present study. (BR83)

where μ_{Sach} is the contribution from two-body exchange currents and μ_{int} is the intrinsic part. μ_{Sach} can be written as

$$\mu_{Sach} = M [R \times j_{ex} (q = 0)] , \qquad \text{(A.2.16)}$$

where R is the distance between two nucleons and M is the nucleon mass. We thus obtain the correction to the magnetic moments due to the meson effect, which can be written as

$$\delta\mu_{ex} = < \phi_n \mid \mu_{ex} \mid \phi_n > . \qquad \text{(A.2.17)}$$

Here, ϕ_n is the wave function of the single-particle model.

The correction due to second-order configuration-mixing can be obtained by second-order perturbation-theory; the following equation has been obtained:

$$\delta\mu_{cm} = < \phi_n' \mid V \frac{Q}{E_n - \mathcal{H}_0} \mu_{free} \frac{Q}{E_n - \mathcal{H}_0} V \mid \phi_n >$$
$$- \beta^2 < \phi_n' \mid \mu_{free} \mid \phi_n > , \qquad \text{(A.2.18)}$$

where $\mathcal{H}_0$ is the kinetic energy operator, V the residual interaction and Q the objection operator. β can be obtained using

$$\beta^2 = \frac{1}{2} \{ < \phi_n' \mid V \frac{Q}{(E_n - \mathcal{H}_0)^2} V \mid \phi_n' >$$
$$+ < \phi_n \mid V \frac{Q}{(E_n - \mathcal{H}_0)^2} V \mid \phi_n > \} . \qquad \text{(A.2.19)}$$

The correction due to the cross term between μ_{ex} and the second-order configuration-mixing is given by

$$\delta\mu_{cr} = < \phi_n' \mid \mu_{ex} \frac{Q}{(E_n - \mathcal{H}_0)^2} V \mid \phi_n >$$
$$+ < \phi_n' \mid V \frac{Q}{(E_n' - \mathcal{H}_0)^2} \mu_{ex} \mid \phi_n > . \qquad \text{(A.2.20)}$$

$\delta\mu_{ex}$, $\delta\mu_{cm}$ and $\delta\mu_{cr}$ indicate the deviation from the single-particle values. The resultant deviation of the magnetic moment of the Schmidt value can be written in terms of the following equation using the effective operators:

$$\delta<\mu^\alpha>^i = < \{ \delta g_l^{\alpha i} \mathbf{l} + \delta g_s^{\alpha i} \mathbf{s} + \delta g_p^{\alpha i} [Y \times s] \} O^\alpha > ,$$

where $\alpha = 0, 1$; $\quad O^{(0)} = 1, O^{(1)} = \tau$; $\quad i = ex, cm, cr .$ $\qquad \text{(A.2.21)}$

Above, g_l, g_s and g_p are the orbital, spin and tensor g-factors. The features of this equation are that the tensor term has been introduced and all corrections in the g-factor are given as deviations from free-nucleon values.

These precise calculations were performed in doubly closed shells ±1 nucleon nuclei. The magnetic moment extracted from the above calculations are listed in Table 6.2 (TO83)(AR88). The Δ isobar effects and the cross term include the term "ex" in this table. Independent calculations by References (TO83) and (AR88) gave similar values. Although either the corrections from the exchange currents or second-order configuration-mixing are too large to explain the experimental value, it becomes closer in many cases by summing both effects.

The effective g-factors, which summed contributions from exchange currents, the configuration mixing and their cross term, are almost the same values for A = 15, 17, 39 and 41. These effective g-factors are almost the same as those deduced by a shell-model calculation in the sd-shell by Brown et al.. As already mentioned in the previous section, in the sd-shell Brown et al. performed calculations of the magnetic moments while considering first-order configuration-mixing. Instead of calculating the second-order effects, they also obtained effective g-factors by fitting the moment to the experimental values (BR83). This consistency suggests that effects beyond first-order configuration-mixing, i.e., exchange currents and the second-order configuration-mixing, are almost of the same magnitude in the same shell.

A.2.5 Relativistic and quark models

We were able to explain magnetic moments quantitatively by introducing exchange currents and second-order configuration-mixing. However, there are some dissatisfactions. One is that all of the calculations mentioned above are in the non-relativistic framework. Since we know that the nucleons inside a nucleus are moving with the Fermi momentum, we need a relativistic framework in order to treat their motion more precisely. The other is that the calculations mentioned above don't reflect the quark's degrees of freedom, of which nucleons consist. Thus, in the more sophisticated nuclear models, relativistic models and quark models have been investigated vigorously in recent years. However, they have not until now succeeded in reproducing the observed magnetic moments. In the following sections, such calculations and recent results are introduced.

(a) Relativistic models

The relativistic motion of the nuclei inside a nucleus can be described by the following Dirac equation,

$$[\,\alpha p + \beta M + V(r)\,]\,\Phi(r) = E\,\Phi(r)\,, \qquad \text{(A.2.22)}$$

where α and β are the Dirac matrix elements, M is the mass of the nucleon and V is the effective potential. Assuming an effective potential, the Dirac equation (A.2.22) can be solved to give the single-particle wave function (OH73) (NE89). The operator of the magnetic moments is given by

$$\mu = \gamma_0\, M\, r \times \alpha + \gamma_a\, \beta\, \sigma\,, \qquad \text{(A.2.23)}$$

where γ_0 and γ_a indicate the Dirac moment and the anomalous moment of the nucleon, respectively. From the wave function and the operator, we can obtain relativistic effects concerning the magnetic moments (OH73) (NE89).

It is also important to extend this method to a calculation of the configuration-mixing effect. Although there have been some attempts (NE89), consistent relativistic calculations in complete model-space have not yet been realized.

A relativistic σ-ω model became available recently (SE86), which can be used to well explain the features of nuclei, e.g., the binding energy. However, the magnetic moments calculated from the model are quite different from Schmidt values for doubly closed shell ±1 nucleon nuclei, since the effective nucleon mass inside a nucleus is about 0.56 of the free-nucleon mass (BO84). From the recent study, it was found that this model affects the spin-orbital currents (NI88), and induces magnetic currents (CH89); as a result, the new calculated values have become close to the Schmidt values.

Until now, almost all calculations have been for doubly closed shell ±1 nuclei, owing to the simple nuclear structure. Table A.2.1 shows results from recent calculations involving various relativistic models. The consistency between these calculated and experimental values is not very good. Especially, by comparing these calculations with the non-relativistic calculations (Table A.2.1), we find that the latter is still better for explaining the experimental values. We must therefore conclude that it is too early to take into account the corrections from relativistic models.

(b) Quark models

We now believe that the basic theory of the strong interaction is Quantum Chromo Dynamics (QCD), in which nucleons comprise quarks and glueons. We may explain the features of the nucleus better in the framework of QCD. However, until now, it has been impossible to apply QCD directly to studies of the nuclear structure and nucleon-nucleon interactions. The quark

Isoscalar moment ($\equiv \mu_{(p\text{-}odd)} + \mu_{(n\text{-}odd)}$)

A	Model	$\mu^{n.r.}{}_S$ (nm)	$\mu^{r.}{}_S$ (nm)	$\delta^{r.}{}_{c.m.}$ (nm)	$\delta^{n.r.}{}_{ex.}$ (nm)	μ_{Tot} (nm)	$\mu_{Exp.}$ (nm)	Δ (nm)	$\Delta/\mu^{n.r.}{}_S$ (%)
39	OH	+1.272	+1.235	—	—	+1.235	+1.414	-0.179	- 14.1
	NE		+1.948	+0.008	-0.001	+1.955		+0.541	+ 42.5
	CH		+1.206	—	—	+1.206		-0.208	- 16.4
41	OH	+3.880	+3.757	—	—	+3.757	+3.836	-0.079	- 2.0
	NE		+4.476	-0.042	-0.074	+4.360		+0.524	+ 13.5
	CH		+4.112	—	—	+4.112		+4.276	+ 7.1

Isovector moment ($\equiv \mu_{(p\text{-}odd)} - \mu_{(n\text{-}odd)}$)

A	Model	$\mu^{n.r.}{}_S$ (nm)	$\mu^{r.}{}_S$ (nm)	$\delta^{r.}{}_{c.m.}$ (nm)	$\delta^{n.r.}{}_{ex.}$ (nm)	μ_{Tot} (nm)	$\mu_{Exp.}$ (nm)	Δ (nm)	$\Delta/\mu^{n.r.}{}_S$ (%)
39	OH	-1.024	-1.079	—	—	-1.079	-0.624	-0.455	- 44.4
	NE		-0.434	+0.148	-0.664	-0.950		-0.326	- 31.8
	CH		-1.090	—	—	-1.090		-0.466	- 45.5
41	OH	+7.706	+7.569	—	—	+7.569	+7.026	+0.543	+ 7.0
	NE		+8.283	-1.032	+1.526	+8.777		+1.751	+ 22.7
	CH		+7.937	—	—	+7.937		+0.911	+ 11.8

$\delta \equiv \mu - \mu^{r.}{}_S$, $\Delta \equiv \mu_{Tot} - \mu_{Exp}$, $\mu_{Tot} = \mu^{r.}{}_S + \delta^{r.}{}_{c.m.} + \delta^{n.r.}{}_{ex.}$,

OH ; (OH74), NE ; (NE89), CH ; (CH89)

Table A.2.1 Magnetic moments predicted by the relativistic models. "r." and "n.r." mean the relativistic frame and the non-relativistic frame, respectively. "S", "c.m." and "ex." mean the Schmidt value, the configuration-mixing and the exchange currents, respectively.

models, which have features of QCD, have therefore been used in such studies. There are two major models of this kind: the bag model and the potential model. The main difference in these two models is the difference in the way to describe the confinement of quarks. In the bag model, confinement is described in terms of the bag surface, or by introducing another field. In the potential model, confinement is described by the interactions among quarks; a hadron can be described as a quark cluster in which quarks interact weakly with each other. These models are well reproduced by the observed features of a hadron. Beyond these successes, studies of nucleon-nucleon interactions using quark models have been vigorous; even calculations of the magnetic moments have been attempted.

The quark shell model (QSM) is based on the bag model, and starts from the picture that quarks moved independently in the big bag. By introducing a pairing interaction among quarks, it is assumed to act only between quark pairs having $J = T = 0$. The magnetic moment therefore results from only the contribution of one quark. In the doubly closed shell ±1 nucleon region (A = 15, 17, 39 and 41) calculations of magnetic moments in this model have been performed (AR87) (KA90). Even in the latest calculation results, which include the configuration mixing and Δ isobar effects, the deviation from the Schmidt values is too large.

The quark cluster model, another powerful method, is based on the potential model, and has the feature that many exchange processes occur among three quarks. That is, the quark cluster contributes to the magnetic moment as exchange currents, as is shown in the case of π mesons (Quark Exchange Currents ; QEC) (YA91). Using this model, calculations of the magnetic moments of A = 15, 17 and 39 were performed (YA91). From these

calculations, a significant contribution from the exchange current in the magnetic moment was found.

Since the application of quark models to the magnetic moments has just started recently, it is too early to present quantitative discussions. However, the search for the quark degree of freedom in magnetic moments is very interesting and promising.

A.2.6 Prediction values of the magnetic moment of ^{43}Ti

The general calculation methods for the magnetic moment are described in the former sections through the historical stream. In this section, the calculation values of the magnetic moment of ^{43}Ti are presented.

^{43}Ti is one of the $f_{7/2}$ mirror nuclei, and is close to the A=40 doubly closed shell. However, there are only a few predicted values available. One predicted value comes from Large-Scale Shell-model calculations; the other comes from the "odd nucleon model" by Buck et al..

(a) Large-Scale Shell-model calculations

By considering the first-order configuration-mixing described in Section A.2.3, calculations of the magnetic moment of ^{43}Ti were performed. In this section, a method developed by Ogawa et al. (HO87) is introduced as an example of this kind of calculation.

We consider ^{40}Ca as being a firm core, and consider the fp-shell as being a model space. The number of active nucleons is therefore three. However, the number of excited nucleons is limited to two, due to the limited calculation ability of a computer for numerical calculations, which is called the 2-jump model. The configuration to consider is therefore

$$(0f_{7/2})^3 + (0f_{7/2})^2 (1p_{3/2}, 0f_{5/2}, 1p_{1/2})^1 + (0f_{7/2})^1 (1p_{3/2}, 0f_{5/2}, 1p_{1/2})^2 . \qquad \text{(A.2.24)}$$

No effective interactions have been proved to exist in the fp-shell, unlike the case of the p- and sd-shells, due to the too large model space. We, therefore, just give the residual interaction through the procedure described in A.2.3-(i). We introduce the following residual interaction:

$$< f_r \mid V \mid f_r >_{TJ} = < f_r \mid V_{KB} \mid f_r >_{TJ} - 0.3(-)^T$$

$$< f_{7/2}^2 \mid V \mid f_{5/2}^2 >_{TJ} = 0.6 < f_{7/2}^2 \mid V_{KB} \mid f_{5/2}^2 >_{TJ}$$

$$f : 0f_{7/2},\ r = \{ 1p_{3/2}, 0f_{5/2}, 1p_{1/2} \}, \qquad \text{(A.2.25)}$$

where V_{KB} indicates the Kuo-Brown interaction (KU68). We used the single-particle energies shown in Table A.2.2, which are based on the ^{40}Ca excitation energies.

We solved Equation (A.2.11) using Equations (A.2.24) and (A.2.25) and obtain the wave function. At the same time, we obtained the wave function of ^{43}Sc, which is a mirror partner of ^{43}Ti, due to the charge symmetry of the nuclear potential. The magnetic moments of ^{43}Ti and ^{43}Sc can be obtained from the given wave function and the operator of Equation (A.2.13). If we omit the tensor term, the isoscalar and isovector moments are given by

$$\mu^{(0)} = [\, g_l^0 < \Sigma\, l_z > + g_s^0 < \Sigma\, s_z >] \,/\, 2$$

and

$$\mu^{(1)} = [\, g_l^1 < \Sigma\, \tau l_z > + g_s^1 < \Sigma\, \tau s_z >] \,/\, 2\,, \qquad \text{(A.2.26)}$$

where (0) and (1) mean the isoscalar and isovector moment, respectively, and $< \Sigma\, l_z >$, $< \Sigma\, s_z >$, $< \Sigma\, \tau l_z >$ and $< \Sigma\, \tau s_z >$ are the matrix elements. These matrix elements for the orbital angular momentum and intrinsic spin are shown in Table A.2.3 (OG89).

By substituting the g-factors of Equation (A.2.26) by free nucleon values,

	Single particle energy
$\varepsilon_p(0f_{7/2}) = \varepsilon_n(0f_{7/2})$	0.0 MeV
$\varepsilon_p(1p_{3/2}) = \varepsilon_n(1p_{3/2})$	2.200 MeV
$\varepsilon_p(0f_{5/2}) = \varepsilon_n(0f_{5/2})$	6.6620 MeV
$\varepsilon_p(1p_{1/2}) = \varepsilon_n(1p_{1/2})$	4.0240 MeV

Table A.2.2 Single particle energies in Ogawa's calculation.

Model	Single particle	1'st order c.m. [1)]
$<\sigma>$	+ 1.00	+ 1.0882
$<l>$	+ 3.00	+ 2.9557
$<\tau\sigma>$	- 1.00	- 0.8354
$<\tau l>$	- 3.00	- 1.4901

1) ; (OG89)

Table A.2.3 Theoretical matrix elements of the A = 43 mirror pair with the first order configuration mixing effect.

	μ of ^{43}Ti (nm)	Memo
Schmidt value	-1.913	free-nucleon g-factors
K. Ogawa et. al (OG89)	- 0.754	free-nucleon g-factors
S.M. Perez et. al (PE87)	- 0.784 (52)	
W. Richter et. al (RI91)	- 0.640	free-nucleon g-factors
	- 0.834	effective g-factors
the present study	(-) 0.85 (2)	

Table A.2.4 Comparison of the experimental magnetic moment of ^{43}Ti with theoretical predictions.

we obtained the magnetic moments of ^{43}Ti and ^{43}Sc to be -0.7544 μ_0 and +4.6674 μ_0 , respectively, as shown in Table A.2.4.

Recently, other calculations based on first-order configuration-mixing have been performed by Richter et al. (RI91). In this work, new two-body interactions were derived for nuclei in the lower part of the fp-shell by fitting semi-empirical potential forms and two-body matrix elements to 61 binding and excitation energy data in the mass range 41 to 49. The shell-model calculations assumed a ^{40}Ca core and that valence nucleons are distributed over the full fp-space. This is similar to the calculation performed for the sd-shell by Brown et al. (BR83), though the fitting range was limited. They also derived the effective g-factors in the fitting range by comparing their calculated results with the observations. The predicted values for the magnetic moments of ^{43}Ti and ^{43}Sc are -0.640 μ_0 and +4.547 $\mu_{0,,}$ respectively, with free-nucleon g-factors. If we adopt their effective g-factors, they are -0.834 μ_0 and +4.589 $\mu_{0,,}$ respectively, to find a better agreement with the experimental values. These predicted values are summarized in Table A.2.4.

(b) Semi-empirical "Odd-Nucleon Model"

Buck et al. paid attention to whether the number of nucleons in the mirror nuclei is odd or even, and made the new empirical model based on the magnetic moments (BU83).

They referred to the magnetic moments of odd-proton and odd-neutron nuclei in the mirror pair, as follows:

$$\mu_p = g_l^p L_o + g_s^p S_o + g_l^n L_e + g_s^n S_e$$

and

$$\mu_n = g_l^n L_o + g_s^n S_o + g_l^p L_e + g_s^p S_e , \qquad \text{(A.2.27)}$$

where o and e indicate the odd and even nucleon groups, respectively. In the single-particle model, the magnetic moments of the mirror nuclei are determined only from the contribution of the odd-nucleon group. Equations (A.2.27) thus change according to

$$\mu_p \sim g_l^p J + (g_s^p - g_l^p) S_o$$

and

$$\mu_n \sim g_l^n J + (g_s^n - g_l^n) S_o . \qquad \text{(A.2.28)}$$

The relationship between μ_p and μ_n can thus be written as

$$\mu_p \sim \alpha \mu_n + \beta J . \qquad \text{(A.2.29)}$$

Using the g-factors ($g = \mu / J$), it becomes

$$g_p \sim \alpha g_n + \beta . \qquad \text{(A.2.30)}$$

They found a strong correlation between the experimental g_p and g_n values, so that α and β can be universal constants. Their results showed that α = -1.145(12) and that β = +1.056(21). Using these values, they predicted unknown magnetic moments including that of ^{43}Ti. Their predicted value of the magnetic moment of ^{43}Ti is -0.784(52) μ_0 (PE87), as shown in Table A.2.4.

Appendix 3. Details of the calculation for the abrasion model

In order to calculate the production cross section and the excitation energy, the single-particle densities (ρ) shown in Equations (2.2) and (2.4) are necessary. As the single-particle densities we used the following Woods-Saxon type:

$$\rho(r) = \frac{\rho_0}{1 + \exp((r - R) / a)} . \qquad \text{(A.3.1)}$$

Here, a is the diffuseness parameter (a=0.60 fm in the calculation) and R and ρ_0 are parameters, which are given by solving

$$< r^2 > = \int_0^\infty r^2 \rho(r) 4 \pi r^2 dr$$

$$= \frac{3}{5} R_a^2 \qquad \text{(A.3.2.a)}$$

and

$$1 = \int_0^\infty \rho(r) 4 \pi r^2 dr , \qquad \text{(A.3.2.b)}$$

where $< r^2 >$ is the root mean square radius and R_a is the so-called nuclear radius ($R_a = 1.18 A^{1/3}$ fm, where A is the mass number).

The integration ranges in Equations (2.2) and (2.4) are set according to the following:

Overlap region	(x-axis direction)	(A.3.3.b)
0 --> R + 2.0 fm	(y-axis direction)	(A.3.3.c)
0 --> R + 2.0 fm	(z-axis direction) .	(A.3.3.a)

In the above, the overlap region is determined by the impact parameter (b).

We can thus integrate Equations (2.2) and (2.4) for the finite impact parameter, and thus obtain the production cross-sections (abrasion cross-

sections) and the excitation energy of the fragments, such as those given in Table 5.3.

Appendix 4. Details of the calculation for the polarization

In this section, the calculation of the polarization in the case of l=2 (1d-state) is shown in detail.

The wave function of the 1d-shell can be obtained from the harmonic-oscillator potential,

$$V(r) = - V_0 + \frac{1}{2} m \omega^2 r^2 . \qquad \text{(A.4.1)}$$

Using this potential, the Shrödinger equation is given by

$$\left[- \frac{\hbar}{2m} \nabla^2 - V_0 + \frac{1}{2} m \omega^2 r^2 \right] \Phi = E \Phi . \qquad \text{(A.4.2)}$$

In polar coordinates, we can solve the equation and obtain the 1d state wave function as follows:

$$\Phi_{+2} = \sqrt{\frac{1}{8}}\, \pi^{-1/4} b^{-3/2} \left(\frac{r}{b} \right)^2 \exp\left(- \frac{r^2}{2 b^2} \right) \sin^2\theta \exp(2 i \phi) , \quad \text{(A.4.3.a)}$$

$$\Phi_{+1} = - \sqrt{\frac{1}{2}}\, \pi^{-1/4} b^{-3/2} \left(\frac{r}{b} \right)^2 \exp\left(- \frac{r^2}{2 b^2} \right) \sin\theta \cos\theta \exp(i \phi) , \quad \text{(A.4.3.b)}$$

$$\Phi_{0} = \sqrt{\frac{1}{12}}\, \pi^{-1/4} b^{-3/2} \left(\frac{r}{b} \right)^2 \exp\left(- \frac{r^2}{2 b^2} \right) (\cos^2\theta - 1) , \quad \text{(A.4.3.c)}$$

$$\Phi_{-1} = \sqrt{\frac{1}{2}}\, \pi^{-1/4} b^{-3/2} \left(\frac{r}{b} \right)^2 \exp\left(- \frac{r^2}{2 b^2} \right) \sin\theta \cos\theta \exp(- i \phi) , \quad \text{(A.4.3.d)}$$

and

$$\Phi_{-2} = \sqrt{\frac{1}{8}}\, \pi^{-1/4} b^{-3/2} \left(\frac{r}{b} \right)^2 \exp\left(- \frac{r^2}{2 b^2} \right) \sin^2\theta \exp(- 2 i \phi) . \quad \text{(A.4.3.e)}$$

Here, normalization is included and b is the oscillator parameter.

By putting Equations (A.4.3) into Equation (2.17), we obtain the following equations:

$$\frac{d\sigma_2}{dk} = \frac{1}{8\sqrt{\pi}} b^{-3} \int dz$$

$$\int \frac{d x}{2\pi} \exp(- i k x) \left(\frac{r_1}{b} \right)^2 \left(\frac{r_2}{b} \right)^2 \exp\left(- \frac{1}{2 b^2} (r_1^2 + r_2^2) \right) \exp(2 i (\phi_1 - \phi_2)) ,$$

(A.4.4.a)

$$\frac{d\sigma_1}{dk} = 0 , \qquad \text{(A.4.4.b)}$$

$$\frac{d\sigma_0}{dk} = \frac{1}{12\sqrt{\pi}} b^{-3} \int dz$$

$$\int \frac{dx}{2\pi} \exp(-ikx) \left(\frac{r_1}{b}\right)^2 \left(\frac{r_2}{b}\right)^2 \exp\left(-\frac{1}{2b^2}(r_1^2 + r_2^2)\right) , \qquad \text{(A.4.4.c)}$$

$$\frac{d\sigma_{-1}}{dk} = 0 , \qquad \text{(A.4.4.d)}$$

and

$$\frac{d\sigma_{-2}}{dk} = \frac{1}{8\sqrt{\pi}} b^{-3} \int dz$$

$$\int \frac{dx}{2\pi} \exp(-ikx) \left(\frac{r_1}{b}\right)^2 \left(\frac{r_2}{b}\right)^2 \exp\left(-\frac{1}{2b^2}(r_1^2 + r_2^2)\right) \exp(-2i(\phi_1 - \phi_2)) .$$

(A.4.4.e)

By using

$$(r_1 r_2)^2 \exp(2i(\phi_1 - \phi_2)) = \left[z^2 - \frac{x^2}{4} + s_0^2 - s_0 x i \right]^2 , \qquad \text{(A.4.5)}$$

Equation (A.4.4.a) changes to

$$\frac{d\sigma_2}{dk} = \frac{1}{8\sqrt{\pi}} b^{-3} \int dz$$

$$\int \frac{dx}{2\pi} \exp(-ikx) \left[\left(\frac{s_0}{b}\right)^2 + \left(\frac{z}{b}\right)^2 - \frac{x^2}{4b^2} - \frac{s_0 x}{b^2} i \right] \exp\left(-\frac{z^2}{b^2}\right) \exp\left(-\frac{x^2}{4b^2}\right)$$

$$= C_2 \int \frac{dx}{2\pi} \exp(-ikx) [3 + 2(a - xi)^2 + (a - xi)^4] \exp\left(-\frac{x^2}{2}\right) . \qquad \text{(A.4.6)}$$

Here,

$$a = \frac{\sqrt{2}\, s_0}{b} \quad \text{and} \qquad C_2 = \frac{1}{32\sqrt{\pi}} b^{-1} \exp\left(-\frac{s_0^2}{b^2}\right).$$

Furthermore, by Fourier transforming Equation (A.4.6) we obtain

$$\frac{d\sigma_2}{dk} = C_2 \exp\left(-\frac{k^2}{2}\right) \left[3 + 2\left(a + \frac{d}{dk} - k\right)^2 + \left(a + \frac{d}{dk} - k\right)^4 \right]. \qquad \text{(A.4.7)}$$

Using

$$\left(a + \frac{d}{dk} - k\right)^2 = (a - k)^2 - 1$$

and

$$\left(a + \frac{d}{dk} - k\right)^4 = (a - k)^4 - 6(a - k)^2 + 3 ,$$

Equation (A.4.7) changes to

$$\frac{d\sigma_2}{dk} = C_2 \exp\left(-\frac{k^2}{2}\right) [(k - a)^2 - 2]^2 . \qquad \text{(A.4.8)}$$

By using similar procedures for Equations (A.4.4.c) and (A.4.4.e), we obtain

$$\frac{d\sigma_{-2}}{dk} = C_2 \exp\left(-\frac{k^2}{2}\right) [(k + a)^2 - 2]^2 \qquad \text{(A.4.9)}$$

and

$$\frac{d\sigma_0}{dk} = \frac{2}{3} C_2 \exp\left(-\frac{k^2}{2}\right) [k^2 - a^2 - 2]^2 . \qquad \text{(A.4.10)}$$

Thus, the production cross sections are summarized as follows:

$$\frac{d\sigma_2}{dk} = \frac{3}{8} N \exp(-b^2 k^2) \left[\left(\frac{k}{\Gamma} - 1\right)^2 - \left(\frac{b}{s_0}\right)^2 \right]^2 , \qquad \text{(A.4.11.a)}$$

$$\frac{d\sigma_{-2}}{dk} = \frac{3}{8} N \exp(-b^2 k^2) \left[\left(\frac{k}{\Gamma} + 1\right)^2 - \left(\frac{b}{s_0}\right)^2 \right]^2 , \qquad \text{(A.4.11.b)}$$

$$\frac{d\sigma_0}{dk} = \frac{1}{4} N \exp(-b^2 k^2) \left[\left(\frac{k}{\Gamma}\right)^2 - 1 - \left(\frac{b}{s_0}\right)^2 \right]^2 , \qquad \text{(A.4.11.c)}$$

and

$$\frac{d\sigma_0}{dk} = \frac{d\sigma_0}{dk} = 0 , \qquad \text{(A.4.11.d)}$$

where

$$N = \frac{32}{3} C_2 \frac{s_0^4}{b^4} \quad \text{and} \qquad \Gamma = \frac{s_0}{b^2} .$$

Summing these cross-sections, we obtain Equation (2.18). Further, by using Equations (A.4.11) and (2.18) we obtain the polarization of the 1d-state as shown in Equation (2.19).

Appendix 5 Flow chart of the program used in particle identification.

A (a) foreground / (b) background program flow of the KODAQ system is shown (OM91).

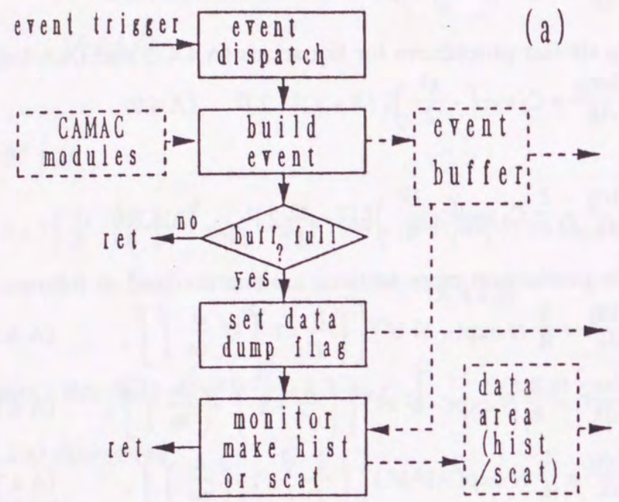

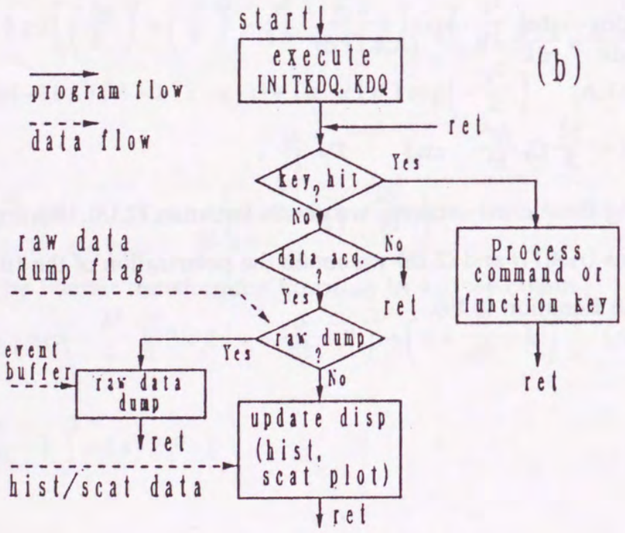

Appendix 6 Flow chart of the program used in β-NMR

Flow chart of the main program to control NMR

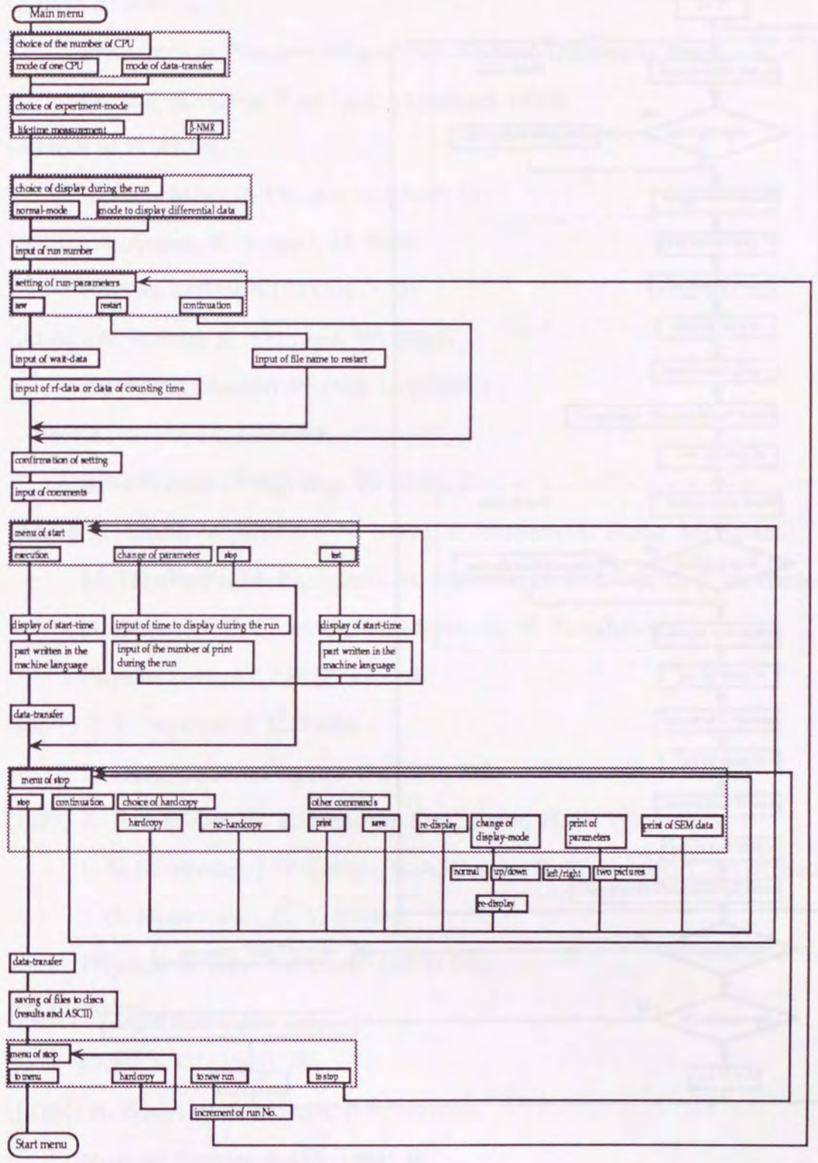

Flow chart of the part written in the machine language.

(Loop-number for temporary saving is M in the program.)

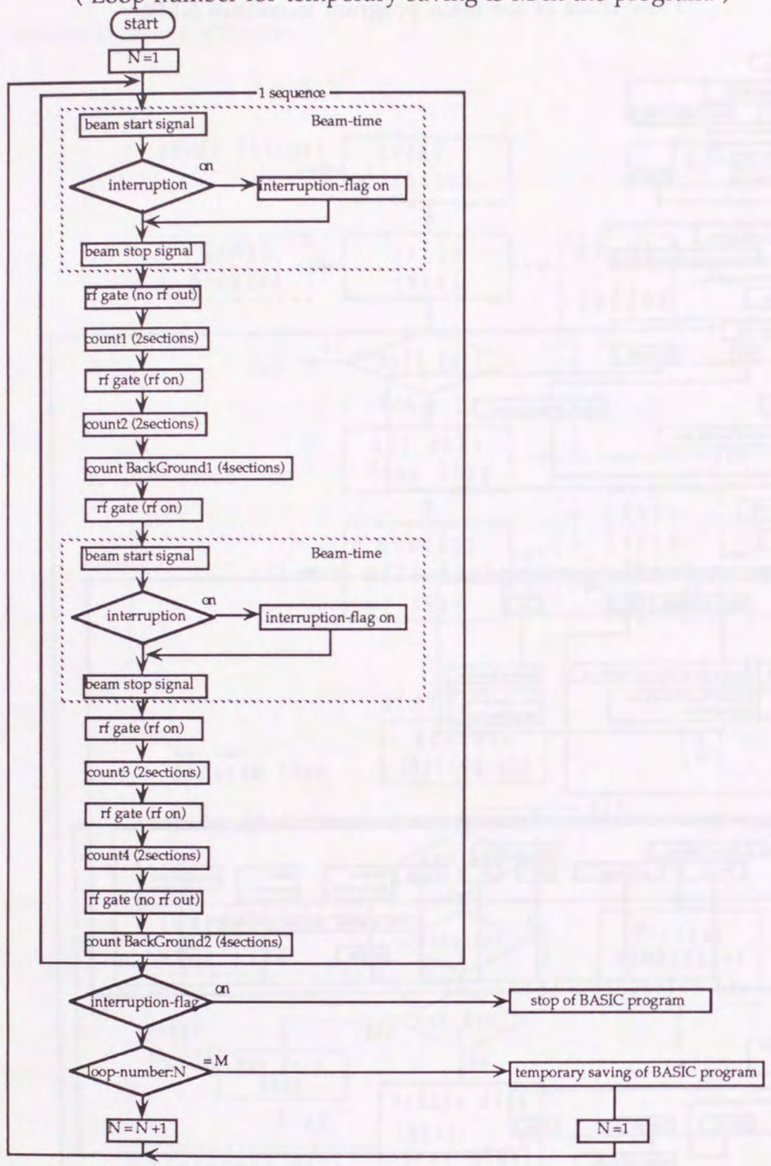

References

(AB61) A. Abragam,
Principles of Nuclear Magnetism, Oxford University Press,
Oxford, (Original Text 1961, paperback 1983)

(AH80) S. P. Ahlen,
Review Modern Physics 52 (1980) 121

(AR87) A. Arima, K. Yazaki, H. Bohr,
Physics Letters B 183 (1987) 131

(AR88) A. Arima, K. Shimizu, W. Bentz,
Advances Nuclear Physics 18 (1988) 1

(AS86) K. Asahi, M. Ishihara,
RIKEN Accel. Prog. Rep. 20 (1986) 21

(AS90) K. Asahi, M. Ishihara, N. Inabe, T. Ichihara, T. Kubo, M. Adachi,
H. Takahashi, M. Kouguchi, M. Fukuda, D. Mikolas, D. J. Morrissey,
D. Beaumel, T. Shimoda, H. Miyatake, N. Takahashi,
Physics Letters B 251 (1990) 488

(BE75) B. L. Berman, S. C. Fultz,
Review Modern Physics 47 (1975) 713

(BI79) K. Van Bibber, D. L. Hendrie, D. K. Scott, H. H. Weiman,
L. S. Schroeder, J. V. Geaga, S. A. Cessin, R. Treauhaft, Y. J. Grossiord,
J. O. Rasmussen, C. Y. Womg,
Physical Review Letters 43 (1979) 840

(BL49) N. Bloembergen,
Physica XV (1949) 386

(BO84) A. Bouyssy, S. Marcos, J. F. Mathiot,
Nuclear Physics A 415 (1984) 497

(BR83) B. A. Brown, B. H. Wildenthal,
Physical Review C 28 (1983) 2397

(BR85) B. A. Brown, B. H. Wildenthal,
Atomic Data and Nuclear Data Tables 33 (1985) 347

(BU83) B. Buck, S. M. Perez,
Physical Review Letters 50 (1983) 1975

(CH89) P. Christillin, G. Do Dang,
Physics Letters B 226 (1989) 22

(CO65) S. Cohen, D. Kurath,
Nuclear Physics 73 (1965) 1

(DU86) J. P. Dufour, R. Del Moral, H. Emmermann, F. Hubert, D. Jean,
C. Poinot, M. S. Pravikoff, A. Fleury, H. Delagrange, K. -H. Schmidt,
Nuclear Instruments and Methods in Physics Research A 248 (1986) 267

(EN90) P. M. Endt,
Nuclear Physics A 521 (1990) 1

(FE68) F. D. Feiock, W. R. Johnson,
Physical Review Letters 21 (1968) 785

(GL59) R. J. Glauber,
Lectures in Theoretical Physics Vol. 1.,
Interscience, New York, (1959)

(GO74) A. S. Goldhaber,
Physics Letters 53B (1974) 306

(GR75) D. E. Greiner, P. J. Lindstrom, H. H. Heckman, B. Cork, F. S. Bieser,
Physical Review Letters 35 (1975) 152

(GU83) C. Guet,
Nuclear Physics A 400 (1983) 191c

(GU85) D. Guerreau,

Nuclear Physics A 447 (1985) 37c

(HO76) B. R. Holstein,
Review of Modern Physics 48 (1976) 673

(HO87) J. Honkanen, V. Koponen, H. Hyvonen, P. Taskinen, J. Aysto,
K. Ogawa,
Nuclear Physics A 471 (1987) 489

(HÜ75) J. Hüfner, K. Schafer, B. Schurmann,
Physical Review C 12 (1975) 1888

(HÜ81) J. Hüfner, M. C. Nemes,
Physical Review C 23 (1981) 2538

(IN80) N. Inoue, K. Kumagai, T. Sugawara
Journal of the Physical Society of Japan 48 (1980) 1123

(JO83) W. R. Johnson, D. Kolb, K. -N. Huang,
Atomic Data and Nuclear Data Tables 28 (1983) 333

(KA90) M. Kato, W. Bentz, K. Shimizu, A. Arima,
Physical Review C 42 (1990) 2672

(KU68) T. T. S. Kuo, G. E. Brown,
Nuclear Physics A 114 (1968) 241

(MA89) K. Matsuta, J. R. Alonso, G. F. Krebs, T. J. M. Symons, M. Izumi,
Y. Nojiri, T. Minamisono, A. Kitagawa, A. Ozawa, S. Momota,
Y. Matsuo, T. Ohtsubo, K. Sugimoto, I. Tanihata, K. Omata, Y. Shida,
S. Shimoura, T. Kobayashi,
First International Conference of Radioactive Nuclear Beams,
World Scientific, (1989) 575
K. Matsuta, M. Izumi, Y. Nojiri, T. Minamisono, A. Kitagawa,
A. Ozawa, S. Momota, Y. Matsuo, T. Ohtsubo, K. Sugimoto, I. Tanihata,
K. Omata, Y. Shida, S. Shimoura, T. Kobayashi, J. R. Alonso,

G. F. Krebs, T. J. M. Symons,
First International Conference of Radioactive Nuclear Beams,
World Scientific, (1989) 457 ;

(MI73) T. Minamisono,
Journal of the Physical Society of Japan 34 Supplement (1973) 324

(MI76) T. Minamisono, J. W. Hugg, D. G. Mavis, T. K. Saylor, H. F. Glavish,
S. S. Hanna,
Physics Letters 61B (1976) 155

(MI87) T. Minamisono,
Hyperfine interactions 35 (1987) 979

(MI90) T. Minamisono, Y. Nojiri, K. Matsuta, K. Takeyama, A. Kitagawa,
T. Ohtsubo, A. Ozawa, M. Izumi,
Nuclear Physics A 516 (1990) 365

(MO73) M. Morita,
Beta Decay and Muon Capture,
W. A. Benjamin Inc., Reading, Massachusetts (1973)

(MU83) M. J. Murphy, R. G. Stokstad,
Physical Review C 28 (1983) 428

(NA67) A. Narath,
Physical Review 162 (1967) 320

(NE89) Y. Nedjadi, J. R. Rook,
J. Phys. G; Nucl. Part. Phys. 15 (1989) 589

(NI88) S. Nishizaki, H. Kurosawa, T. Suzuki,
Physics Letters B 209 (1988) 6

(OG89) K. Ogawa,
Private communications

(OH73) H. Ohtsubo, M. Sano, M. Morita,

Journal of the Physical Society of Japan 34 Supplement (1973) 509
H. Ohtsubo, M. Sano, M. Morita,
Progress of Theoretical Physics, 49 (1973) 877

(OH88) T. Ohtsubo, Y. Yasui, S. Fukuda, A. Kitagawa, Y. Nojiri,
T. Minamisono,
Osaka University Laboratory of Nuclear Studies Annual Report
(1988) 56

(OH92) A. Ohnishi, T. Maruyama, H. Horiguchi,
Progress of Theoretical Physics 87 (1992) 417

(OM91) K. Omata, Y. Fujita, N. Yoshikawa, M. Sekiguchi, Y. Shida
INS Report 884 (1991)

(PA84) Particle Data Group,
Review Modern Physics 56 (1984)

(PE87) S. M. Perez,
Physical Review C 36 (1987) 1202

(PE89) G. Peilert, H. Stocker, W. Greiner, A. Rosenhauer, A. Bohnet,
J. Aichelin,
Physical Review C 39 (1989) 1402

(PU46) E. M. Purcell, H. C. Torrey, R. V. Pound,
Physical Review 69 (1946) 37

(RA89) P. Raghavan,
Atomic Data and Nuclear Data Tables 42 (1989) 189

(RI91) W. A. Richter, V. D. Merwe, R. E. Julies, B. A. Brown,
Nuclear Physics A 523 (1991) 325

(RO86) W. F. Rogers, D. L. Clark, S. B. Dutta, A. G. Martin,
Physics Letters B 77 (1986) 293
W. F. Rogers,

Doctor thesis, The University of Rochester, (1986)

(SE86) B. Serot, J. D. Walecka,
Advances in Nuclear Physics 16 (1986) 1

(SH86) K. Shima, T. Mikumo, H. Tawara,
Atomic Data and Nuclear Data Tables Vol. 34 (1986) 382

(SI73) R. Silberberg, C. H. Tsao,
The Astrophysical Journal Supplement 25 (1973) 315

(SI88) J. D. Silk, H. D. Holmgren, D. L. Hendrie, T. J. M. Symons, G. D. westfall,
P. H. Stetson, S. Raman, R. L. Auble, J. R. Wu, K. Van Bibber,
Physical Review C 37 (1988) 158

(SP81) K. H. Speidel, P. N. Tandon, V. Mertens,
Zeitschrift fur Physik A - Atoms and Nuclei 302 (1981) 107

(SU65) K. Sugimoto, A. Mizobuchi, K. Nakai, K. Matuda,
Physical Letters 18 (1965) 38

(SU73) K. Sugimoto, A. Mizobuchi, T. Minamisono, Y. Nojiri,
Journal of the Physical Society of Japan 34 Supplement (1973) 158

(SU77) K. Sugimoto, N. Takahashi, A. Mizobuchi, Y. Nojiri, T. Minamisono,
M. Ishihara, K. Tanaka, H. Kamitsubo,
Physical Review Letters 39 (1977) 323

(TA89) I. Tanihata,
Treatise on Heavy-Ion Science Vol.8 (1989) 443

(TE74) K. Terakura, N. Yokoyama, S. Kohzuki,
Journal of the Physical Society of Japan 36 (1974) 130

(TO83) I. S. Towner, F. C. Khanna,
Nuclear Physics A 399 (1983) 334

(TO86) I. S. Towner,
Comments Nucl. Part. Phys. 15 (1986) 145

(VA48) J.H. Van Vleck,
Physical Review 74 (1948) 1168

(VE74) A. Veyssière, H. Beil, R. Bergère, P. Carlos, A. Leprêtre, A. De Miniac,
Nuclear Physics A 227 (1974) 513

(VI79) Y. P. Viyogi, T. J. M. Symons, P. Doll, D. E. Greiner, H. H. Heckman,
D. L. Hendrie, P. J. Lindstorm, J. Mahoney, D. K. Scott, K. Van Bibber,
G. D. Westfall, H. Wieman,
Physical Review Letters 42 (1979) 33

(WE76) G. D. Westfall, J. Gosset, P. J. Johansen, A. M. Poskanzer, W. G. Meyer,
H. H. Gutbrod, A. Sandoval, R. Stock,
Physical Review Letters 37 (1976) 1202

(WE79) G. D. Westfall, T. J. M. Symons, D. E. Greiner, H. H. Heckman,
P. J. Lindstrom, J. Mahoney, A. C. Shotter, D. K. Scott, H. J. Crowford,
C. McParland, T. C. Awes, C. K. Gelbke, J. M. Kidd,
Physical Review Letters 43 (1979) 1859

(WI82) D. H. Wilkinson,
Nuclear Physics A 377 (1982) 474

(WO82) C. Y. Wong, K. Van Bibber
Physical Review C 25 (1982) 2990

(YA85) T. Yamazaki,
Physics Letters B 160 (1985) 227

(YA91) Y. Yamauchi, A. Buchmann, A. Faessler,
Nuclear Physics A 526 (1991) 495